CHAPTER 88

Dislocation–Obstacle Interactions at the Atomic Level

D.J. BACON

Department of Engineering, The University of Liverpool, Brownlow Hill, Liverpool L69 3GH, UK

Y.N. OSETSKY

Materials Sciences and Technology, ORNL, Oak Ridge, TN 37831, USA

and

D. RODNEY

Science et Ingénierie des Matériaux et Procédés, INP Grenoble, CNRS/UJF, Domaine Universitaire, Boîte Postale 46, 38402 Saint Martin d'Hères, France

1572-4859, DOI: 10.1016/S1572-4859(09)01501-0

Dislocations in Solids
Edited by J. P. Hirth and L. Kubin

Contents

1. Introduction

The techniques of atomic-scale simulation by computer offer ways of investigating properties of crystal defects that are not usually open to direct study by experiment. Some have been in use for over 40 years and have provided important information on the atomic structure and energy of crystalline defects. This chapter is concerned with dislocation–obstacle interactions that resist the glide of dislocations in metals and hence increase the applied stress necessary to cause plastic deformation. Computer simulation of the atomic mechanisms involved in this area of materials science is fairly recent and the aim of this chapter is to highlight the understanding that has been achieved over the past decade. A recent handbook [1] provides a comprehensive introduction to many aspects of modelling at both the atomic and continuum scales. It includes descriptions of methods and examples of codes for a variety of techniques. We have tried to avoid unnecessary overlap except inasmuch that a clear description of the methods that have led to the results we present is required in order that their strength and weakness can be appreciated.

We assume a prior knowledge of basic properties of dislocations, such as the Burgers vector, $\boldsymbol{b}$; their edge, screw or mixed character; their glide (or slip) plane; the process of cross-slip; consequences of dissociation into partials; and the form of $\boldsymbol{b}$ of perfect dislocations in body-centred cubic (BCC) and face-centred cubic (FCC) metals, i.e. $\frac{1}{2}\langle 1\,1\,1\rangle$ and $\frac{1}{2}\langle 1\,1\,0\rangle$, respectively. (See Ref. [2] for an introduction and Refs [3,4] for more advanced and detailed presentations.) We do not go into detail about the atomic structure of dislocation cores: recent reviews of progress in modelling core structure in different metals and the influence of core structure on dislocation motion are to be found in Refs [5,6]. Nor do we study effects of grain or interphase boundaries on dislocation properties and behaviour, for the materials considered here are single crystals: simulation of boundary effects in nanocrystals and other materials are discussed in Ref. [7].

In the multiscale framework for simulating the properties of dislocations in metals, there are three distinct spatial scales, each involving distinct methods. The finest scale uses *ab initio* (first principles) calculations in which Schrödinger's equation for interacting electrons is used to compute the position of atoms [8]. It is restricted to a few hundred atoms at most and is therefore limited to the core region around a dislocation. The coarsest scale is the continuum, in which dislocations are treated as though in an elastic, rather than atomic, medium. The distortion field produced by a long dislocation varies inversely with distance and is thus long-ranged, and many of the important properties arising from this, such as stress, strain and strain energy, can be modelled using linear elasticity. Indeed, most of the applications of dislocation theory over the past 70 years have been based on this [2–4].

Modern approaches to continuum-scale computer simulation of dislocations are not dealt with here. (For a broad introduction see Ref. [1].)

Atomic-scale simulation treated in this chapter sits between the *ab initio* and continuum scales. It uses model sizes that are large enough to allow for the main effects of the distortion field, but also provides full resolution of the atomic structure of the dislocation core and the obstacles a dislocation may encounter as it moves under external loading. Although the strain energy of a dislocation is affected by the finite size of the atomic model, its core properties (structure, energy), and therefore its short-range interactions with other defects, are less sensitive and can be described with acceptable accuracy. This can be tested by simulating systems of increasing size in order to reach convergence of results with the desired accuracy. The size is usually limited for the practical reason that the computing (CPU) time required is proportional to the number of atoms.

The need to achieve results in reasonable time limits atomic-scale modelling in two other ways. First, the CPU time per atom is determined by the time needed to compute the forces between, and energy of, atoms using an interatomic potential. Thus, to minimise the CPU time, the potential should have a range as short as possible. The potentials currently used in the field are empirical potentials obtained by different realisations of the Embedded Atom Model (EAM) [9]. Their empirical parameters are based typically on fits to properties of the metal such as elastic constants, phonon spectra, cohesive energy, stacking fault energy, and surface and point defect energies, and, increasingly frequently, to *ab initio* data. For reviews see Ref. [8].[1]

Second, the total CPU time is proportional to the number of 'iterations' required to complete the simulation. 'Iterations' here has one of two meanings, depending on the simulation method. In molecular statics (MS), a crystal at temperature $T = 0\,\mathrm{K}$ is modelled, i.e. the kinetic energy of the atoms is maintained equal to zero, and the system achieves equilibrium when the potential energy, computed by summing the interatomic potential energy of the atoms minus the work of forces applied to the system, is minimised. This state is found from a trial starting configuration by a series of iterations in which the atoms are moved repeatedly. (See Ref. [1] for examples.) In molecular dynamics (MD), kinetic energy is not zero and at equilibrium the average kinetic energy per atom equals $3k_{\mathrm{B}}T/2$, where k_{B} is the Boltzmann constant. At a given time t, the acceleration of every atom is calculated from the force on it due to its neighbours using Newton's second law (force = mass × acceleration). This equation of motion is solved numerically for all atoms to predict their position at time $(t + \Delta t)$, where Δt is the MD time-step, e.g. Refs [1,10]. This procedure is repeated to enable the trajectory of atoms to be followed for as long as is necessary to complete the process under investigation, the number of iterations in this case being the number of time-steps. To maintain accuracy, Δt is typically of the order of one to a few femtoseconds ($1\,\mathrm{fs} = 10^{-15}\,\mathrm{s}$).

[1] For the references to the potentials used for the results presented in this chapter, the reader is referred to the original papers we cite.

We give a few examples of model size and computing resource required in Section 2. For the moment, it is sufficient to bear in mind that the models of interest here contain typically from a few hundred thousand to a few million atoms. Size in this range is usually sufficient for treatment of the elastic field of one dislocation and for it to move and interact with other defects without severe restriction by the model boundary conditions. In simulation of atomic dynamics by MD, the number of time-steps that can be accomplished within a reasonable CPU time is typically in the range 10^5–10^7, so that the total simulated time is of the order of nanoseconds ($1\,\mathrm{ns} = 10^{-9}\,\mathrm{s}$). Thus, the spatial and time scales of the work reviewed here are nanoscale.

A model for simulating dislocation–obstacle interactions on these scales should satisfy the following criteria.

(a) It should not artificially constrain the dislocation core structure and it should ensure that the displacement, $\boldsymbol{u}$, of the atoms from their perfect crystal sites exhibits the discontinuity that defines the dislocation with Burgers vector $\boldsymbol{b}$, i.e.

$$\boldsymbol{b} = \oint \mathrm{d}\boldsymbol{u}, \tag{1}$$

where the integral encircles the dislocation line.

(b) It should be large enough to permit accurate simulation of the effects of the elastic distortion field of the dislocation.

(c) It should allow for dislocation motion to occur as a result of application of external action in the form of stress or strain: this motion should not be restricted by the model boundaries.

(d) It should permit simulation of either static ($T = 0\,\mathrm{K}$) or dynamic ($T > 0\,\mathrm{K}$) conditions.

(e) Methods should be incorporated for visualising the atoms in the vicinity of the dislocation core and obstacle during the process under investigation.

Computer models that satisfy these criteria are described in the Section 2, with emphasis on a method that allows the construction of an infinite, periodic glide plane for the mobile dislocation. This model is applied in the following sections for simulation of the interaction of dislocations with crystalline defects. Practical limits on model size restrict the size of these defects to a few nanometres.

Much of the research presented here has been driven by the need to investigate the effect of radiation on the mechanical behaviour of metals in current and future nuclear power systems, for the defects of concern are of the order of a nanometre in size and their interactions with dislocations cannot be observed directly by experiment. The core components of reactors are subjected to irradiation by a flux of fast neutrons produced by the nuclear reaction (e.g. Ref. [11]). The neutrons induce damage in metals that can change their mechanical properties. Indeed, fast neutrons (as well as ions) produce localised regions of defects by the displacement-cascade process, in which an atom is given sufficient energy by an irradiating particle that it can displace many of its neighbours in an avalanche of collisions.

Displaced atoms that do not return to their lattice sites become self-interstitial atoms (SIAs), mainly at the periphery of a cascade, and a corresponding number of sites are left vacant in the central region (see Ref. [12] and references cited therein). A substantial fraction of these defects form clusters with their own kind, either during the cascade process itself, which has a lifetime $\sim 10\,\mathrm{ps}$, or after diffusion in the material. SIAs usually cluster as tightly packed planar arrays of crowdions that are nascent dislocation loops with perfect Burgers vector parallel to the crowdion axis, i.e. $\boldsymbol{b} = \frac{1}{2}\langle 1\,1\,0\rangle$ in FCC, $\frac{1}{2}\langle 1\,1\,1\rangle$ or $\langle 1\,0\,0\rangle$ in BCC and $1/3\langle 1\,1\,\bar{2}\,0\rangle$ in HCP (e.g. Refs [13–15]). Faulted loops with $\boldsymbol{b} = 1/3\langle 1\,1\,1\rangle$ also form in FCC metals. Vacancies cluster in the form of loops or, in FCC metals, in a specific dissociated structure called a stacking fault tetrahedron (SFT). Depending on the metal and irradiation conditions, they can also agglomerate to form voids and when He is present, as a result of either transmutation or direct injection, He-filled bubbles can arise. Plasticity is strongly affected by such clustered defects. The yield stress is usually increased, the work-hardening rate and ductility reduced and flow localisation by dislocation channelling can occur at high levels of cluster density (e.g. Refs [16–18]). In the latter case, deformation is inhomogeneous and localised in bands of intense plastic shear that appear to be clear of irradiation defects when observed in a transmission electron microscope (TEM) after the deformation, e.g. Ref. [16].

Linear elasticity theory can provide a description of dislocation interaction with obstacles. However, approximations have to be made for processes that are controlled by atomic mechanisms, in particular when the interaction involves direct contact between the dislocation and obstacle, for the core of the dislocation is involved in the interaction process. On the other hand, the defects produced under irradiation have sizes in the nanometre range and since their density is high, $\sim 10^{23}\,\mathrm{m}^{-3}$ (e.g. Refs [19–21]), their average separation is on the order of a few tens of nanometres. They are amenable to atomic-scale simulations. The aim of the research presented below has been to study both the elementary mechanisms of interaction between one dislocation of definite character (edge or screw) with one particular defect and measure directly from the simulation the pinning effect due to the defect on the dislocation. In a multiscale approach, such information can be then used in dislocation dynamics (DD) simulations to simulate the more statistical problem of the glide of dislocations in populations of defects [22].

After a description of the methods in Section 2, we consider in Section 3 the interaction of dislocations with the crystal itself (exemplified by the Peierls stress and DD) and solute atoms (interaction that controls solid solution hardening (SSH)). We then review interaction with voids and precipitates in Section 4. Obstacles with dislocation character are considered in Section 5, i.e. dislocation loops and SFTs. Because of the possibility of dislocation reactions, more complex and varied reactions are observed with this category of obstacle. The cases that have been studied extensively are those for FCC and BCC metals: HCP metals have received far less attention, mainly because of the absence of reliable interatomic potentials suited for the study of dislocations.

2. Structure of models used to simulate dislocations at the atomic level

2.1. Rigid boundary model

The simplest approach, which was used in early atomic-level modelling of dislocations [23–29], is to generate the atom coordinates of a perfect crystal of the required structure, orientation and size and impose on them the dislocation displacement field given by linear elasticity theory. In order to prevent a return to the perfect crystal state when relaxation occurs, boundary conditions have to be applied to the model. This is achieved by creating a layer of atoms (FR) fixed in their unrelaxed position around the outside of the inner region of mobile atoms (MR), i.e. rigid boundary conditions (RBCs) are used. This arrangement is shown schematically in Fig. 1(a) as a cross-section of a cylinder containing an edge dislocation. Invariance of the dislocation field along its line allows periodicity along the y-axis and this is readily achieved by adding the translation $\pm L_y$, i.e. the length of the model in the y direction, to the y coordinate of atoms in region MR. The thickness of the rigid and periodic layers has to be larger than the range of the interatomic potential in order that atoms in the inner region have a full set of neighbours.

The RBC method with this configuration has been used to study dislocation properties such as core structure and energy, and led to valuable insights in early work on the core properties of screw dislocations in BCC metals [29,30]. However, region MR must be sufficiently large for relaxation of the atoms in the vicinity of the dislocation core to be unrestricted by the rigid boundaries. This condition is particularly important when the dislocation can dissociate, i.e. the core is wide. For instance, the dissociation width of a screw dislocation in a model of Ni saturates

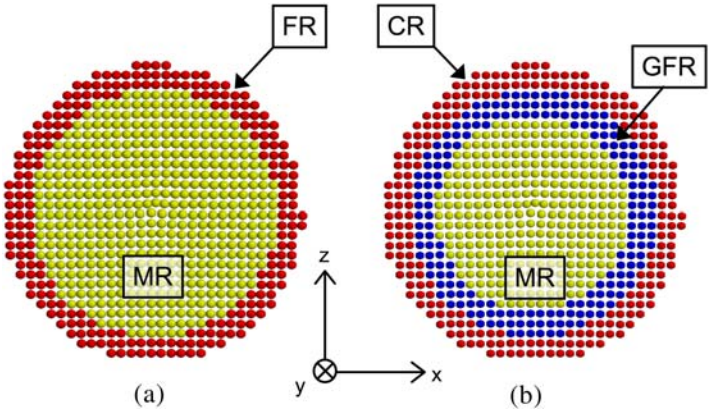

Fig. 1. (a) Representation of rigid boundary model showing regions of fixed (FR) and mobile (MR) atoms. (b) Representation of flexible boundary model showing the continuum (CR), Green's function (GFR) and mobile (MR) atom regions.

to the true value (~ 2 nm) only when the distance from the centre of the dislocation core to the fixed boundary is > 6.3 nm ($\sim 25b$) [31].

The initiation of dislocation motion in a RBC model can be studied by applying increasing homogeneous shear strain, ε, in small increments and relaxing the position of the mobile atoms at each increment. The critical value, ε_P, at which the dislocation moves from its initial position gives the Peierls stress $\tau_P = G\varepsilon_P$, where G is the elastic shear modulus. However, the rigid boundaries oppose this motion because their atom coordinates correspond to the initial position of the dislocation. This produces a configuration force on the dislocation that increases as it moves nearer the boundary. This leads to an overestimation of the Peierls stress [32], which can be up to almost an order of magnitude in low Peierls stress crystals (see, e.g. Ref. [31]). Also, stress cannot be applied with this model.

2.2. Flexible boundary model

Green's function boundary conditions (GFBCs) offer a more sophisticated technique, for they allow flexible boundaries to be simulated according to the elastic and/or lattice properties of the crystal, thereby enabling the boundaries to distort in response to the dislocation. (The displacement at point $\boldsymbol{x}$ due to an infinitesimal force $\boldsymbol{F}$ at point $\boldsymbol{x}'$ is $\boldsymbol{u} = \boldsymbol{G}(\boldsymbol{x} - \boldsymbol{x}')\boldsymbol{F}$, where $\boldsymbol{G}$ is the Green's function.) Two-dimensional (2D) [33] and three-dimensional (3D) [31,34,35] realisations of GFBCs have been suggested and applied in studies of cracks and dislocations.

The simulation cell consists of three regions shown schematically in Fig. 1(b). The linear elastic displacement field of the dislocation is initially applied to the whole model, after which atoms in region MR are relaxed with their forces derived from an interatomic potential, whilst their neighbours in the Green's function region (GFR) and continuum region (CR) are held fixed. This results in non-zero forces on atoms in the GFR. These forces are then relaxed by displacing atoms in both the GFR (displacements calculated from the lattice Green's function) and the outer CR (displacements calculated via the elastic Green's function). The process is repeated until forces in the GFR fall below a chosen value. In practice, up to 10 iterations may be necessary to achieve reasonable accuracy for dislocation core structure and energy. For details see Refs [31,35].

The GFBC technique has several advantages over simpler RBC methods. It allows a significant reduction in the minimum size of the inner region required to reproduce the correct core structure and Peierls stress [31]. Also, for the same number of atoms in the inner region, the dislocation can move further without strong interference from the boundaries, although a dislocation–boundary distance of typically ~ 15–$20a_0$ is required for reasonable results. The method is particularly attractive for simulations where the number of atoms has to be kept small because calculation of interatomic forces is computationally time-consuming, e.g. *ab initio* or many-body interactions [36–38]. However, self-consistent convergence with GFBCs requires many force calls and calculations of long-range Green's functions, and results in lower computational efficiency than the RBC method for problems

involving a large number of atoms. Examples of two simulations are given in Section 2.6.

2.3. Periodic array model

The GFBC model is not suited to simulation of dynamic conditions (temperature $T>0\,\mathrm{K}$). Both the RBC and GFBC methods suffer from additional limitations. First, as already mentioned, the boundaries are not transparent and the dislocation cannot travel over long distances. Second, they are compatible with application of only external strain and not stress: when the dislocation moves under applied strain, the stress, which arises from the elastic part of the strain only, decreases and constant applied stress simulations cannot be performed. A way to circumvent these problems is to use a periodic array of dislocations (PAD), as proposed initially by Daw et al. [39]. The simulated crystal containing an initially straight dislocation has PBCs in the dislocation glide plane, i.e. not only in the dislocation line direction (y) but also in the glide direction (x), thereby creating an infinite array of infinitely long, parallel dislocations. The dislocation still experiences model-size effects due to interaction with its periodic images but the effect is constant throughout the simulation cell, irrespective of the dislocation position relative to the cell boundaries. Effects of external loading can be studied by applying either stress or strain, and the dislocation can glide over a long (in principle, infinite) distance because of transparency associated with PBCs. Models based on a PAD are computationally efficient for a large number of atoms and, as will be shown later, can be used for not only qualitative but also quantitative studies of DD and mechanisms, and for parameterisation of the processes linking the atomic and continuum approaches.

To illustrate the method, we consider first in Section 2.3.1 a general approach for creating periodicity in the glide plane of a dislocation and then present two particular examples of edge (Section 2.3.2) and screw dislocations (Section 2.3.3). Treatment of the BCs in the direction normal to the glide plane and ways in which external loading is applied are discussed in Section 2.4.

2.3.1. Formal description of creating periodicity

The following approach provides a formal prescription for generating PBCs along both the dislocation line (y-axis) and its direction of motion (x-axis) for a dislocation of any character. It follows from the fact that the Burgers vector $\boldsymbol{b}$ of a perfect dislocation is a translation vector of the lattice, usually the shortest lattice vector. It can therefore be described as the difference between two other lattice vectors. The prescription is as follows.

(i) Construct two half crystals, which we label λ (upper) and μ (lower), with the same orientation.
(ii) Select lattice translations vectors $\boldsymbol{t}_\lambda$ and $\boldsymbol{t}_\mu$ in λ and μ such that $\boldsymbol{b} = (\boldsymbol{t}_\lambda - \boldsymbol{t}_\mu)$.

(iii) Strain λ and μ by e_λ and e_μ, respectively, to bring $\boldsymbol{t}_\lambda$ and $\boldsymbol{t}_\mu$ into coincidence so that after straining $\boldsymbol{t}_\lambda = \boldsymbol{t}_\mu = \boldsymbol{t}^*$, where $\boldsymbol{t}^*$ is to be the translation vector for periodicity, L_x, along x.

(iv) Glue the half crystals together and relax the atoms. The model now contains a dislocation along y with $\boldsymbol{b} = (\boldsymbol{t}_\lambda - \boldsymbol{t}_\mu)$.

The procedure is shown schematically in Fig. 2 for positive edge and right-handed screw dislocations. The left-hand sketch in each case shows the two half-crystals (in cross-section in (a) and plan view in (b)) and the translation vectors $\boldsymbol{t}_\lambda$ and $\boldsymbol{t}_\mu$ whose difference gives $\boldsymbol{b}$. The right-hand figures show the models after relaxation when viewed in the $+y$ direction ($-y$ out of the paper): the displacements (with respect to $+y$) associated with the shear strains e_λ and e_μ used in (b) are indicated at the outer corners of the screw figures. All models have periodicity with translation vector $\boldsymbol{t}^*$. The RH/FS convention (e.g. Ref. [2]) is used to define the sense of $\boldsymbol{b}$, i.e. with positive line sense out of the paper, $\boldsymbol{b}$ is as indicated by the arrow in (a) and the arrow head in (b). The strains used to bring $\boldsymbol{t}_\lambda$ and $\boldsymbol{t}_\mu$ into coincidence account for the stress-free distortion introduced in the simulation cell by the dislocation. They are minimised by making L_x as long as possible.

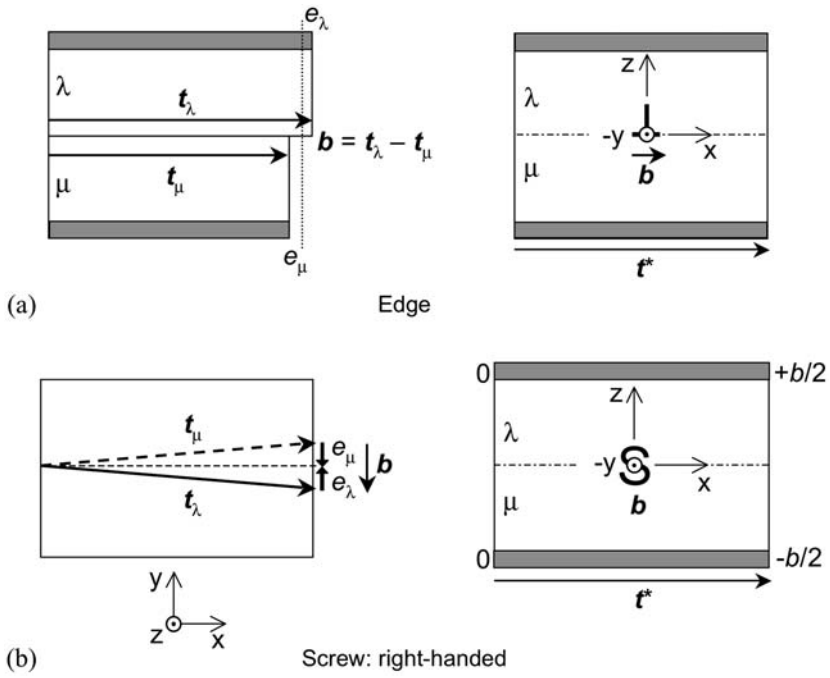

Fig. 2. Procedure for creating (a) positive edge and (b) right-handed screw dislocations by straining, joining and relaxing half crystals λ and μ. The dislocation line lies along the y-axis and slips in the x direction in all cases. As explained in Section 2.4, shaded regions at the $\pm z$ faces here and in Fig. 3 are used to apply stress or strain to the dislocated model.

A similar method can be used to create PAD models for interfacial dislocations such as twinning dislocations. In this case, λ and μ have different orientation and the dislocation forms a step in the twin boundary ([40], see p. 173 of Ref. [2]). Nevertheless, by appropriate choice of $\boldsymbol{t}_\lambda$ and $\boldsymbol{t}_\mu$ such that $(\boldsymbol{t}_\lambda - \boldsymbol{t}_\mu)$ equals $\boldsymbol{b}$ of the twinning dislocation, periodicity can be exploited to study the long-range motion of the boundary (e.g. Ref. [41]).

Practicalities for the edge and screw dislocations in a single crystal are considered in more detail in the following two sections.

2.3.2. *Model for an edge dislocation*

The initial stress-free structure consists of λ and μ with N and $(N-1)$ y–z lattice planes with spacing b, respectively, as in Fig. 3(a). They are strained by $-1/2N$ and $1/2(N-1)$ to have the same length, L_x, in the x direction before being joined along the slip plane x–y, as in Fig. 3(b). During relaxation to form the edge dislocation, λ and μ are constrained so that they retain the same size L_x along x. The dislocation thus formed is *not* a 'misfit dislocation', which arises between half-crystals with different natural (stress-free) lattice parameters and results in an interface with zero dislocation content (see, e.g. p. 181 of Ref. [2] and the appendix of Ref. [42]). The strains used to remove the size difference b between λ and μ can be distributed in different ways, but the most obvious, which results in the lowest energy, has the misfit distributed approximately equally between them. It amounts to changing the cell length in direction x by $+b/2$ and $-b/2$ in the upper and lower halves of the simulation cell respectively.

Imposition of periodicity in the rectangular cell shown in Fig. 3(b) results in application of a bending moment to the dislocated crystal because, as recalled in Fig. 4(a), an edge dislocation bends an unconstrained crystal. Forcing the crystal into the rectangular cell of Fig. 4(b), which is equivalent to Fig. 3(b), causes

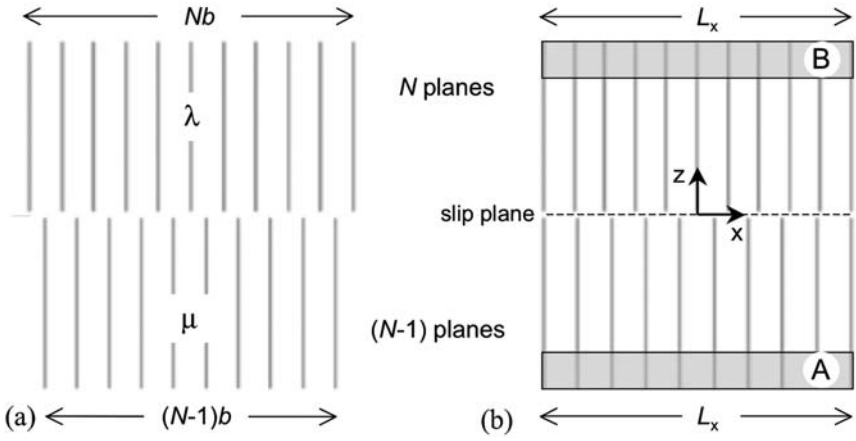

Fig. 3. Schematic illustration of construction of an edge dislocation.

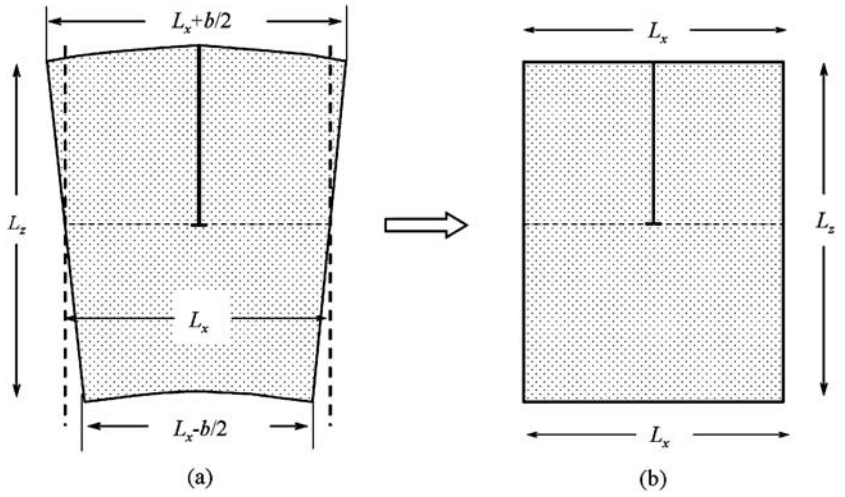

Fig. 4. (a) Unconstrained and (b) constrained crystal containing an edge dislocation.

additional stress in the model. However, the bending moment decreases as L_x/L_z increases. Furthermore, if the dislocation slip plane coincides with the neutral axis, i.e. is in the middle plane of the crystal, the unbending stress is zero. The internal stress distribution in the vicinity of the dislocation core is then close to that of a dislocation in an unconstrained medium [42]. The contribution of the additional stress is maximum for atoms near the top and bottom of the model, well away from the dislocation core (see, e.g. Fig. 7 of Ref. [42]).

Another consequence of periodicity in the x direction is that the dislocation in the computational cell experiences a shear stress σ_{xz} (and hence a glide force) due to its image in all the periodic cells. The largest value (due to one of its nearest-neighbour images) is of the order Gb/L_x. However, the net shear stress is zero for a straight dislocation because σ_{xz} due to an image on the right is opposite in sign to that due to the equivalent one on the left. It is non-zero for curved dislocations, but remains small. Also, as in the RBC model, the Peierls stress increases when L_x decreases. The variation is slow but may be of importance for low Peierls stress crystals.

2.3.3. Model for a screw dislocation

The procedure follows that for the edge dislocation, but with important differences. The x–z planes perpendicular to the chosen direction of the dislocation line are sketched for the perfect crystal in Fig. 5(a). When the atoms are displaced by the screw dislocation displacement field given by isotropic elasticity theory, i.e.

$$u_y = \frac{b}{2\pi}\arctan\left(\frac{z}{x}\right), \tag{2}$$

the cell is transformed to that in Fig. 5(b). The x–z planes form a helicoidal surface of pitch b and intersect the central x–y plane with a shift $\pm b/2$ between the $x<0$ and $x>0$ surfaces.

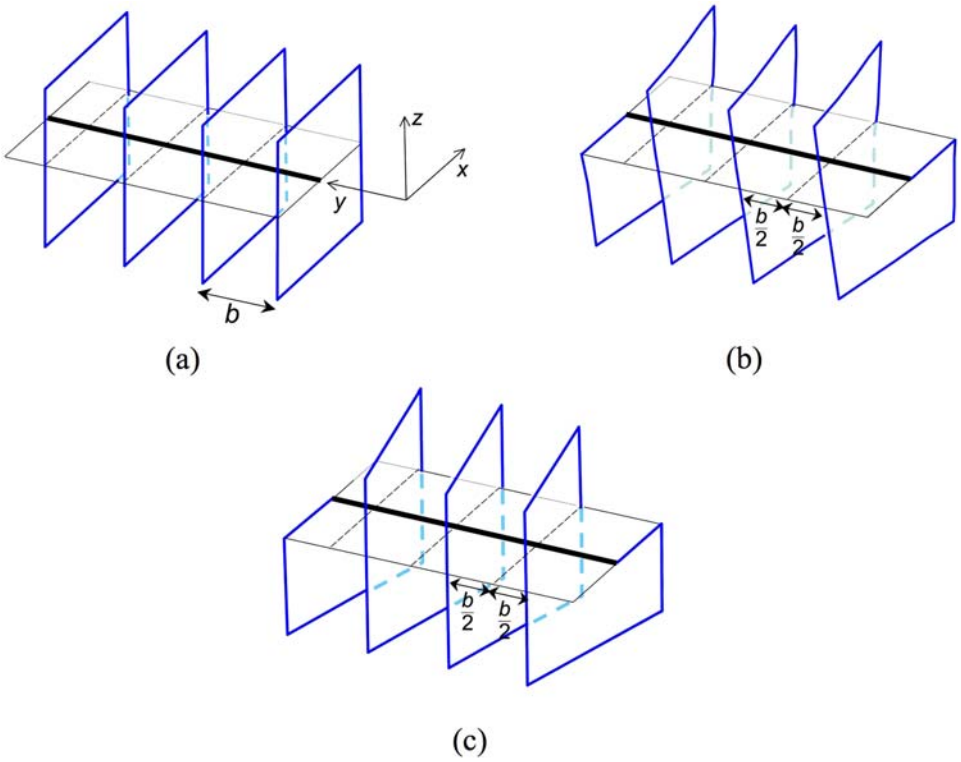

Fig. 5. Creation of a left-handed screw dislocation ($\boldsymbol{b} = [0, b, 0]$ and positive line sense −y) showing the effect on the atomic planes perpendicular to the y-axis. (a) Perfect crystal, (b) crystal with elastic displacements for an infinite medium and (c) effect of imposing PBCs in the x-direction.

Periodicity along y is ensured by the independence of u_y on y, but periodicity in the x direction is not achieved as easily as in the edge model because of the $\pm b/2$ shifts in the y direction across the $\pm x$ surfaces. Some authors (e.g. Refs [43,44]) have avoided this difficulty by treating the boundaries in the $\pm x$ direction as free surfaces, i.e. free space in the regions $|x| > L_x/2$. However, this solution suffers from the same limitations as the RBC method, i.e. the dislocation experiences an image force (attractive in this case) that increases as it moves away from the central position $x = 0$. Also, there is no possibility of long-range motion.

A PAD with PBCs in the x direction can be created, however, by adding a displacement $\pm b/2$ to the y coordinate of atoms that cross the $\pm x$ boundaries in order to put the x–z planes near the central x–y plane into coincidence. The periodic cell on the right ($x > L_x/2$) is generated by adding L_x and $b/2$ to the x and y coordinates, respectively, of atoms in the inner region: the corresponding displacements have opposite sign for the periodic cell on the left. This is equivalent to using a cell which is not a parallelepiped. This method has been used by several authors, e.g. Refs [45–48].

In both the edge and screw models, shifts $\pm \boldsymbol{b}/2$ are added across the $\pm x$ surfaces in the Burgers vector direction. As seen above, in the edge case, it amounts to an expansion of the cell along with a bending moment. In the screw case, it results in shearing the cell. Also, inspection of Fig. 5(b) reveals that the x–z planes are not vertical in the $\pm x$ surfaces but are inclined with angles of opposite sign in the $x<0$ and $x>0$ surfaces. Imposition of PBCs forces these planes to become vertical, as shown in Fig. 5(c), which is equivalent to applying a torque in the $\pm x$ surfaces. The influence of this torque is difficult to evaluate but it decreases with the ratio L_z/L_x. A PAD model for a mixed dislocation can be created by mixing the edge and screw shifts.

2.4. Boundary conditions in the z-direction and loading techniques

Boundary conditions at the $\pm z$ surfaces are important because action due to external loading is applied there. It is clear from Figs 3(b) and 5(c) for the edge and screw dislocations, respectively, that PBCs cannot be used, and free BCs can only be employed when external load effects are not of interest. Two choices for the $\pm z$ boundaries are possible: either rigid or pseudo-free. In the former case, an atomic block (of thickness exceeding the range of the interatomic potential) is created at each boundary with atoms fixed in their initial, strained position [42]. These are represented by the shaded regions in Figs 2 and 3. A second possibility is to create free space in the regions $|z|>L_z/2$. The $\pm z$ surfaces can be either fully free [49,50] or constrained to 2D dynamics by allowing surface atom motion only in directions x and y [51,52]. This condition is compatible only with stress-controlled simulations, whereas rigid boundaries can be used for either stress- or strain-controlled simulations.

Consider the model shown schematically in Fig. 3. A dislocation lies along the y axis perpendicular to the paper and was formed by the process described in Section 2.3, wherein atoms in the inner region, MR, are free to move in static or dynamic simulations. Blocks A and B at the $\pm z$ surfaces are used to apply external action and atoms in them are either fixed in their initial position relative to each other using RBCs or free to move in any direction using free boundary conditions. The primary glide plane is the plane $z = 0$. The glide force per unit length of dislocation line is given by $F = \tau b$, where τ is the component of stress resolved on the glide plane in the direction of $\boldsymbol{b}$, i.e. σ_{xz} and σ_{yz} for the edge and screw, respectively. F due to external action can be generated in two ways, as follows.

(i) *Shear strain ε applied*. Either one or both of the blocks A and B can be used to apply a strain, but for simplicity we assume that A is fixed and the dislocation moves when actions are applied to B. Application of shear displacement $\boldsymbol{u} = [u_x, u_y, 0]$ produces shear strain components

$$\varepsilon_{xz} = \frac{u_x}{L_z} \text{ and } \varepsilon_{yz} = \frac{u_y}{L_z}. \tag{3}$$

Rigid boundaries are required for A and B in order to maintain this strain during the relaxation of the mobile atoms. The corresponding applied shear stress components σ_{xz} and σ_{yz}, which create a glide force on the edge

and screw components of the dislocation, respectively, are calculated from the total force $\boldsymbol{F}^{\mathrm{B}} = [F_x^{\mathrm{B}}, F_y^{\mathrm{B}}, F_z^{\mathrm{B}}]$ on all the atoms in B (which at equilibrium is equal to the total force, $\boldsymbol{F}^{\mathrm{A}}$, on A) by the relations:

$$\sigma_{xz} = -\frac{F_x^{\mathrm{B}}}{\mathrm{A}_{xy}} \text{ and } \sigma_{yz} = -\frac{F_y^{\mathrm{B}}}{\mathrm{A}_{xy}}, \tag{4}$$

where $\mathrm{A}_{xy} = L_x L_y$ is the x–y cross-section area of the crystallite of mobile atoms.

(ii) *Shear stress τ applied*. For stress loading, a shear force $\boldsymbol{F} = [F_x, F_y, 0]$ is applied either to the atoms in block B, which is allowed to move rigidly while block A is held fixed, or as $\boldsymbol{F}$ applied to B and $-\boldsymbol{F}$ to A if A and B are either free or both allowed to move rigidly. The force components are chosen such that the required stresses $\sigma_{xz} = F_x/\mathrm{A}_{xy}$ and $\sigma_{yz} = F_y/\mathrm{A}_{xy}$ are applied. The shear strain components resulting from the applied stress are calculated from $\boldsymbol{u}$ as in eq. (3). In the case of free boundary conditions, u_x and u_y are the average differences of displacement of atoms in A and B.

Note that in order to apply a strain, e.g. ε_{xz}, only the average difference in displacement in direction x between blocks A and B has to be fixed while the atomic displacements in directions y and z can be unconstrained. As a result, another possibility to apply a strain is to constrain only the position of the centre of gravity of the blocks A and B and not the position of every atom [53]. This is achieved by subtracting at every simulation step the average force on a block from the forces on atoms within it, i.e. for atoms in B, $F_x = F_x - \langle F_x \rangle^{\mathrm{B}}$ and similarly for atoms in A.

There are several differences between application of external action for simulation by MS ($T = 0\,\mathrm{K}$) and MD ($T > 0\,\mathrm{K}$). In MS, increasing strain can be applied in increments, with potential energy minimisation performed after every increment. In case (ii) the potential energy is the internal energy computed with the interatomic potential from the position of the atoms minus the work of the applied stress ($= \boldsymbol{F}(\boldsymbol{u}^{\mathrm{B}} - \boldsymbol{u}^{\mathrm{A}})$). With free boundaries, $\boldsymbol{u}^{\mathrm{A}}$ and $\boldsymbol{u}^{\mathrm{B}}$ are the average displacements in the two blocks. In MD simulations, both forms of external loading can be used. For scenario (i), the model crystal has to be equilibrated at the chosen temperature and shear strain then applied at a given rate by imposing velocity $\boldsymbol{v} = [v_x, v_y, 0]$ on B, with stress calculated from $\boldsymbol{F}^{\mathrm{B}}$ (eq. (4)). In scenario (ii), constant shear stress or stress rate can be applied by imposing constant or increasing shear force $\boldsymbol{F} = [F_x, F_y, 0]$ after equilibration. With RBCs, B is free to move under the combined influence of external force $\boldsymbol{F}$ and internal force $\boldsymbol{F}^{\mathrm{B}}$ and has to be treated as a separate super-particle of mass M_{B} with an equation of motion coupled with those of all mobile atoms. The corresponding shear strain rate at any instant is calculated from $\boldsymbol{v}/L_z$. (Again, with free boundary conditions v is the average atomic velocity in B.) A feature of PAD models pointed out in Ref. [42] is that dislocation motion obeys the Orowan relationship between mobile dislocation density, ρ_{D}, dislocation velocity, v_{D}, and the resulting plastic shear

strain rate (see, e.g. Ref. [2]). After integration over time, t, with constant ρ_D, this law takes the form

$$\varepsilon = \int v_D b \rho_D \mathrm{d}t = \bar{x} b \rho_D = \bar{x} \frac{b}{L_x L_z}, \tag{5}$$

where $\bar{x}$ is the mean distance of dislocation motion.

2.5. Restrictions on model parameters

Available computing power limits the size and complexity of atomic models that can be simulated. The total CPU time required is proportional to the product of the number of atoms and the number of MS relaxation iterations or MD time-steps. With the models presented in Sections 2.1–2.3, the boundary conditions in the glide direction result in forces on the dislocation due to either periodic or image dislocations, but their influence can be made minimal if the model is large enough. The PAD method is particularly favourable because the periodic images remain at constant distance from the dislocation. Also, even with scalar computing, it is possible to simulate cell volumes that correspond to large but realistic dislocation density ρ_D. For example, a model of a metal with dimensions $L_x = 25\,\mathrm{nm}$, $L_y = 40\,\mathrm{nm}$, $L_z = 25\,\mathrm{nm}$ containing one dislocation has $\rho_D = 1/L_x L_z = 1.6 \times 10^{15}$ m^{-2}, which is within the range found experimentally in heavily cold-worked metals. It contains approximately 2,000,000 mobile atoms, a number that can be simulated easily with a scalar computer and empirical interatomic potentials. With one obstacle to dislocation motion in the cell, i.e. a periodic obstacle spacing of 40 nm, the model is representative of many real situations. By using parallel computing, ρ_D can be reduced by at least an order of magnitude.

To illustrate the suitability of models of this size, Fig. 6 contains shear stress versus shear strain plots for MS simulation of glide of an edge dislocation through a periodic row of 2 nm voids in Fe at $T = 0\,\mathrm{K}$ [42]. (Here and throughout the text, we use Fe to denote α-Fe, the stable BCC phase of pure iron below 911 °C at atmospheric pressure.) The plots correspond to three models of different size, each containing one void. (The form of these plots is explained in Section 4.2.1.) The critical (maximum) shear stress is seen to be independent of L_x (C1 and C2) and to be halved when L_z is doubled (C3), as expected from elasticity theory (see Section 4.2.3, eqs (13) and (14)). The limitation on model dimensions imposed by computing power is therefore not significant for the problems to be discussed in later sections.

Restrictions on timescale are more serious, however, and lead to values of plastic strain rate, $\dot{\varepsilon}$, in MD simulations that are high compared to experiment. To illustrate, consider glide of a dislocation across the $25 \times 40 \times 25\,\mathrm{nm}^3$ simulation cell above. The maximum MD time-step required to maintain accuracy is typically in the range 1–5 fs, depending on T, so a simulated time of 10 ns requires between 10^7 and 2×10^6 time-steps. Assuming the computer code runs at 10^{-6} s of CPU time per atom per time-step, the total CPU time for the simulation is in the range 46–231 days. For the dislocation to glide the distance L_x in this time, its velocity, v_D, has to

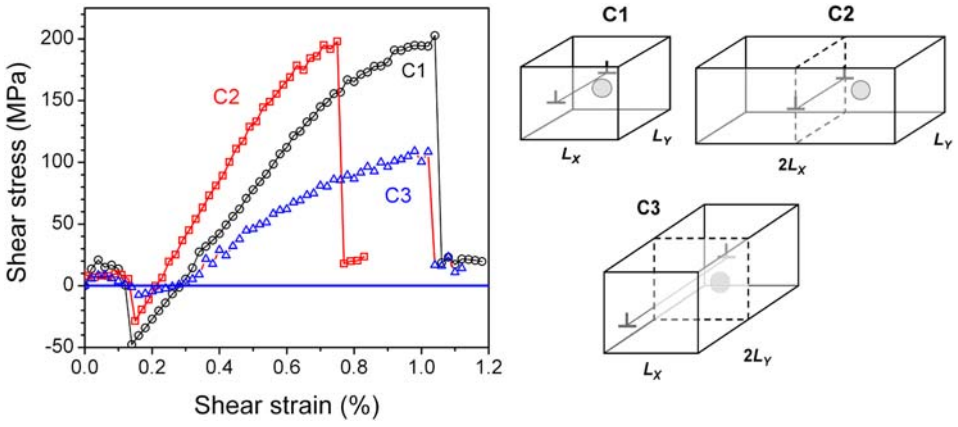

Fig. 6. Stress–strain curves for glide of an edge dislocation through a row of 2 nm voids in Fe for models of different size. $L_x = 30\,\text{nm}$, $L_y = 41.4\,\text{nm}$. Approximate number of atoms: C1 $= 2 \times 10^6$, C2 and C3 $= 4 \times 10^6$. (From Ref. [42].)

equal $2.5\,\text{ms}^{-1}$ and the strain rate that has to be imposed on the model is, from eq. (5) with $b = 0.25\,\text{nm}$, $\dot{\varepsilon} = \rho_D b v_D = 10^6\ \text{s}^{-1}$. In fact, most studies in the literature have used $\dot{\varepsilon}$ in the range 10^6–$10^8\,\text{s}^{-1}$. These values are more than 10 orders of magnitude larger than the typical strain rate of $10^{-4}\,\text{s}^{-1}$ applied to macroscopic tensile specimens in laboratory tests. With such a difference, even massively parallel computing cannot bridge the gap between simulation and experiment. Note, however, that v_D in MD simulations is realistic for dislocations in free flight when the applied stress is tens to hundreds of MPa. Also, in real tensile tests dislocations spend most of the time immobile in contact with obstacles and not in free flight, so that the applied strain rate mainly controls the contact time with obstacles and not the free flight velocity.

The high values of $\dot{\varepsilon}$ place restrictions on the MD simulation of thermally activated processes. There may be several possible unpinning mechanisms for a dislocation blocked by an obstacle. If some can be thermally activated, the probability of their occurrence is directly proportional to the time the dislocation spends in contact with the obstacle, which is limited in simulation to times of the order of 10 ns. Now consider a typical experiment with $\dot{\varepsilon} = 10^{-4}\ \text{s}^{-1}$, $\rho_D = 10^{12}\,\text{m}^{-2}$ and distance between obstacles $L = 10^{-6}\,\text{m}$. The apparent value of v_D from Orowan's law is $4 \times 10^{-7}\,\text{ms}^{-1}$. If the time of free flight between obstacles can be neglected compared with the waiting time at an obstacle, Δt, then $\Delta t = L/v_D = 2.5\,\text{s}$. Thus, the time a dislocation can spend in contact with an obstacle in an MD simulation is about 10 orders of magnitude shorter and the probability of a thermally activated process occurring is small. In other words, because $\dot{\varepsilon}$ is high, the stress in the model increases rapidly, which decreases the activation enthalpy of the interaction processes and strongly favours athermal processes. Nevertheless, it will be seen in later sections that effects of T and $\dot{\varepsilon}$ are observed in MD simulations of dislocation–obstacle interactions.

2.6. Other practical issues

The pros and cons of the methods reviewed here can be summarised as follows. RBC models are simple to implement and fast for even millions of atoms with short-range empirical interatomic potentials. They are convenient for core structure studies and immobile dislocation–defect interaction simulations, but not for application of external stress or strain. GFBC models overcome some of the disadvantages of rigid boundaries. They are suitable for static conditions ($T = 0\,\mathrm{K}$) and simulations where long-range elastic effects influence dislocation core structure and interaction energy with other defects, or when the interatomic force calculations are computationally expensive and the number of atoms is small. It is not sensible to use them when the dislocation bends strongly under applied strain and sweeps a large area, for such cases require a large inner region and demand large computational resource because of the long-range nature of the elastic Green's function.

The PAD technique has been developed for use with short-range empirical interatomic potentials and has been applied extensively for simulation of dislocation–obstacle interaction under a wide range of conditions, i.e. applied strain at $T = 0\,\mathrm{K}$ and applied strain or stress at $T > 0\,\mathrm{K}$. It is intrinsically less accurate than the GFBC method, but this is more than offset by its computational efficiency for models with up to millions of atoms. To illustrate this, consider glide of an edge dislocation of the $\frac{1}{2}[1\,1\,1](1\,\bar{1}\,0)$ slip system in GFBC and PAD models of Fe containing approximately 0.5×10^6 atoms at 0 K [54]. It encounters a row of 2 nm spherical voids of spacing 20 nm and, under increasing applied strain, overcomes them. (Details of this are presented in Section 4.2.1.) The dislocation shape in the glide plane at the maximum stress when the dislocation breaks away is shown in Fig. 7(a). Both shapes are identical in the vicinity of the void, but forward motion of the dislocation between the voids has been restricted in the GFBC model by the boundaries, which are about $15a_0$ away, where a_0 is the lattice parameter. The dislocation climbs in both cases by absorbing vacancies as it leaves the void, as shown in Fig. 7(b). The CPU time with the GFBC method was more than one order larger than with the PAD model, demonstrating that the latter offers similar accuracy with much smaller computational resource.

A model-specific effect can arise when the PAD model is used to study the reaction of a screw dislocation with an obstacle. It will be seen in Sections 4 and 5 that if the dislocation absorbs point defects from an obstacle, it acquires a helical turn. This can glide along the dislocation line, i.e. in the direction of $\boldsymbol{b}$, and, if L is short and $\dot{\varepsilon}$ or τ are low, it can move through a periodic boundary and reappear on the other side of the original obstacle, thereby restoring it. The dislocation usually changes its slip plane by double cross-slip in this process. We do not consider that this simulates a real reaction.

Finally, since a strength of atomic-scale modelling is its ability to simulate processes in the dislocation core, it is important to visualise and identify structure in this region. For the edge dislocation with $\boldsymbol{b} = \frac{1}{2}[1\,1\,1]$ in the BCC metal considered above, a simple analysis of atomic disregistry in the core provides satisfactory

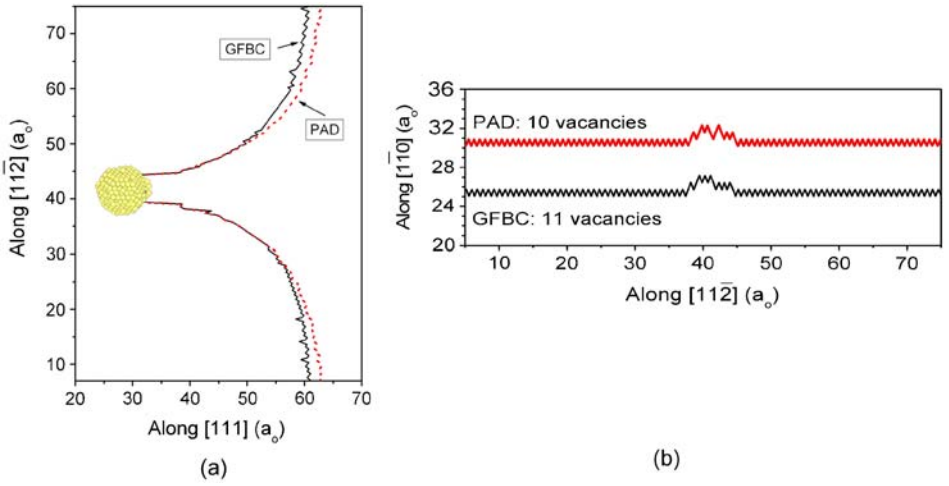

Fig. 7. (a) Comparison of the line shape at the critical stress for a ½[1 1 1](1 $\bar{1}$ 0) edge dislocation overcoming a row of 2 nm voids in Fe at 0 K simulated with GFBCs and PAD models. (b) [1 1 1] projection of line shape after dislocation breakaway showing climb by absorption of vacancies. Scale unit a_0 = lattice parameter. (From Ref. [54].)

results for MS and MD simulations [42]. Atomic positions in each (1 1 $\bar{2}$) atomic plane perpendicular to the dislocation line are considered. The point of maximum relative [1 1 1] displacement between two nearest-neighbour atoms in the [1 1 1] direction and an atom in the adjacent (1 $\bar{1}$ 0) plane is taken as the intersection of the dislocation line with that (1 1 $\bar{2}$) plane. By treating all (1 1 $\bar{2}$) planes, one can determine the location of the whole dislocation line, including kinks and jogs. The line shapes in Fig. 7 were obtained in this way. The technique can be applied easily for the screw dislocation in cases when the core is compact. It is less suitable for metals where the dislocation dissociates.

Other geometrical methods are available, based for example on the analysis of the centro-symmetry of atomic environments [1] or on the comparison of local atomic environments with perfect reference crystals [45]. In the latter case, 12 neighbours in FCC coordination in an FCC metal correspond to the perfect structure, whereas 9 indicates the HCP arrangement, i.e. a stacking fault, 11 or 10 first neighbours occur at partial dislocations and lower coordination can occur in other crystalline defects. This method can be adapted easily for BCC [44] and HCP metals [55,56]. It has proved effective in detecting and distinguishing product dislocation segments formed in complex reactions in BCC metals by combining it with identification of atoms with high potential energy [57]. Thermal fluctuations at high T and $\dot{\varepsilon}$ can cause noise. To exclude this, the analysis is repeated over a short period of time (every 10 time-steps during 100–200 time-steps) and only those atoms which remain in defective environments during this time period are shown. This procedure works well for T up to $\sim$600 K and $\dot{\varepsilon}$ up to $\sim 10^8\,s^{-1}$. More complicated and/or rigorous methods based on local structure analysis of

neighbours [58] or Voronoi polyhedra analysis [59] can also be applied, but usually at a cost to CPU time.

3. Dislocation glide in pure metals and solid solutions

3.1. Glide in pure crystals

The basic controllers of dislocation glide are the nature of the bonding between atoms and the crystal structure of the metal itself [60], for they determine the arrangement of atoms in the core region of a dislocation. The mobility of dislocations depends strongly on the ability of the core to spread. (See Refs [5,6] for recent reviews.) If a metastable stacking fault can form on a plane by shear displacement between atoms, this may lead to dissociation of a dislocation with perfect $\boldsymbol{b}$ into partial dislocations separated by a fault and hence a relatively wide core. Crystal symmetry guarantees an extremum on the stacking fault energy surface (also known as the γ-surface) for some slip systems in metals [61], e.g. $\frac{1}{2}\langle 1\,1\,0\rangle\{1\,1\,1\}$ in FCC and $1/3\langle 1\,1\,\bar{2}\,0\rangle(0\,0\,0\,1)$ in HCP, but not others, e.g. $\frac{1}{2}\langle 1\,1\,1\rangle\{1\,1\,0\}$ or $\frac{1}{2}\langle 1\,1\,1\rangle\{1\,1\,2\}$ in BCC and $1/3\langle 1\,1\,\bar{2}\,0\rangle\{1\,0\,\bar{1}\,0\}$ in HCP. Whether or not a stable fault occurs in the latter cases depends on the atomic bonding: *ab initio* calculations indicate that one does occur in the HCP metal zirconium [62] but not in the BCC metals [63]. We now consider dislocation motion against the intrinsic resistance of the lattice, remembering that the interatomic potential used for the simulation should provide a good description of the core structure, whether at rest or moving, in the metal being modelled.

3.1.1. Glide at 0 K: the Peierls stress

Because of the periodic nature of the crystal lattice, the energy of a straight dislocation varies periodically as it glides, with minima (the Peierls valleys) separated by maxima (the Peierls barriers). In this chapter, the Peierls stress, τ_P, is taken to be the minimum applied shear stress resolved in the slip direction on the slip plane needed to overcome the Peierls barrier at 0 K. It can be as high as 0.5% of the shear modulus in BCC [64] and HCP [65] metals where screw dislocations have non-planar core structures, and in covalent semiconductors [66] where dislocation glide requires bond swapping. The Peierls stress can be determined from MS simulations by applying either increasing shear strain, ε, and therefore stress, τ, until the dislocation moves at $\tau = \tau_P$. In principle, all types of model boundary conditions described in Section 2 can be used but, as explained there, the resistance of the boundary with RBCs or GFBCs can influence dislocation glide, and hence the value of τ_P. This is particularly so when τ_P is low [32].

The Peierls stress depends on the metal and the interatomic potential. Consider the plots in Fig. 8, obtained for straight edge dislocations in PAD models under shear loading (Section 2.4) for (a) Fe [67] and (b) α-Zr [68]. In Fe, the two potentials predict similar elastic constants, no metastable stacking faults and almost identical core structures for perfect dislocations [57], yet the value of τ_P differs by a

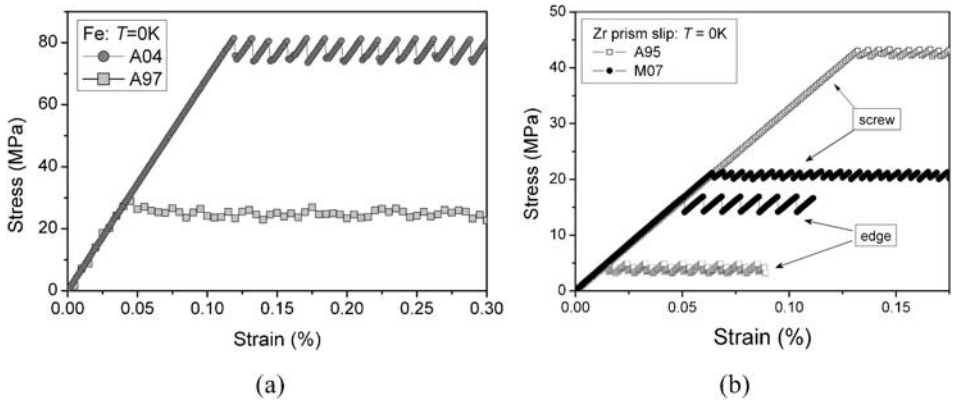

Fig. 8. Plots of τ versus ε for glide at 0 K of (a) ½[1 1 1](1 $\bar{1}$ 0) edge dislocation in Fe (from Ref. [67]) and (b) 1/3⟨1 1 $\bar{2}$ 0⟩{1 0 $\bar{1}$ 0} edge and screw dislocations in Zr (from Ref. [68]). The labels for the interatomic potentials are A97 [69] and A04 [70] for Fe, and A95 [71] and M07 [72] for Zr.

factor of more than three. (The elastic modulus, G, for [1 1 1](1 $\bar{1}$ 0) shear in Fe is 73 GPa, so τ_P/G is approximately 0.3×10^{-3} and 1.1×10^{-3} for the A97 and A04 models, respectively.) The two potentials used for Zr also give the same elastic constants and lattice parameter ratio, and both predict stable intrinsic faults on the basal and prism planes, although the fault energy, γ, is different in the two models [68]. Again, these different potentials result in markedly different τ_P values for the same slip system, as shown in (b). (G for ⟨1 1 $\bar{2}$ 0⟩{1 0 $\bar{1}$ 0} shear in α-Zr is 34 GPa, so τ_P/G is approximately 0.2×10^{-3} and 0.5×10^{-3} for the edge dislocation with the A95 and M07 potentials, respectively, and 1.3×10^{-3} and 0.7×10^{-3}, respectively, for the screw dislocation.) The difference between results for τ_P for the same metal indicates that caution must be exercised in attaching weight to values of the Peierls stress obtained in this way.

Nevertheless, some effects are seen in such simulations that are consistent with experiments and their interpretation. The edge dislocation tends to have a wider core and lower τ_P than the screw of the same slip system in the same metal. Edge dislocations dissociate and have low τ_P values ($\sim 10^{-4}G$) on the {1 1 1} planes of FCC metals and (0 0 0 1) planes of the HCP metals that have a low-energy, basal stacking fault. τ_P/G is higher for glide of the edge dislocation on any planes of BCC metals and on the prism plane of HCP metals. Ease of glide of screw dislocations is determined by the possible existence of a non-planar core structure [5]. τ_P is low in the FCC metals because dissociation on a {1 1 1} plane results in a planar core, and likewise in HCP metals with a low-energy basal stacking fault. It is higher for prism slip in HCP metals when the screw core spreads only on the basal plane or simultaneously on the prism and basal planes if faults occur with similar energy in both planes.

Screw dislocations in BCC metals have high τ_P, usually above 1 GPa, because of their non-planar core. Two structures have been found, depending on the

interatomic potential: a threefold degenerate core, proposed initially in Ref. [64] and predicted by early pair potentials (see Ref. [29]), and a non-degenerate compact core, first observed in simplified MS simulations based on interaction potentials between rows of atoms [73] and later predicted by *ab initio* calculations [38,63] and the interatomic potential in [70]. However, τ_P is somewhat ill-defined for the BCC screw. With some potentials that predict a degenerate core [30,44], the dislocation advances by one atomic distance at a lower critical stress and adopts a metastable sessile structure. It remains immobile until an upper critical stress is reached and motion then becomes unbounded. Also, τ_P is sensitive to non-Schmid components in the applied stress, particularly normal stress perpendicular to the glide plane [44,74]. (See also Refs [5,6].)

3.1.2. Glide at finite temperature

The minimum applied resolved shear stress for dislocation glide at $T>0\,\mathrm{K}$ is less than τ_P because of thermal activation. When the stress is high enough so that a dislocation no longer feels the Peierls stress, its free-flight motion has a viscous character with steady-state velocity, v_D, proportional to the resolved shear stress τ

$$v_D = \frac{\tau b}{B}, \tag{6}$$

where B is a friction coefficient. With increasing stress, v_D falls below values given by eq. (6) and tends asymptotically to the transverse sound velocity of the material ($\sim$few kms^{-1}). B has various origins in real materials [75], but in MD simulations is controlled solely by phonon damping. MD simulations using PAD models to determine v_D as a function of τ yield values of B in the range 1–100 μPas [52,76–78]. Examples of data obtained by simulation for v_D versus τ at 100 and 300 K for the edge dislocation in the two models of Fe used for Fig. 8(a) are presented in Fig. 9. It is seen that the potential from Ref. [70], which gives the higher τ_P, also results in lower v_D for the same value of τ. With log–log scales, the plots are linear with gradient equal to 1, as expected from eq. (6), and the value of B increases with increasing T due to increasing phonon damping. The relation between B and T was shown to be linear in FCC metals and Fe [52,77], in agreement with Leibfried's theory of phonon damping [75].

As proposed initially by Seeger [79], a dislocation in a high Peierls stress crystal at $T>0\,\mathrm{K}$ and low τ spends most of its time aligned with the bottom of a Peierls valley until thermally activated nucleation of a kink-pair moves part of it into the next valley. Subsequent propagation of the kinks along the line transfers the rest of the dislocation to the new position. An early expression based on an analogy between a dislocation and a vibrating string was proposed by Friedel [80]:

$$v_D = d\omega_D \frac{b}{l_c}\frac{L}{l_c}\exp\left(-\frac{\Delta H(\tau)}{k_B T}\right), \tag{7}$$

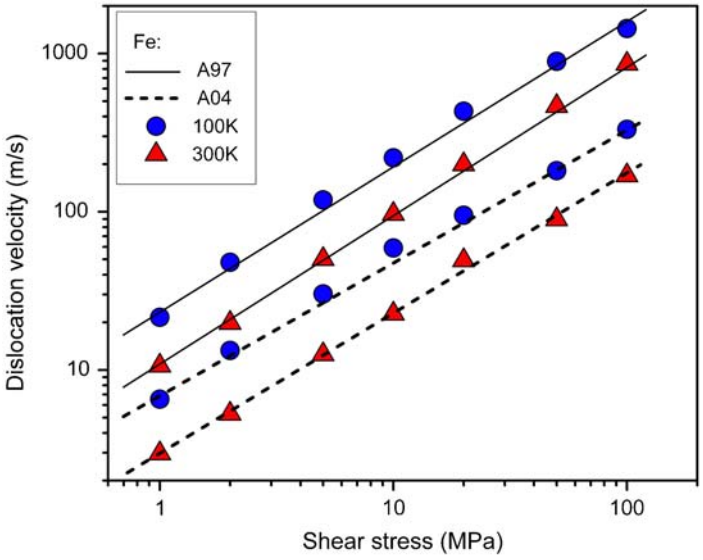

Fig. 9. Plots of v_D versus τ for edge dislocation glide at $T>0$ K on the ½[1 1 1](1 $\bar{1}$ 0) slip system in Fe. The two potentials A97 [69] and A04 [70] are those used in Fig. 8(a).

where d is the distance between Peierls valleys, ω_D a characteristic frequency close to the Debye frequency, L the dislocation length and l_c the size of the critical kink-pair nucleus. ΔH is the activation enthalpy of the kink-pair nucleus and is a decreasing function of τ.

This velocity relation has been checked at the atomic-scale by Rodney [53] from a comparison between MS and MD simulations for a Lomer dislocation in an FCC model of Al. The MS simulations used the Nudged Elastic Band method [81] to determine minimum energy paths between Peierls valleys at different values of τ. The maximum enthalpy along a given path is $\Delta H(\tau)$. MD simulations were performed at constant applied strain rate, $\dot{\varepsilon} = 1.5 \times 10^7\ \mathrm{s}^{-1}$, and different temperatures. The examples of the stress–strain curves in Fig. 10(a) show that serrations occur with each jump of the dislocation from one Peierls valley to the next. Each jump produces a plastic strain, $\Delta\varepsilon_p$, given by eq. (5) with $\bar{x} = d$, which compensates part of the elastic strain and results in a stress drop $\Delta\tau = G\Delta\varepsilon_p \approx 30$ MPa, where G is the shear modulus. To extract the enthalpy–stress relation, the stress is taken to be the average jump stress and the corresponding ΔH^* is computed from its linear relation with the thermal energy, a dependency well known from experiment [82,83]. Indeed, a characteristic enthalpy ΔH^* is obtained from Orowan's law in steady state and eq. (7):

$$\dot{\varepsilon} = \rho_D b v_D = \rho_D b d \omega_D \frac{bL}{l_c^2} \exp\left(-\frac{\Delta H^*}{k_B T}\right). \tag{8}$$

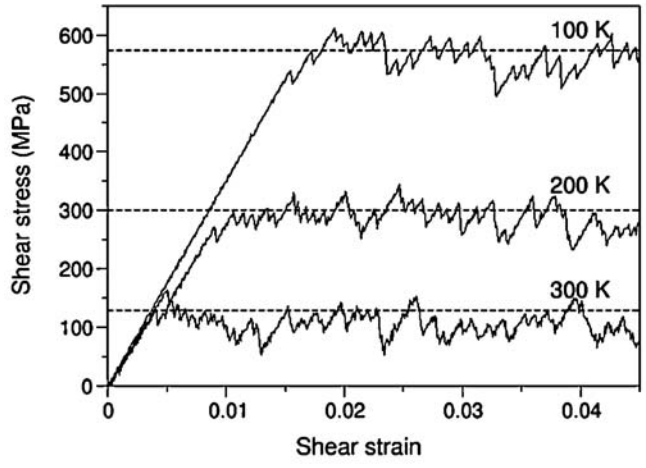

(a)

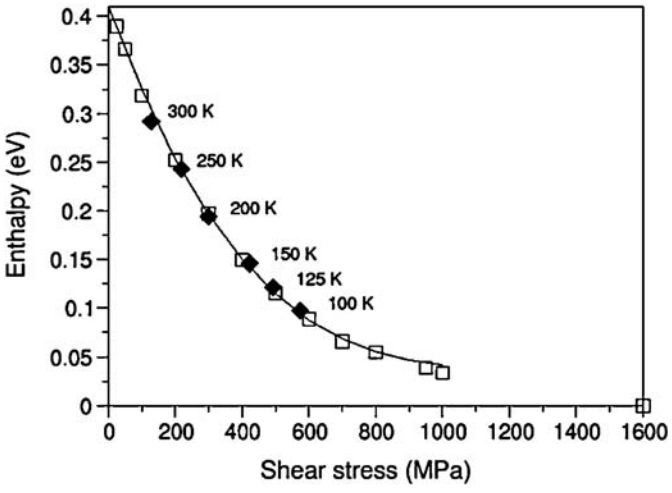

(b)

Fig. 10. (a) Curve of τ versus ε for thermally activated glide of a Lomer dislocation in Al at 100, 200 and 300 K with $\dot{\varepsilon} = 1.5 \times 10^7\ s^{-1}$. (b) Comparison between kink-pair formation enthalpies obtained from static (open squares) and dynamic (filled diamond) simulations. A PAD model was used with free surfaces in the z direction. In the static simulations, the stress was applied by means of external forces in the $\pm z$ surfaces. In the MD simulations, $\dot{\varepsilon}$ was applied by controlling the velocity of the centres of gravity in the $\pm z$ surfaces. (From Ref. [53].)

Taking logarithms of both sides yields

$$\Delta H^* = k_B T \ln\left(\frac{\rho_D b d \omega_D b L}{l_c^2 \dot{\varepsilon}}\right). \quad (9)$$

Setting $\omega_D = 5 \times 10^{13}\,s^{-1}$, $b = d = 0.258\,nm$, $L = 9.7\,nm$ ($= L_y$ of the model), $\rho_D = 10^{-2}\,nm^{-2}$ and $l_c = b$, gives $\Delta H^* = Ck_BT$ with $C = 11.3$. This proportionality coefficient is significantly smaller than that in experiments ($C = 25 \sim 30$) because of the high applied strain rate. Fig. 10(b) compares the enthalpy curve with the result of the static simulations, proving the accuracy of the velocity law of eq. (8) for the range of T and $\dot{\varepsilon}$ explored here.

3.1.3. Comparison with experiment

A striking difference between modelling and experiment is that the Peierls stress predicted from atomic-scale simulations is several times larger than values deduced from experiment. For instance, with the Fe interatomic potentials used above, the Peierls stress for the ½⟨1 1 1⟩ screw dislocation in Fe is above 1 GPa while the experimental value is 400 MPa [84]. A similar observation has been made for potassium [85]. High values have also been obtained with *ab initio* calculations [38], with the exception of molybdenum modelled within the Generalized Pseudopotential Theory [37]. Various explanations have been put forward to explain the discrepancy, such as the effect of kink dynamics [38], stress concentrations [86] and collective behaviour of dislocations [87]. More research is needed to provide better understanding of this discrepancy.

3.2. Glide in solid solutions

3.2.1. Background

The yield and flow stress of a metal can be strongly influenced by the presence of solute atoms, an effect that is exploited in 'alloy strengthening'. Whether in solution (SSH) or in precipitates of a second phase ('precipitation strengthening'), the solute atoms make the metal inhomogeneous at the atomic scale and create a resistance to dislocation glide, e.g. Refs [88,89]. Simulations of solid solutions are described in this section and precipitates are considered in Section 4.

There are two principal issues involved in attempting to model SSH and gain a quantitative estimate of the critical applied stress for glide. One is concerned with the short-range interaction of a dislocation with the solute obstacles, which we return to below. The other arises from the statistical nature of the distribution of obstacles in an alloy. Foreman and Makin [90] made the first computer simulation study of this problem in the approximation of constant line tension to model glide of a dislocation in a field of randomly positioned pinning points, and an analytical treatment was presented by Kocks [91]. More sophisticated approaches to the statistical nature of SSH have also been considered in semi-analytical treatments, e.g. in Refs [92–95]. (A review of some of the earlier models has been presented by Haasen [96].) It is not possible to address this issue quantitatively by MD simulation

because the simulation cells required to obtain results with statistical significance would be too large. Instead, atomic-scale modelling has mainly focused on the interaction between a dislocation and one or a few solute atoms near or within its core.

Until recently, this interaction was derived from the long-range solution obtained by linear elasticity theory. Solutes can be modelled using several descriptions depending on their nature [2–4]. The simplest considers each solute atom to be a centre of dilatation due to its misfit in the solvent crystal. As a result of the associated volume change, a dislocation interacts with the solute if it has a non-zero pressure component in its stress field. The interaction energy decreases as $(r)^{-1}$, where r is the distance from the solute atom to the dislocation core, and can be negative (attractive) or positive (repulsive) depending on the position of the solute atom with respect to the dislocation. If the symmetry of the site occupied by the solute atom is lower than that of the perfect crystal, more than one distinct orientation of that atom must exist, i.e. its distortion field is not spherically symmetric: consequently there is an interaction with the shear stress field of a dislocation, again proportional to $(r)^{-1}$. Substitutional solute atoms in metallic alloys do not lower the symmetry: examples treated by atomic-scale simulation include Cu and Cr in Fe, Al in Ni and Mg in Al (see Section 3.2.2). Interstitial solutes may lower the symmetry, the classic case being that of carbon (C) in Fe, for which the C atom occupies an octahedral site and creates a distortion with tetragonal rather than cubic symmetry (see Section 3.2.3). An induced interaction can also arise if the elastic properties of the solute atom are different from the host crystal. This interaction is of order $(r)^{-2}$.

These descriptions based on elasticity theory break down when r tends to zero, i.e. within the dislocation core, and atomic-scale simulations are adopted. *Ab initio* methods can be used to model single solute atoms or small clusters in the core [97], but, due to their computational cost, cannot be used to simulate dislocation motion in a solid solution. The PAD method and short-range potentials discussed in Section 2 are suitable. Although specific electronic effects of solute atoms cannot be represented by these potentials, properties such as size misfit or symmetry-breaking can.

3.2.2. Substitutional solute atoms

Alloys simulated to date include solutions of Al in Ni (FCC), Mg in Al (FCC) and Cu or Cr in Fe (BCC). A significant source of hardening comes from the short-range interaction of the dislocation with particular configurations of solute atoms, specifically pairs of solute atoms across or along the dislocation glide plane, rather than more diffuse, long-range interaction as in classical SSH theories [96].

In the case of Al in Ni, nearest-neighbour pairs of Al atoms with one atom just below and one just above the dislocation glide plane are strong pinning centres. Rodary et al. [98] simulated the glide of an edge dislocation with PAD boundaries under constant applied shear stress for solute concentration, c, in the range 1–8 at.%. An example is shown in Fig. 11. With the interatomic potential set used, an Al atom is oversized with a volume misfit parameter of 3%. To ensure that the gliding dislocation encountered the most representative random arrangement

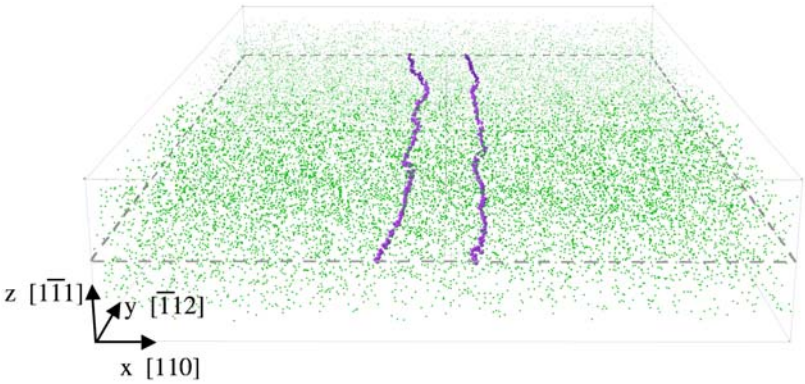

Fig. 11. Dislocation gliding in a Ni–3at.% Al solid solution at 300 K under $\tau = 70$ MPa. The dimensions of the computational cell are $L_x = 30$ nm, $L_y = 43.12$ nm, $L_z = 7.32$ nm. The visualisation shows Al atoms and atoms in the Shockley partial cores which do not have FCC or HCP coordination. (From Ref. [98].)

compatible with overall computing time, the dislocation was allowed to make 20 sweeps of the model via the transparent x boundaries. Dislocation velocity, v_D, was obtained from the average x coordinate of the core atoms. If the dislocation paused for at least 50 ps before completing 20 sweeps, v_D was taken to be zero. Plots of v_D versus τ for pure Ni and 3, 5 and 8at.% alloys are presented in Fig. 12(a). v_D tends to the limit of the transverse velocity of sound at high τ, depends linearly on τ at lower stress and falls to zero at the stress τ_s, which depends on solute concentration. The velocity extrapolates to zero at the stress τ_d. Rodary et al. refer to τ_s and τ_d as the 'static' and 'dynamic' threshold stresses, respectively. These stresses increase linearly with solute concentration, c, as shown by the data in Fig. 13(a). With increasing T, τ_s decreases due to thermally assisted motion of the dislocation over the strong part of the obstacle spectrum, but τ_d is unaffected because it represents the effect of the weak part of the obstacle spectrum.

The MD simulations showed that a significant part of hardening was due to obstacles consisting of Al–Al pairs in nearest-neighbour coordination across the slip plane that are formed from second-neighbour pairs by the passage of the dislocation. This is because glide of a Shockley partial shifts atoms above the glide plane by $1/6\langle 1\,1\,2\rangle$ with respect to those below and thus changes their respective position. A nearest-neighbour Al dimer is highly repulsive in Ni–Al for two reasons. One is elastic in origin and due to the positive misfit. The other is chemical: second-neighbour pairs of Al atoms are energetically favourable over first neighbours because of the stability of the Ni_3Al intermetallic phase, which is included in the interatomic potential. The resistance of Al dimers across the glide plane is not accounted for by elasticity since the interaction with the dilatation field of the solute above the glide plane cancels (at first order) that of the solute below.

In more quantitative studies of SSH in this alloy, Proville et al. [100] and Patinet and Proville [101] measured by static simulations the pinning force and force range

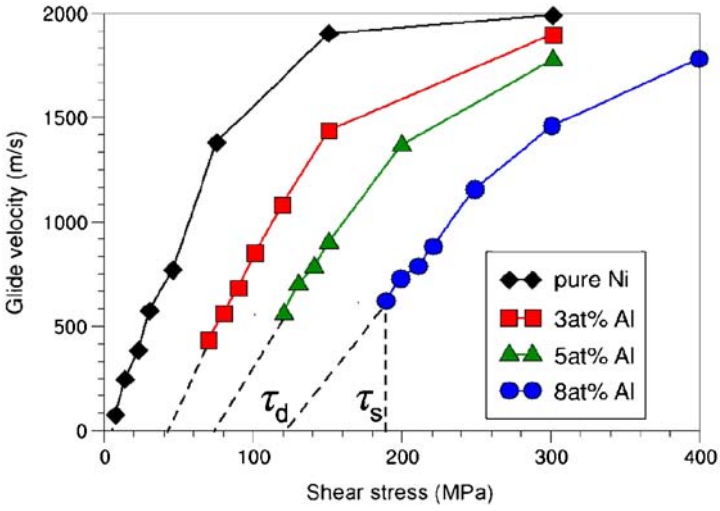

(a)

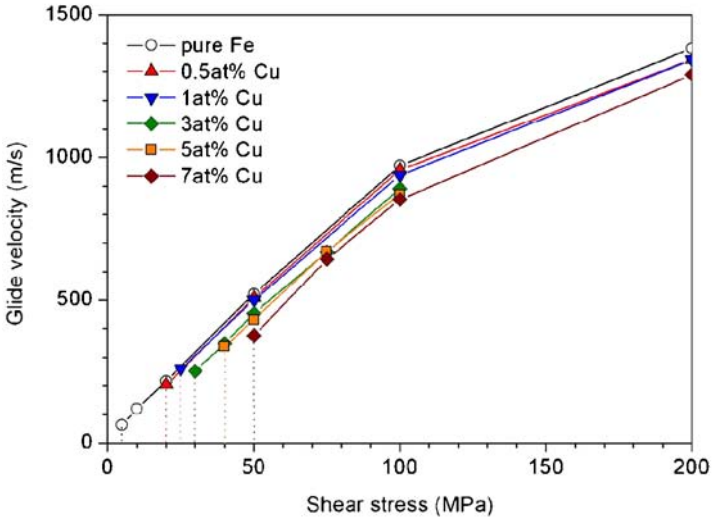

(b)

Fig. 12. Dislocation velocity versus τ at 300 K in (a) Ni–Al (from Ref. [98]) and (b) Fe–Cu (from Ref. [99]).

for single solute atoms and pairs that may or may not cross the glide plane of either screw or edge dislocations. The interaction was found to be significant only when the solutes are just above or below the glide plane. For such short-range configurations, the two Shockley partials of a dislocation interact separately with

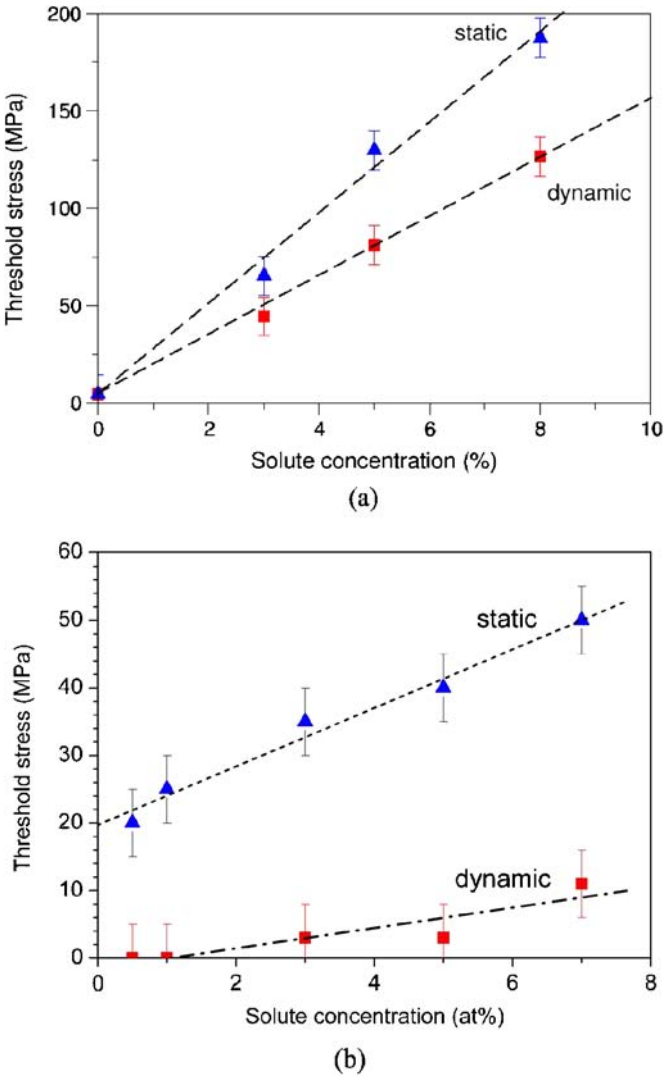

Fig. 13. Concentration dependence of τ_s and τ_d at 300 K in (a) Ni–Al (from Ref. [98]) and (b) Fe–Cu (from Ref. [99]).

the solute atoms and the energy of the solute is always minimum in the stacking fault of the dislocation. As a result, the pinning force on the trailing partial is larger than that on the leading one. Also, since the partials of both edge and screw dislocations have edge components that interact with the dilatation field of solute atoms, the pinning forces on screw and edge dislocations are of same magnitude. This short-range effect is contrary to assumptions in theories of SSH, in which interaction with screws is assumed to be weak because the edge components of their

partials have opposite sign and cancel at large distance. The CRSS at $T = 0\,\mathrm{K}$ for both edge and screw dislocations increases linearly with c at the same rate, about 25–30 MPa/at.%, in agreement with experimental indentation hardness measurements on Ni–Al [102]. The strongest configuration for both edge and screw dislocations is a dimer of solute atoms in the plane just above the glide plane: the pinning force is about twice that for a solute atom in the same plane, which is the location for a single atom with the highest obstacle strength. The second strongest configuration is the dimer that crosses the glide plane, as described above. Pinning forces found by simulation are smaller than estimates obtained by elasticity theory, showing that the latter does not account accurately for the short-range interactions.

The interaction energy of edge and screw dislocations with single solute atoms in the Al–Mg system was computed using cylindrical simulation cells with RBCs and no loading in Ref. [103]. The interaction energy with the two partials is symmetrical in this case because the dislocation is at rest. As in Ni–Al, the strongest interaction is when the solute atom is in a plane adjacent to the glide plane.

The importance of short-range interactions has also been confirmed for the BCC alloy Fe–Cu, in which Cu is an oversized substitutional solute. MS simulation of motion of the $\frac{1}{2}\langle 1\,1\,1\rangle\{1\,\bar{1}\,0\}$ edge dislocation under increasing strain shows that the critical stress, τ_c, is determined by individual obstacles in the form of either single Cu atoms or pairs of solute atoms adjacent to the glide plane [99]. For single atoms, τ_c is highest when the solute occupies a site in the plane immediately below the extra half-plane of the dislocation. It is the one that gives the maximum attractive interaction energy with the dislocation. For Cu–Cu doublets, the maximum τ_c is approximately 50% higher than that for one solute atom and occurs for the first-neighbour pair in the plane immediately below the extra half-plane. This configuration is equivalent to the strongest obstacle pair in Ni–Al, except that in that case the pair is above the glide plane. By varying the model size in the simulations of individual obstacles, τ_c was found to be approximately proportional to the reciprocal of the spacing of strong obstacles along the dislocation line, a result consistent with the continuum treatment of localised-obstacle strengthening.

MD simulation of edge dislocation glide in Fe–Cu solid solutions at $T > 0\,\mathrm{K}$ revealed similar behaviour to that in Ni–Al discussed above, i.e. smooth motion with constant velocity at high τ and irregular motion with pauses and complete stops at low τ [99]. Plots for v_D versus τ in Fe–Cu solutions at 300 K are shown in Fig. 12(b). They have similar form to those for Ni–Al in (a), but v_D at a given stress is much less sensitive to change in c. The threshold stresses τ_s and τ_d defined in Fig. 12(a) are plotted as functions of c for Fe–Cu in Fig. 13(b). Both increase linearly with c, but, unlike those for Ni–Al, do not extrapolate to the same value at $c = 0$. Tapasa et al. note that dislocation glide in the equivalent simulation of pure Fe occurs at $\tau \sim 1$ MPa, so even a concentration as small as 0.5at.% of Cu in Fe has a significant effect on τ_s.

Rodary et al. [98] have pointed out that the linear dependence of τ_s on c is consistent with the importance of the strongest obstacles in the solute spectrum, because, according to Friedel statistics [80], the stress at which a dislocation moves

across a field of point obstacles is proportional to the square root of obstacle density, and the density of *pairs* of solute atoms is proportional to solute concentration. It is also consistent with interpretation of the experimental concentration-dependence of hardening in Cu–Mn solid solutions, according to which pairs of Mn atoms are responsible for the hardening [104].

3.2.3. Interstitial solute atoms

The important role of carbon interstitial solute in the phenomena of yielding and strain ageing in steel was first treated theoretically via elasticity in [105]. The significance of the interaction of carbon atoms with the dislocation core itself was identified, but it has been possible only recently to examine this within the scope of large-scale atomic simulations. Potentials that accurately reproduce all important properties of C in Fe have not been available, so Tapasa et al. [106] employed a combination of the EAM interatomic potential for Fe–Fe interaction from Ref. [69] and a pair potential for Fe–C interaction from Ref. [107], which models an atom having the same octahedral site and distortion field as C in Fe and similar migration energy. Carbon in this low symmetry site creates a tetragonal distortion, for it repels its two first-neighbour Fe atoms in a $\langle 1\,0\,0 \rangle$ direction and attracts its four second neighbours in the two transverse $\langle 0\,1\,1 \rangle$ directions. Thus, C solutes are located in either a $(1\,\bar{1}\,0)$ atomic plane parallel to the dislocation glide plane (with tetragonal distortion axis (TDA) in the [0 0 1] direction) or sites between two $(1\,\bar{1}\,0)$ planes (with [1 0 0] or [0 1 0] TDAs symmetric about $\boldsymbol{b}$).

Tapasa et al. [106] used MS to investigate the interaction energy of the edge dislocation with a C atom in sites near the slip plane. Sites half an interplanar spacing below the $(1\,\bar{1}\,0)$ plane at the bottom of the extra half-plane have the highest binding energy, $E_b = 0.68$ eV. C atoms in sites within $(1\,\bar{1}\,0)$ atomic planes have a maximum E_b of 0.5 eV when located one below the extra half-plane. These values compare with the elasticity estimate of about 0.5 eV obtained in Ref. [105] and values in the range 0.5–0.8 eV calculated later when the influence of the tetrahedral distortion was taken into account, e.g. Refs [108–111]. This distortion gives rise to C interaction with the $\frac{1}{2}\langle 1\,1\,1 \rangle$ screw dislocation, for which E_b is predicted to be approximately 40% of the value for the edge [111]. Interestingly, Becquart et al. [112] have recently developed a new potential for a C atom in Fe using *ab initio* data and find that the maximum E_b for the screw dislocation is 0.41 eV. Thus, although maximum binding occurs inside the core region where linear elasticity is not strictly valid, the E_b value it gives for C in Fe is consistent with the atomic-level treatments.

Simulations of solutions of C have not been made, but the critical stress, τ_c, at which an edge dislocation overcomes a row of single C atoms in sites of high binding and spacing $L = 3.51$ or 11.23 nm at $T = 0$ K and > 0 K has been determined [106]. Examples of the critical line shapes are shown in Fig. 14. The τ_c values for these conditions are 466, 146 and 50 MPa, respectively. The critical stress at $T = 0$ K has an L^{-1} dependence consistent with strengthening due to point obstacles with barrier energy E_b. The temperature-dependence of τ_c in the model with $L = 3.51$ nm is plotted in Fig. 15 for three values of $\dot{\varepsilon}$. τ_c decreases strongly with

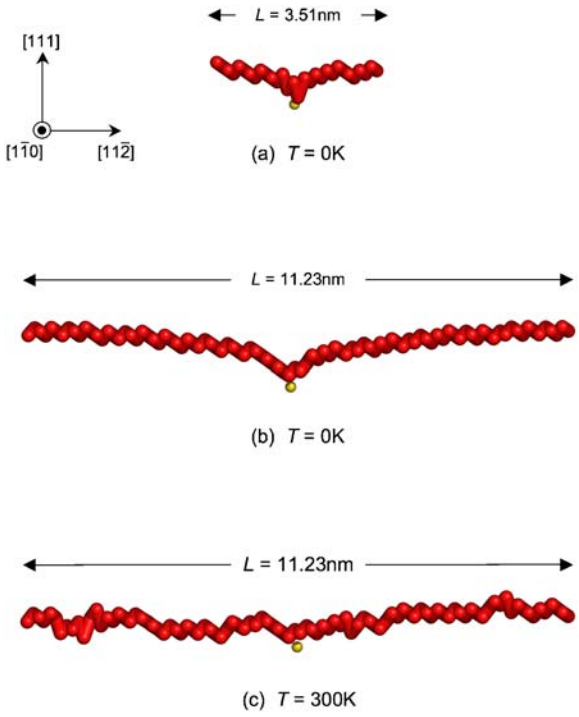

Fig. 14. Edge dislocation shape (visualised by atoms in the core) at τ_c for a carbon atom (small sphere) in the site of maximum binding energy, E_b, in Fe crystals at (a, b) $T = 0\,K$ for two different spacings, L, between carbon atoms and (c) $T = 300\,K$. The applied strain rate is $\dot{\varepsilon} = 5 \times 10^6\ s^{-1}$. (From Ref. [106].)

increasing T at low T and increases with increasing $\dot{\varepsilon}$. It is small and largely independent of T above about 300 K. Carbon atom migration within the core occurs during the time the dislocation is pinned when $T \geq 800\,K$, but extensive drag of solute does not occur at the applied strain rates accessible to MD simulation because the dislocation jumps forward by too large a distance as it unpins for a C atom to be recaptured.

Tapasa et al. deduced the activation parameters for slip in this atomic-scale model with the following treatment. Dislocations slip by overcoming barriers, each of which exerts a resisting force with a profile such that the area under the force–distance curve equals the total energy, E_b. (See, e.g. Refs [2,113,114].) At $T > 0\,K$, the energy required is partly provided as mechanical work by the applied load: it is written $\tau_c bLd^*$ or $\tau_c V^*$, where d^* and V^* are the activation distance and volume, respectively. The remainder is thermal and has to overcome the free energy of activation $\Delta G^* = E_b^* - \tau_c V^*$, where E_b^* is the total energy required between the dislocation states separated by d^*. ΔG^* is the Gibbs free energy change at constant T and $\dot{\varepsilon}$ between those two states. The probability of ΔG^* being provided by thermal fluctuations is $\exp(-\Delta G^*/k_B T)$ if $\Delta G^* \gg k_B T$. Hence, from eq. (8) the

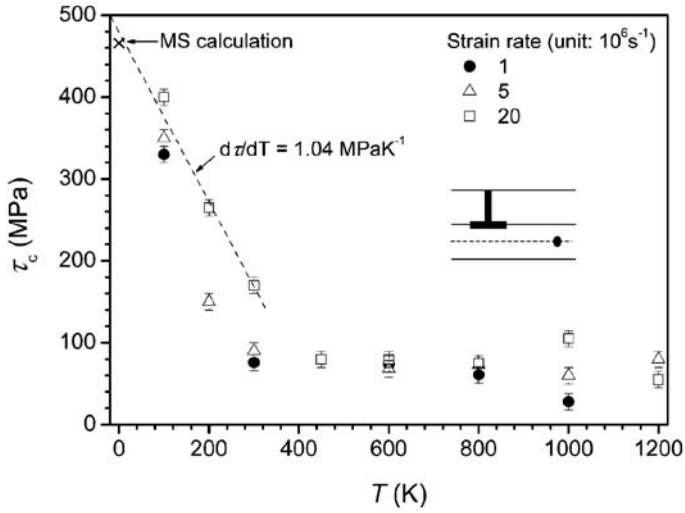

Fig. 15. Temperature dependence of τ_c for a carbon atom in the site of maximum E_b with $L = 3.51$ nm. The dashed line indicates $\partial\tau_c/\partial T$ in the region of strong temperature-dependence. (From Ref. [106].)

macroscopic plastic strain rate is

$$\dot{\varepsilon} = \rho_D A \exp\left(\frac{-\Delta H^*}{k_B T}\right), \tag{10}$$

where $A = bDv$. D is the glide distance between each obstacle overcome and v the effective attempt frequency. G^* has been replaced by the enthalpy H^* by taking the entropy term in $\dot{\varepsilon}$ to be unity.

In experiments, ΔH^* and V^* are determined from tensile tests at constant T and constant $\dot{\varepsilon}$. If a change in $\dot{\varepsilon}$ from $\dot{\varepsilon}_1$ to $\dot{\varepsilon}_2$ causes a change $\Delta\tau_c$ in the flow stress at constant T, then V^* can be obtained from

$$V^* = \frac{k_B T \ln(\dot{\varepsilon}_2/\dot{\varepsilon}_1)}{\Delta\tau_c}. \tag{11}$$

The activation enthalpy is obtained from tests over a range of T at constant $\dot{\varepsilon}$ by using the relation

$$\Delta H^* = -V^* T \left(\frac{\partial\tau_c}{\partial T}\right)_{\dot{\varepsilon}}. \tag{12}$$

Tapasa et al. applied these equations to the MD data in Fig. 15. $\Delta\tau_c = 42$ MPa when $\dot{\varepsilon}$ decreases from 20 to $5 \times 10^6\,s^{-1}$ at $T = 100$ K, which gives $V^* = 2.9b^3$ from eq. (11). The values at 200 K and 300 K are $2.2b^3$ and $4.7b^3$, respectively. Since L is 3.51 nm ($=14b$), d^* is approximately 0.2–0.3b, which is reasonable for an interstitial atom. Use of eq. (12) with these V^* values and the gradient of the dashed τ_c versus T line in Fig. 15 gives $\Delta H^* = 0.03$, 0.05 and 0.14 eV for $T = 100$, 200 and

300 K, respectively, i.e. 3–6$k_B T$. This energy is much smaller than $E_b = 0.68$ eV that has to be overcome by the dislocation at $T = 0$ K. This exposes a limitation of MD for simulation of thermally activated dislocation processes already mentioned in Section 2.5. The unavoidably high $\dot{\varepsilon}$ limits the time available for activation and results in small values of ΔH^*, as mentioned at the end of Section 3.1.2. This conclusion was also drawn by Domain and Monnet [43], who used MD simulation of glide of a ½⟨1 1 1⟩ screw dislocation in Fe to reveal that ΔH^* is $\sim 20 k_B T$ smaller than that realised in experiment at much smaller strain rate.

3.2.4. Extension to microscopic models

An outstanding issue in relation to MD simulation of SSH is how to incorporate information gained from relatively small models into larger-scale analyses that recognise the statistical nature of dislocation behaviour. Rodary et al. [98] have provided a brief discussion of how results from their MD modelling of Ni–Al might be incorporated in a higher-level, micromechanical approach to predict macroscopic stress–strain curves. Proville et al. [100,101] used the pinning forces and force ranges computed from MS simulations to parameterise analytical expressions of CRSS proposed in various classical theories of SSH [96]. One difficulty is that the theories assume a single type of obstacle whereas simulations exhibit a range of pinning forces depending on obstacle type (single atom or dimer) and position with respect to the glide plane. A generalisation of the Mott–Nabarro model to include several types of obstacles was proposed in Ref. [100] and showed good agreement with MS simulations. Olmsted et al. [103] proposed a semi-analytical approach based on computation of a one-dimensional energy landscape for the motion of a straight edge dislocation through a random field of Mg solutes in Al using the single solute energy values. The stress to unpin a straight edge dislocation trapped in a local energy minimum was estimated and compared with values obtained by MS for a dislocation moving under stress through a random array of solutes. A good agreement was obtained. The thermally activated rate of dislocation unpinning versus τ and T was calculated semi-analytically, and again good agreement was found with results of MD simulations.

A challenge for future work in this area is to provide more accurate information on the motion of dislocation cores containing solute atoms across wide ranges of T and ν_D, and build it into continuum-based models so that effects such as dislocation–dislocation interactions and dislocation climb can be simulated.

4. Voids and precipitates

4.1. Introduction

We now turn to obstacles that are larger than the individual solute atoms considered in Section 3, but are still only up to a few nanometres in size. As noted in Section 1, much of the research using atomic-scale simulation has been driven by the need to investigate the effect of obstacles that are of importance for metals in

current and future nuclear power systems. MD simulation of displacement cascades shows that a significant fraction of the point defects are created in clusters with their own kind. SIA clusters are usually in the form of dislocation loops. The clustered vacancies resulting from radiation damage may have dislocation character, i.e. loops or SFTs. These vacancy clusters also form during annealing of the vacancy supersaturation created by rapid quenching of metals from temperatures just below the melting point. The obstacle properties of dislocation loops and SFTs are considered in Section 5.

In many situations, vacancies cluster to form voids. Voids are common features of the microstructure after either irradiation at high temperature or ageing after quenching. When He atoms are present, e.g. as a result of a transmutation reaction with atoms in the metal, these cavities may contain He gas. Voids are usually of near-spherical shape, with facets on close-packed planes that have low surface energy. It will be seen below that they can offer strong resistance to dislocation motion as a result of direct contact between dislocation and void. The interaction is characterised by the following. It is energetically favourable for a dislocation to intersect a void because its core and strain energy is zero within the cavity. However, this is at least partially offset by the fact that the dislocation has to create a surface step (in the direction of $\boldsymbol{b}$) by shear as it penetrates a void. These two effects determine the obstacle strength of the void, i.e. the magnitude of the applied stress that is necessary for the dislocation to break away. These important details, and the effect of the cavity on the dislocation energy, are not easily modelled using elasticity theory [115].

Precipitates also form a class of obstacle known to be important for the strength of alloys, e.g. Refs [88,89]. For many applications, alloy composition and heat treatment are deliberately chosen to develop a population of precipitates that offers optimum resistance to dislocation motion and is stable in the temperature range required for use. In terms of atomic-scale simulation, such alloys have received little attention because the size and dispersion of their precipitates are such that the strengthening mechanisms are quite well understood from conventional, continuum-based models. Computer simulation has tended to focus on alloy systems where the precipitates are small and research is required to understand the dislocation–precipitate mechanisms at the atomic level. The alloys in question are again important for current and future nuclear power systems. They are Fe–Cu and Fe–Cr, and are also considered in this section.

If the dislocation penetrates and shears a precipitate, the features that determine the obstacle strength may be similar to those mentioned for a void, i.e. an interface step has to be created and the dislocation energy in the precipitate may be different from that in the surrounding matrix, in this case as a result of differences in properties such as the elastic constants and stacking fault energy. Furthermore, the dislocation may induce a change within the precipitate to a more favourable crystal structure, an effect discovered by computer simulation of Cu precipitates in Fe (see below). The features of strengthening are different, however, if the dislocation does not penetrate the precipitate, e.g. if the precipitate is incoherent with the matrix or if the stress state near it is sufficient to induce the dislocation to bypass it by cross-slip.

Important details that determine the critical applied stress and breakaway mechanism are not easily modelled using elasticity theory. For example, the surface step on a void (or interface step around a precipitate) increases in size to b as an edge dislocation is pulled from the obstacle, in contrast to the situation for a screw where it decreases to zero, and the energy of the step may not be known with precision. Furthermore, the effect of a small void or precipitate on the dislocation energy and stress field can only be treated with approximation. Atomic-level simulation incorporates these effects naturally. We first consider the obstacle resistance encountered by edge dislocations due voids in Fe and Cu (Section 4.2.1) and precipitates in Fe (Section 4.2.2) at $T = 0$ K. In this MS modelling, shear strain ε is applied in increments $\Delta\varepsilon$ and the potential energy, E, is minimised after every increment: the applied shear stress,τ, is calculated from the reaction force exerted by the moveable atoms on the rigid outer blocks of atoms (Section 2.5). MS simulation neglects effects due to kinetic energy and provides for direct comparison with continuum modelling of these obstacles (Section 4.2.3). The effects of temperature on void and precipitate strengthening are presented in Section 4.3, and examples of simulations of bubbles and loose clusters of vacancies are described in Section 4.4.

4.2. Edge dislocation–obstacle interaction at $T = 0$ K

4.2.1. Voids

This interaction has been most widely studied for Fe using the interatomic potential from Ref. [69]. The computational cell and BCC crystallographic indices for the edge dislocation are shown schematically in Fig. 16(a). A spherical void of diameter D is placed with its equator on the dislocation slip plane. The periodic spacing of voids in the y direction is L. (From now on, we use L for the obstacle spacing of both edge and screw dislocations, i.e. for L_y and L_x respectively.) Results for 339-vacancy voids ($D = 2$ nm) in a crystal of 2.07 M atoms ($L = 41.4$ nm, $L_x = 29.8$ nm, $L_z = 19.9$ nm) are presented in Fig. 17(a) as curves of τ and ΔE versus ε, where ΔE is the change in E from the initial state when the straight dislocation is far from the row of voids. Four regions are indicated on the plots. The dislocation glides towards the void at the Peierls stress of 23 MPa in region I. It is attracted by, and pulled into, the void in region II: a step of length b is created on the entry surface of the void but E decreases because of the decrease in length of the dislocation. Stress becomes negative because the plastic shear strain due to dislocation motion is larger than the imposed strain: τ does not return to zero until ε increases and the dislocation becomes straight and coincident with the centre-to-centre line of the voids, i.e. the minimum energy configuration is achieved. In region III the dislocation bows between the voids under increasing ε until it is released at the critical resolved shear stress, τ_c. As shown in Fig. 7, visualisation of the atoms in the dislocation core demonstrates that on breaking away, the dislocation absorbs a few vacancies from a void and so acquires a pair of superjogs, i.e. jogs of more than one-atom height. Region IV corresponds to motion of the jogged dislocation. The dependence of the

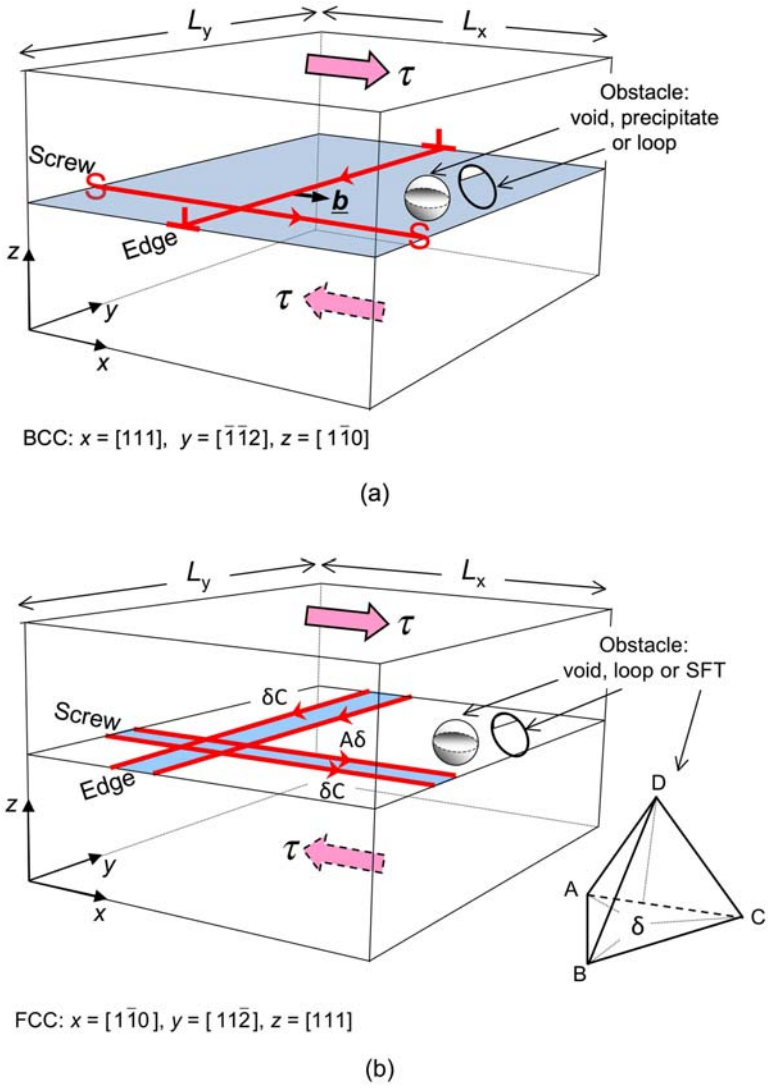

Fig. 16. Schematic illustration of the atomic cell and crystallography used to simulate interaction of dislocations with a row of obstacles in (a) BCC and (b) FCC metals. The sense of positive applied resolved shear stress, τ, is shown. The centre-to-centre spacing of obstacles is L_x and L_y for the screw and edge dislocations, respectively. The tetrahedron in (b) is also used to identify the Burgers vectors and slip planes for the FCC case.

τ–ε plot on D for $L = 62$ nm in Fe at 0 K is shown in Fig. 18. The maximum, τ_c, of each curve varies approximately logarithmically with D for a given L, as can be seen in Fig. 19. Furthermore, it is approximately inversely proportional to L, e.g. for the three values of L shown for the 2 nm void, τ_c varies in the ratio 1:1.40:1.99 while

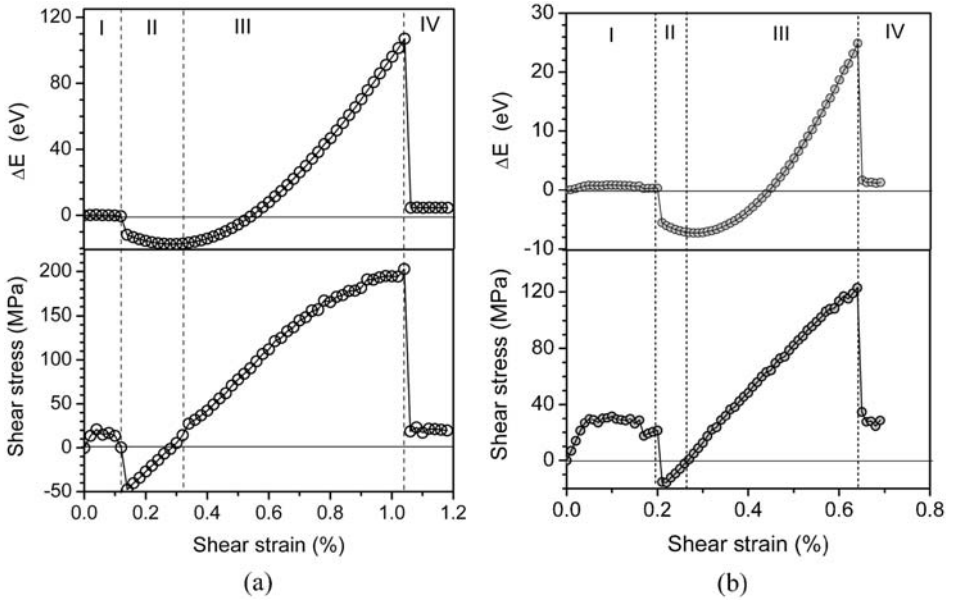

Fig. 17. Change in potential energy and applied stress as functions of applied strain in an Fe crystal at $T = 0\,\mathrm{K}$ containing an edge dislocation ($L = 41.4\,\mathrm{nm}$) gliding through (a) a 2 nm void containing 339 vacancies and (b) a 2 nm precipitate containing 339 Cu atoms. (From Refs [42,116].) Note the difference in the scale of the ordinate axes between (a) and (b).

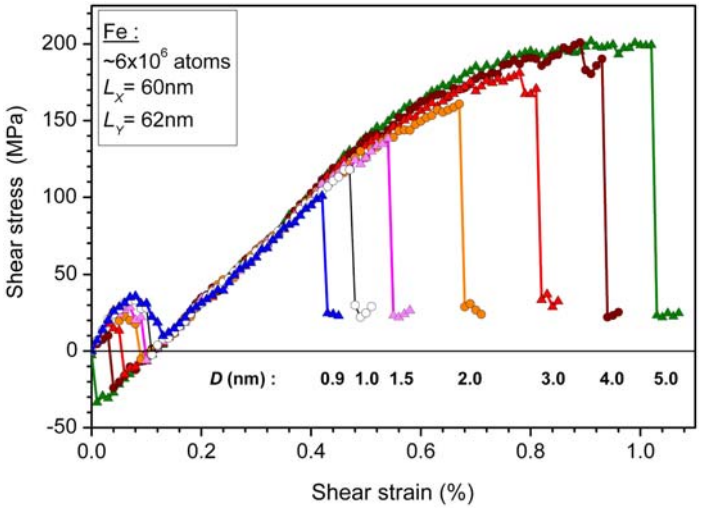

Fig. 18. Stress–strain curves obtained for edge dislocation–void interaction in Fe at 0 K using the interatomic potential from Ref. [69]. The model size and D are indicated. (From Refs [116–119].)

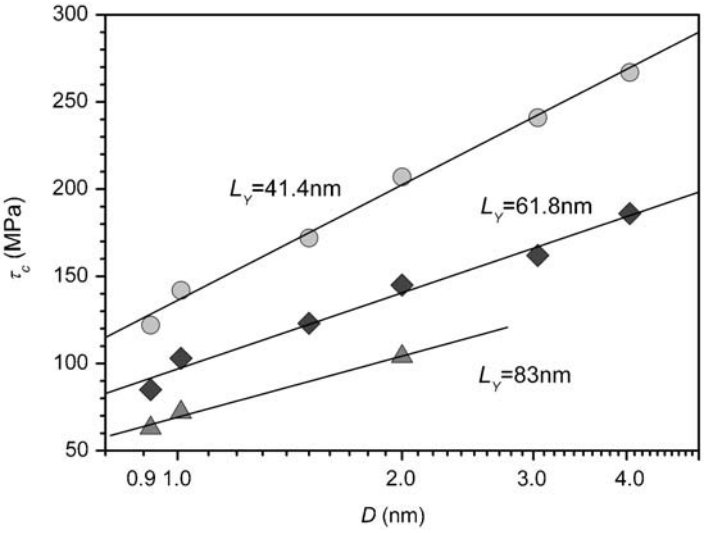

Fig. 19. τ_c versus D (log scale) for rows of voids in Fe at 0 K and three different centre-to-centre spacings, L.

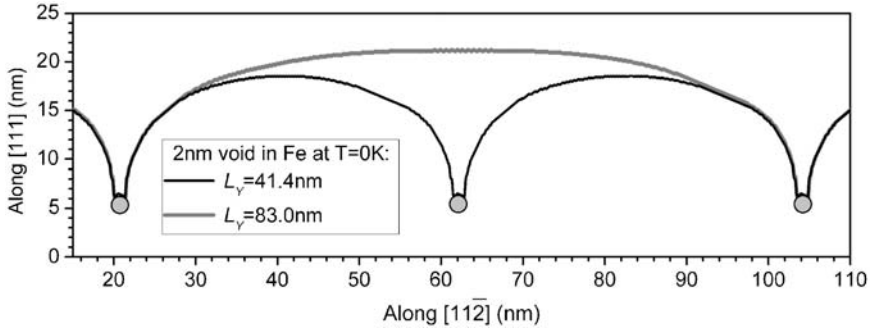

Fig. 20. Shape of the dislocation line at τ_c for 2 nm voids with different spacing, L, in Fe at 0 K. Black line: $L = 41.4$ nm, $\tau_c = 207$ MPa; grey line: $L = 83.6$ nm, $\tau_c = 104$ MPa. Dislocations are visualised by showing atoms in the core. (From Ref. [117].)

L^{-1} varies as 1:1.35:2.02. The shape of the dislocation line in the $(1\ \bar{1}\ 0)$ slip plane at τ_c for crystals with $L = 41.4$ and 83 nm is presented in Fig. 20. The radius of curvature of the line between the obstacles is smaller for the smaller L, i.e. larger τ_c. This, and the L^{-1}-dependence, is as expected from the line tension model of elasticity. However, it should be noted that the dislocation configuration in the vicinity of the voids is almost identical for the two L values, a feature not predicted by that model.

Dislocation line shape in the slip plane at τ_c for voids of different size is presented in Fig. 21 by black lines. (Grey lines are the dislocation shape for Cu precipitate

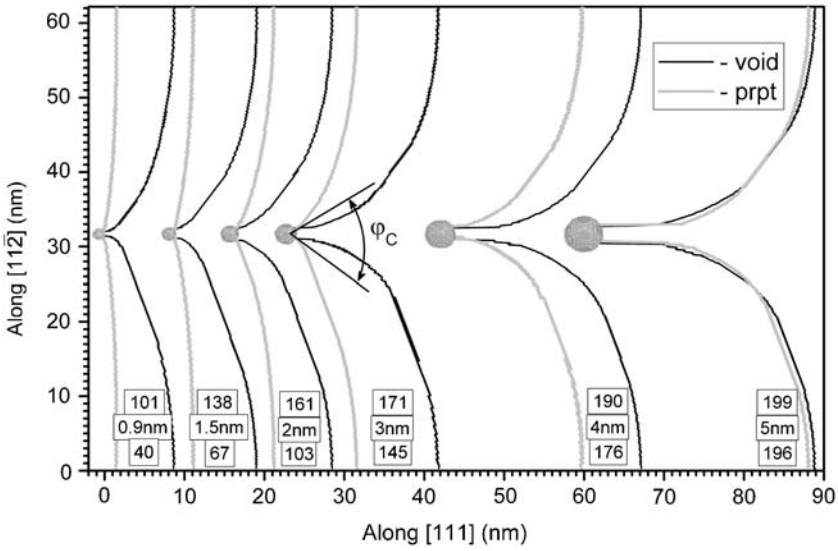

Fig. 21. Critical line shape in the (1 $\bar{1}$ 0) plane for a dislocation passing a row of either spherical voids or Cu precipitates of different size in Fe at 0 K. Spacing $L = 62$ nm and D varies from 0.9 to 5 nm. Black line: shape for voids; grey line: shape for precipitates. The labels for each pair of shapes indicate: τ_c for void, D and τ_c for precipitate, in descending order. (From Ref. [120].)

obstacles discussed in Section 4.2.2). As seen in Fig. 18, small voids with D of up to about 1.5 nm in Fe give an almost linear dependence of τ on ε in region III. The gradient $d\tau/d\varepsilon$ is slightly lower than the elastic shear modulus because of plastic strain due to the bowing dislocation. These small voids offer relatively weak resistance. Larger voids are relatively strong obstacles and the dislocation bows out more before breakaway at τ_c, resulting in decreasing $d\tau/d\varepsilon$ as τ_c is approached. The dislocation bends sufficiently to form a screw dipole in the critical configuration when $D \geq 2$ nm, as shown in Fig. 21. This shape is the same as that for an edge dislocation to overcome a row of impenetrable obstacles by the Orowan mechanism, although an Orowan loop is not left around the obstacle in the void case and the spacing of the dislocations in the dipole is less than D. The mutual attraction due to self-stress of the dislocation segments at the void surface assists their alignment in the screw dipole arrangement and results in the decrease of $d\tau/d\varepsilon$ as the dipole is extended. The dipole length can reach several tens of nanometres for $D > 5$ nm. The mechanism controlling dislocation breakaway is associated with the difficulty of formation of a step on the exit surface of the void, which is believed to be a consequence of the threefold structure of the $\frac{1}{2}\langle 1\,1\,1 \rangle$ screw core. In fact, a simple shear step is not formed. Instead, the edge dislocation climbs by absorbing some vacancies from the void at breakaway (Fig. 7) and the dipole is annihilated by unzipping from the void surface rather than by cross-slip of the screw segments. This effect has been found with two different potentials for Fe [69,70], even though

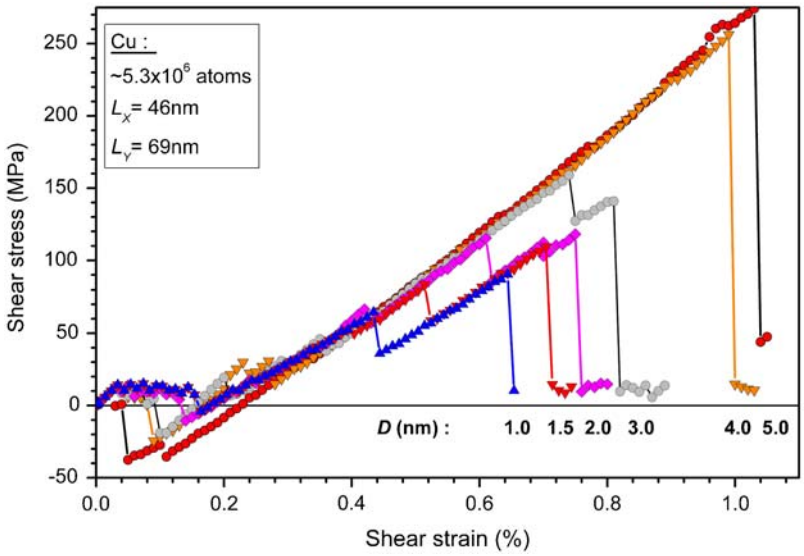

Fig. 22. Stress–strain curves obtained for edge dislocation–void interaction in Cu at 0 K using the interatomic potential from Ref. [121]. The model size and D are indicated. (From Refs [120,122].)

they reproduce different screw core structures [57]. The amount of climb depends on D (see examples in Ref. [116]).

The model orientation for edge dislocation–void interaction in Cu is drawn in Fig. 16(b). The τ–ε plots for 0 K have a similar sequence of regions I–IV to those for Fe, as demonstrated for data for $L = 35$ nm and D in the range 1–5 nm in Fig. 22. However, there are differences in region III as τ rises from 0 to τ due to the difference in the structure of edge dislocations in the two metals. In contrast with Fe, climb does not occur when edge dislocations overcome voids in Cu at 0 K. Furthermore, the τ–ε plots do not show a marked decrease in $d\tau/d\varepsilon$ as τ_c is approached, and there are significant drops in τ for small D before eventual breakaway. These differences from Fe are due to the dissociated dislocation core structure in this FCC metal. For small voids ($D \leq 2$ nm), the first drop in τ occurs when the leading Shockley partial breaks from the void. The step formed by this on the exit surface is a partial step $1/6\langle 1\,1\,2\rangle$ and the stress required is small. Breakaway of the trailing partial determines τ_c. The line shapes in the (1 1 1) plane at these two maxima in τ are shown in Fig. 23. For larger voids, τ_c is controlled by the leading partial and the dislocation breaks away as a whole. Creation of a pure screw segment is not possible and $d\tau/d\varepsilon$ does not decrease by dipole formation. As a consequence of these effects, voids in Cu are weaker obstacles than those in Fe when small and stronger when large. The latter effect arises from the high Peierls stress of one of the partials [120]. The dissociation of the core into distinct partials prevents dislocation climb, but it is possible that in metals with high stacking fault energy, such as Al, constriction of the core could result in dislocation–void interaction more like that in Fe.

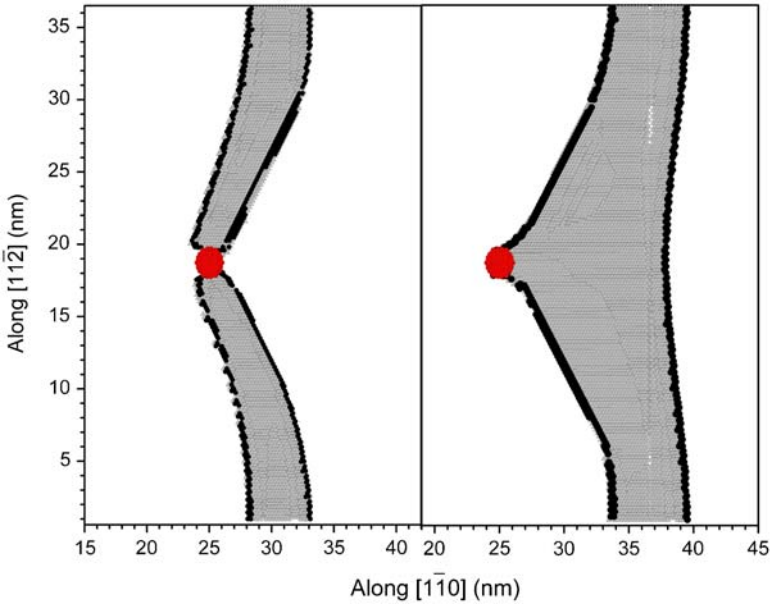

Fig. 23. Critical line shape in the (1 1 1) plane for a dislocation passing a row of 2 nm voids with spacing 35 nm in Cu at 0 K. Left-hand figure: $\tau = 115$ MPa; right-hand figure: $\tau = 118$ MPa. The core region of Shockley partials is shown by black symbols and the stacking fault is grey. (From Ref. [122].)

4.2.2. Precipitates

As noted in Section 4.1, atomic-level simulation of dislocation–precipitate interaction has concentrated on nanoscale precipitates that occur in metals used in nuclear power systems. Among these, Cu in Fe is important because Cu-rich precipitates of small size ($D <$ few nanometres) form during neutron irradiation of ferritic pressure vessel steels that contain small amounts (a few tenths of a percent) of Cu. Cu precipitates that nucleate during thermal ageing of Fe–Cu alloys transform martensically as they grow from the BCC crystal structure coherent with the Fe matrix to a twinned 9R form of the FCC structure. The size at which they transform from BCC to 9R falls in the range from about 4 to 10 nm, depending on the heat treatment (e.g. Ref. [123]). In neutron-irradiated steels, however, Cu precipitates remain small and BCC in structure. Together with radiation damage formed by vacancies and SIAs, they make a significant contribution to irradiation hardening (e.g. Refs [124–126]).

The interaction of an edge dislocation with spherical BCC Cu precipitates coherent with the Fe matrix at 0 K has been simulated for various D and L values using the interatomic potential from Ref. [69] with the model depicted in Fig. 16(a) [116–120,122,127–129]. As anticipated in Section 4.1, some features of the interaction are similar to that for voids. This is illustrated by noting the similar form of the ΔE and τ versus ε plots for rows of 2 nm voids and precipitates in Figs 17(a) and (b), respectively, although the reduction in E when the dislocation

penetrates the obstacle and τ_c are smaller for the precipitate. These differences in magnitude arise from the fact that the precipitate is a region with non-zero modulus and the step on the Cu–Fe interface has lower energy than the free-surface step on a void. Consequently, the dislocation simply shears the precipitate without being pulled into screw orientation. For example, the critical included angle, φ_c, between the dislocation segments at the obstacle surface is 70° for the $D = 3$ nm precipitate compared with 0° for the void of the same size (Fig. 21). Dislocation climb does not occur.

More significant differences between Cu precipitates and voids arise for D greater than about 3 nm. In these larger precipitates, the BCC Cu undergoes a dislocation-induced, partial transformation to a more stable FCC-like structure. This is demonstrated by the projection of atom positions in four atomic planes near the equator of a 4 nm precipitate after dislocation breakaway in Fig. 24. The {1 1 0} planes have a twofold stacking sequence in the BCC metals, as can be seen by the upright and inverted triangle symbols near the outside of the precipitate, but atoms represented by circles are in a different sequence. Atoms away from the Fe–Cu interface are seen to have adopted a threefold sequence characteristic of the {1 1 1} planes in an FCC metal. This transformation, first found in MS simulation of a screw dislocation penetrating a precipitate [130,131], increases the obstacle strength and results in critical line shape (Fig. 21) and τ_c (Fig. 25) that are close to those of voids of the same size. It is also accompanied by formation of jogs on the dislocation as it leaves the precipitate, as seen on the right of Fig. 24. These atomic-level mechanisms are not predicted by continuum treatments, such as the line-tension

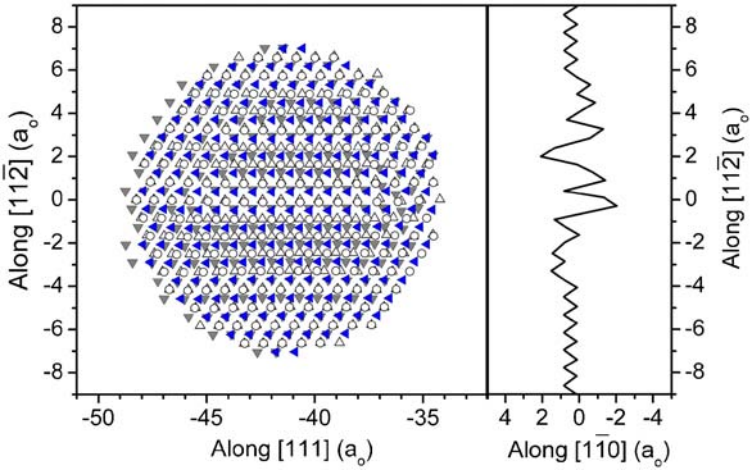

Fig. 24. Position of Cu atoms in four consecutive (1 $\bar{1}$ 0) planes through the centre of a 4 nm precipitate in Fe after dislocation breakaway at 0 K. The figure on the right shows the dislocation line in [1 1 1] projection after breakaway: climb to the left indicates absorption of vacancies whereas climb to the right is due to absorption of atoms. (From Ref. [117].)

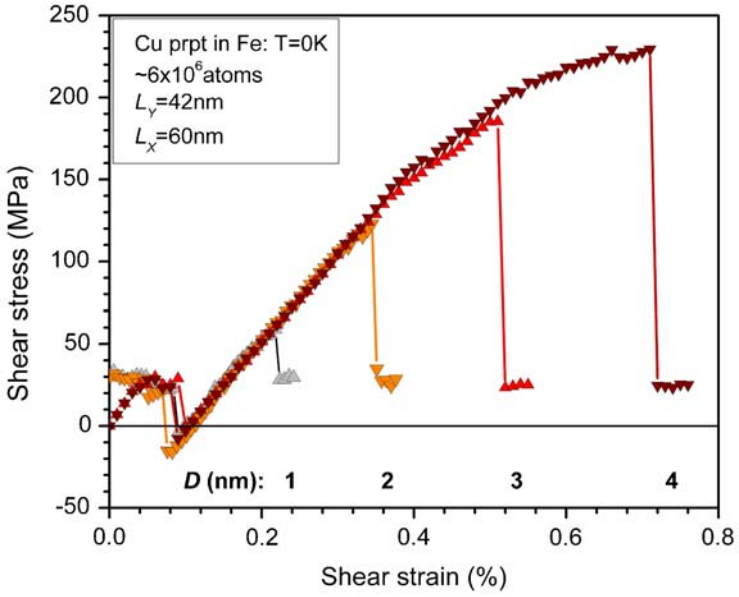

Fig. 25. Stress–strain curves obtained for interaction between an edge dislocation and Cu precipitates with diameter D and spacing $L = 42$ nm in Fe at 0 K. The model size and D are indicated.

and modulus-difference approximations that form the basis of the Russell–Brown model of Cu precipitate strengthening of Fe [132].

4.2.3. Comparison of atomistic and continuum results at 0 K

The simulations of the preceding section neglect kinetic effects and are the atomic-level equivalent of conventional linear elasticity modelling of dislocations. In the latter, the simplest approach to strengthening due to a dispersion of localised obstacles uses the line tension approximation. For a row of obstacles of spacing L, the dislocation breaks away when the forward force τbL on length L overcomes the resistance of one obstacle, i.e. when the obstacle can no longer withstand the line tension force $2\Gamma\cos(\varphi/2)$ imposed by the two segments of the bowing line at the obstacle: here Γ is the line tension (equal to approximately $Gb^2/2$ in the constant line tension approximation) and φ is the included angle between the segments, as shown for a 3 nm precipitate in Fig. 21. The critical stress is reached when φ is reduced to the critical angle φ_c and so

$$\tau_c = \alpha \frac{Gb}{L}, \tag{13}$$

where $\alpha = \cos(\varphi_c/2)$. A factor of approximately 0.8 has to be introduced to account for randomness in the obstacle arrangement [90,91]. It was seen in the data for voids above that the dependence of τ_c on L^{-1} holds for atomic-scale interactions, as it should since there is no reason to doubt the Peach–Koehler expression that the

force per unit length on a dislocation is τb. The parameter α that characterises obstacle strength does not have a firm theoretical basis, however. In the literature where experimental tensile test data for, say, irradiated steels have been used to validate a theoretical expression for yield stress, eq. (13) has frequently been employed with α obtained by empirical fitting to the test data. It generally falls in the range 0.1–0.5. Unfortunately, this approach is inadequate for quantitative and predictive modelling because, as seen in preceding sections, α depends sensitively on obstacle size, type and atomic mechanisms. For example, the 3 nm precipitate in Fig. 21 has $\varphi_c = 70^\circ$ and $\tau_c = 145$ MPa, yet τ_c given by eq. (13) with this angle and $L = 62$ nm is approximately 210 MPa. Similarly, τ_c for the 2 nm void with this L is 161 MPa, but eq. (13) with $\varphi_c = 0^\circ$ predicts 260 MPa. The line tension model overestimates obstacle strength because it neglects self-interaction between the branches of the dislocation across the obstacle, which tends to pull them into alignment.

Self-stress interaction between different parts of a dislocation was first included in modelling of strengthening due to impenetrable obstacles (Orowan strengthening) and voids using linear elasticity in Refs [115,133]. By computing the equilibrium shape of a dislocation bowing between obstacles under increasing stress, it was shown that the maximum stress for which equilibrium could be achieved fitted the relationship

$$\tau_c = \frac{Gb}{2\pi AL}\left[\ln(D^{-1} + L^{-1}) + \Delta\right], \tag{14}$$

where G is the elastic shear modulus and Δ is an empirical constant; A equals 1 if the initial dislocation is pure edge and $(1 - \nu)$ if pure screw, where ν is Poisson's ratio. It was shown in Refs [115,134] that eq. (14) holds for anisotropic elasticity if G and ν are chosen appropriately for the slip system in question, i.e. if $Gb^2/4\pi$ and $Gb^2/4\pi A$ are set equal to the pre-logarithmic energy factor of the screw and edge dislocations, respectively. The value of G obtained in this way is 64 GPa for $\langle 1\,1\,1\rangle\{1\,1\,0\}$ slip in Fe and 43 GPa for $\langle 1\,1\,0\rangle\{1\,1\,1\}$ slip in Cu [135]. The explanation for the D- and L-dependence of τ_c is that voids and impenetrable Orowan particles are 'strong' obstacles to dislocation motion and so the dislocation segments at the obstacle surface are pulled into parallel, dipole alignment at τ_c by self-interaction [115,133]. For every obstacle, the forward force, $\tau_c bL$, on the dislocation has to match the dipole tension, i.e. energy per unit length, which is proportional to $\ln(D)$ when $D \ll L$ and $\ln(L)$ when $L \ll D$ [2]. Thus, $\tau_c bL$ correlates with $Gb^2\ln(D^{-1} + L^{-1})^{-1}$. The correlation between τ_c obtained in atomic-scale simulation and the harmonic mean of D and L, as in eq. (14), is tested for voids and precipitates in Fig. 26.

Values of τ_c obtained in the continuum modelling of Refs [115,133,134] were found to fit eq. (14) with Δ equal to 0.77 for the Orowan process and, with a realistic estimate of void surface energy, 1.52 for voids. Lines for these two values of Δ are drawn on Fig. 26. It is seen that the void data for Fe fit eq. (14) for D down to about $5b$, i.e. just over 1 nm. τ_c for voids in Cu fall below the prediction of eq. (14) when D is small and above it when large, a transition that seems to be related to whether τ_c is controlled by release from the void of a single partial or both, as explained in

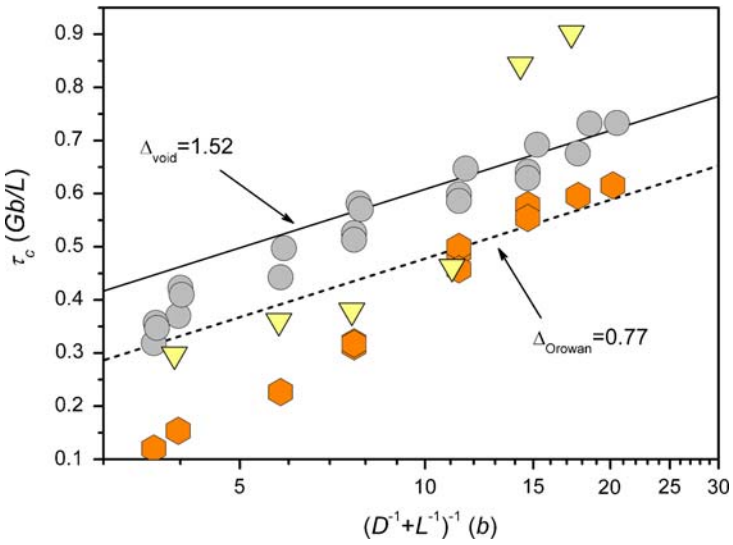

Fig. 26. Critical stressτ_c (units Gb/L) versus the harmonic mean of D and L (unit b) for voids in Fe (circles) and Cu (triangles) and Cu precipitates in Fe (hexagons) for crystals at 0 K with various sizes (L: 41.4–83 nm; L_x: 20–60 nm; number of atoms: 2–8 $\times$ 10^6). Lines obtained in Refs [115,133,134] as best fit to τ_c values obtained in continuum modelling for voids and impenetrable Orowan particles are also shown. (From Refs [116,118,120,127].)

Section 4.2.2. The data for Cu precipitates in Fe follows the continuum prediction for large D but falls well below it for small precipitates that are easily sheared.

It is perhaps surprising at first sight to find that the atomic modelling data and the continuum results are in good agreement across the size range down to about $D<2$ nm for voids in Fe and 3–4 nm for the other obstacles. The explanation lies in the fact that in the atomic simulation, as in the earlier continuum modelling, large obstacles offer sufficient resistance to dislocation glide at $T=0$ K to enable the dislocation line segments at the obstacle surface to adopt dipole alignment at τ_c. This shape would not be achieved at this stress in the line-tension approximation where self-stress effects are ignored. This work shows that eq. (14) can be used in continuum modelling for nanoscale obstacles that are sufficiently strong. The measure of strength and identification of the atomic mechanisms involved require atomic modelling, however.

The incorporation of MS data into large-scale DD simulations requires further study. As a start, Monnet [136] has shown how the results for τ and ΔE from atomic simulation in Fig. 17(a) can be interpreted and analysed using linear elasticity. The method decomposes the work done by the applied stress, i.e. $V\int \tau \mathrm{d}\varepsilon$ where V is the model volume, into three components. One is the linear elastic strain energy in the model due to the stress, i.e. $(V/2G)\int \tau \mathrm{d}\tau$. Another is the work dissipated as the dislocation overcomes lattice friction. This is extracted from the system in the MS technique, i.e. energy minimisation prevents an increase in E as a dislocation moves

at the Peierls stress, even though work is done. The third component is the work required for the dislocation to bow whilst pinned by the voids: the energy of the additional line length can be treated in the line-tension approximation. Monnet shows that it is possible to determine the dislocation–void interaction energy by subtracting the elastic and curvature components from ΔE. Shearing of the void by the dislocation leads to an increase of E equal to the formation energy of the steps created on the void surface and dislocation climb by absorption of vacancies does not seem to play an important role because the energy contribution is insignificant.

4.3. Temperature effects for voids and precipitates

Numerous simulations by MD show that, in general, τ_c decreases and the dislocation line bows out less in the critical condition with increasing T (see Fig. 27). Mechanisms for some obstacles are similar to those at 0 K. For example, dislocation climb does not occur when an edge dislocation is released from a void in Cu at $T>0$ K and voids in Fe shrink due to climb at all temperatures [122]. The latter phenomenon was found using the interatomic potential for Fe from Ref. [69] and has now been observed in simulations [137,138] using more recent potentials [69,139]. There is, however, a considerable difference in the T-dependence of τ_c for

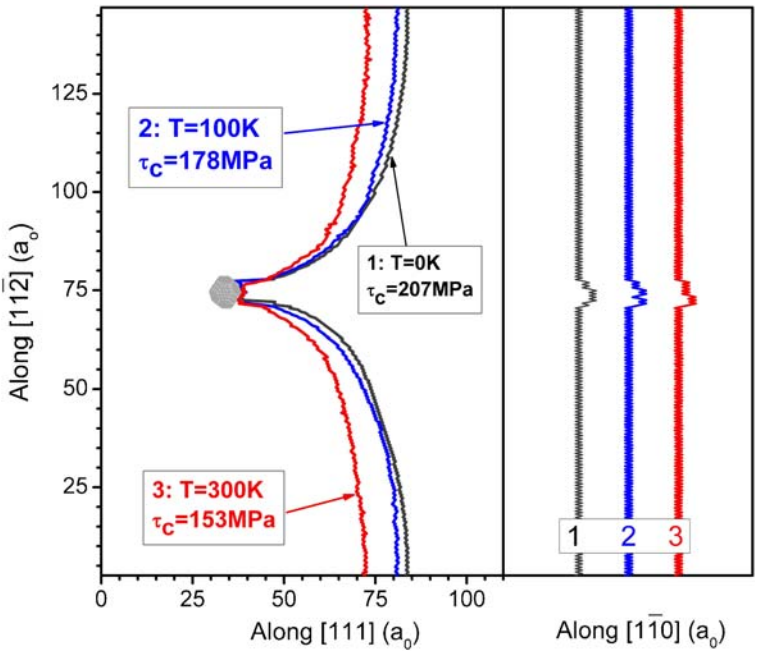

Fig. 27. Critical line shape for a dislocation passing a row of 2 nm voids with spacing 41 nm in Fe at 0, 100 and 300 K. (From Ref. [120])

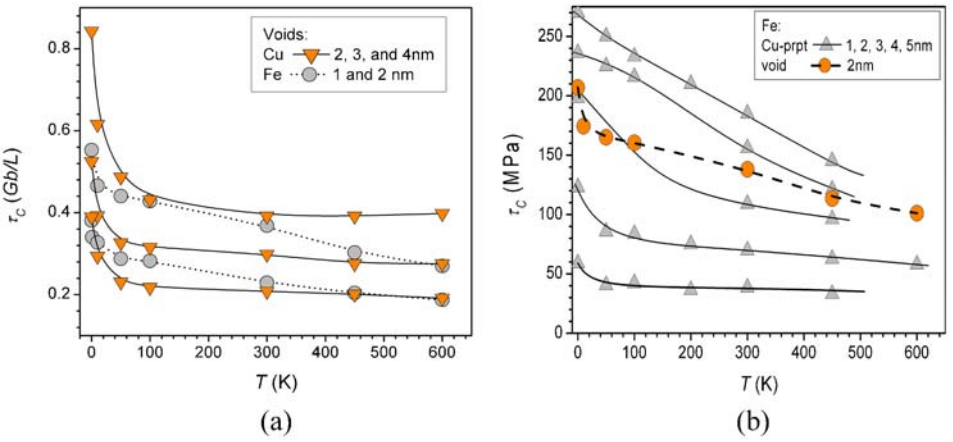

Fig. 28. Plot of τ_c versus T with $\dot{\varepsilon} = 5 \times 10^6\ s^{-1}$ for (a) voids of different size in Fe ($L = 41.4$ nm) and Cu ($L = 35.4$ nm), and (b) Cu precipitates of different size (triangles) and a 2 nm void (circles) in Fe ($L = 41.4$ nm). (From Refs [116–120].)

voids in Fe and Cu. As shown in Fig. 28(a), τ_c for iron has a rather gradual decrease over the range from 0 to 600 K whereas it exhibits a significant drop in Cu between 0 and 100 K and only a very weak decrease beyond that. (We will return to this feature of Cu in Section 5.5 on SFTs.) The same conclusions were drawn by Hatano and Matsui [140], who used a similar, but smaller MD model of Cu with an edge dislocation and voids in the size range $D = 0.6$–5 nm with $L = 23$ nm. They found no significant variation of τ_c for T in the range 100–500 K, a result attributed to the absence of dislocation climb at breakaway. The data for breakaway stress of the leading and trailing partials at 300 K were analysed separately in Ref. [140] and the effects of dissociation were found to be the same as those at $T = 0$ K discussed in Section 4.2.1.

Hatano et al. [141] have reported several distinctive features for the interaction of a screw dislocation with voids with $D = 1$–6 nm in Cu using an MD model with 920,000 atoms and $L = 20$ nm. For low T equal to either 10 or 150 K, the τ–ε plot exhibits only one maximum as the two Shockley partials unpin from a void together, unlike those for the edge dislocation (see Fig. 23), for which the partials have larger spacing. The dependence of τ_c on D is as in eq. (14) but with $A = (1 - \upsilon)$, which is predicted from continuum modelling [133] because segments of the initially straight screw dislocation are pulled towards the *edge* dipole configuration, for which the energy per unit is proportional to $(1 - \upsilon)^{-1}$. However, the D-dependence of τ_c changes between 150 and 300 K, and the τ_c values are higher than expected from the low-T results. This is due to constriction and cross-slip of the dissociated dislocation at the void surface. Cross-slip does not occur at lower T, presumably because the thermal energy is insufficient to activate cross-slip at the high strain rate of the simulations. Cross-slip can result in more than one outcome and at 450 K a mechanism which involves double cross-slip and a

formation of prismatic loop can be activated. This leads to the unusual effect of increased τ_c at high T. However, caution has to be exercised when simulating a screw dislocation because interactions between the obstacle and its images can occur through the periodic boundaries (Section 2.5). They can affect the breakaway process, particularly when T is high and L is as small as 20 nm. It will be shown in Section 5.5.2 that the behaviour of a screw dislocation between free surfaces in an FCC metal has specific features.

The effects of temperature on dislocation interaction with Cu precipitates in Fe are more complex, for the stability of BCC Cu within a precipitate is dependent on T and D. The free energy difference between the FCC and BCC phases increases with decreasing T but the surrounding Fe matrix tends to stabilise the BCC phase, and so there is an interplay between precipitate size and temperature in the dislocation-induced transformation process. The variation of τ_c with T for $D = 1$–5 nm is shown for the edge dislocation in Fig. 28(b). Data for a 2 nm void are included for comparison. τ_c is small for small precipitates. Their structure remains coherent with the Fe matrix across the temperature range and τ_c has a weak dependence on T above 100 K. The critical size for the BCC→FCC-like transformation increases with increasing T. Thus, for large precipitates the T-dependence of τ_c is strong in comparison with voids, to the extent that when T increases to 450 K, a 4 nm precipitate offers only about the same obstacle strength as a 2 nm void. The dislocation induces the structure change at low T but this is suppressed above 450 K and the cutting process is simple shear, as in the small precipitates. This is inferred from the climb profiles for $D = 4$ nm in Fig. 29: the

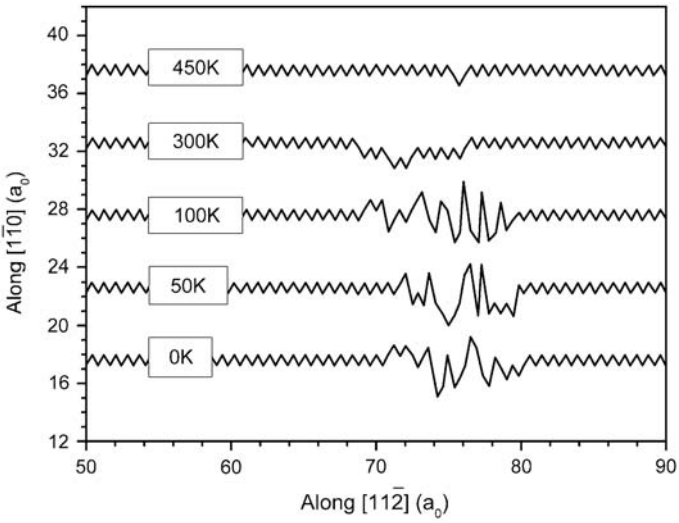

Fig. 29. [1 1 1] projection of an edge dislocation with $\boldsymbol{b} = \frac{1}{2}[1\,1\,1]$ after breakaway from a 4 nm Cu precipitate in Fe at different temperatures. Climb down is due to absorption of atoms by the dislocation and creation of vacancies inside the precipitate, whereas deviation up is due to the opposite process.

phase transformation is accompanied by the creation of vacancies and extra atoms in the precipitate, resulting in dislocation climb seen for $T < 450\,\mathrm{K}$.

The size dependence of the Cu transformation mechanism has now been confirmed for screw dislocations by MD simulation of screw–precipitate interaction at 10 K under constant τ [142]. It was observed that the phase transformation occurred for $D > 1.8\,\mathrm{nm}$ and that when D exceeds 2.5 nm the dislocation bypass mechanism becomes Orowan looping due to the coherency loss of the precipitates. Values of τ_c were not obtained.

The simulations suggest that the yield stress of an under-aged or neutron-irradiated Fe–Cu alloy containing small, coherent precipitates should have a weak T-dependence, whereas the dependence should be stronger in an overaged or electron-irradiated alloy where the population of coherent precipitates has larger size [127]. More direct experimental evidence in support of the simulation predictions has been obtained by Lozano-Perez et al. [143] by utilising the crystallography of the BCC→9R martensitic transformation. Planes of atoms in twinned 9R precipitates exhibit characteristic 'herring-bone' fringe contrast when viewed along a $\langle 1\,1\,1 \rangle$ direction of the Fe matrix in a high-resolution electron microscope (HREM). The angle, α, between fringes in neighbouring twin bands is approximately 129° immediately after the transformation, but relaxes during annealing to 121° to reduce the strain energy [123]. Samples of a Fe-1.3 wt%Cu alloy were aged at 550 °C before cooling to room temperature, in order that precipitates larger than about 5 nm would transform to 9R whilst smaller precipitates would retain the BCC structure. One set of samples was deformed by bending at room temperature and both sets were then annealed at 400 °C to allow transformed precipitates to relax. HREM foils were prepared at −60 °C so that any remaining untransformed precipitates should transform to 9R. Angle α was then measured for precipitates in both sets of samples. The results are shown in Fig. 30, from which it is seen that precipitates in the undeformed alloy have a relaxation threshold of about 4–5 nm, while all the precipitates in the deformed samples appear to be relaxed.

High-chromium (Cr) ferritic/martensitic steels offer another alloy system where coherent precipitates harden the material during ageing and/or irradiation. Cr-rich α' phase separates from the α phase and forms a fine dispersion of nanoscale obstacles to dislocation motion, e.g. Refs [144–146]. Unlike Cu in Fe, Cr is stable in the BCC structure, but it has a larger elastic modulus than Fe and α' precipitates are expected to repel dislocations, rather than attract them. Terentyev et al. [147] have simulated the interaction of an edge dislocation with a row of spherical Cr precipitates in a matrix of either pure Fe or Fe–10at.% Cr, the latter being used to compare the obstacle contributions of precipitates and a solid solution. The MS method ($T = 0\,\mathrm{K}$) with the model in Ref. [42] described in Section 2.3 was used with the potential from Ref. [148]. The precipitate spacing was 14 nm for small precipitates ($D = 0.6$ or 1.2 nm) and 28 nm for larger ones.

Examples of the critical line shape and corresponding stress–strain curves obtained for several values of D are shown in Fig. 31. (The stress in the plot is the applied stress minus 80 MPa, which is the Peierls stress at 0 K for the edge

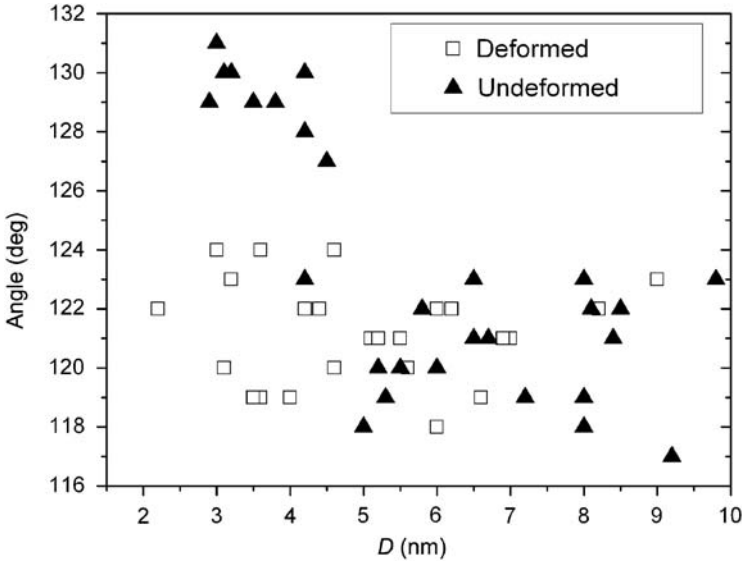

Fig. 30. Angle α between herring-bone fringes in adjacent twin-related bands in Cu precipitates in Fe, plotted against D for deformed and undeformed samples. (Reprinted from Ref. [143] with permission from Taylor & Francis Ltd., http://www.informaworld.com.)

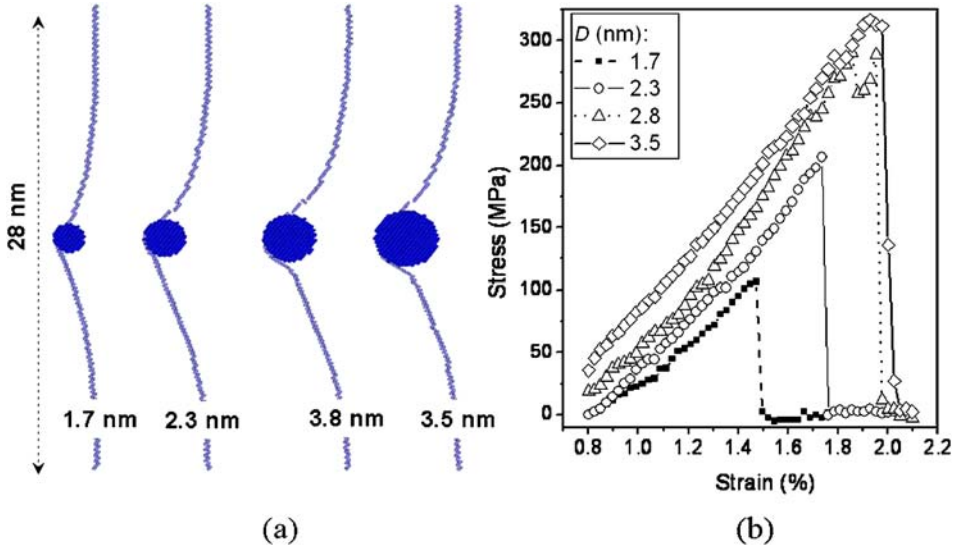

Fig. 31. Interaction of an edge dislocation with an α' Cr precipitate in Fe. (a) Configuration of the dislocation in the $(1\ \bar{1}\ 0)$ slip plane at τ_c for precipitates of different size D, and (b) the corresponding τ versus ε plots. (Reprinted from Ref. [147] with permission from Elsevier Ltd. http://www.sciencedirect.com/science/.)

dislocation in pure Fe with the potential used (Fig. 8(a)). It is seen that the dislocation is repelled by a precipitate but finally shears it at τ_c. No defects are formed inside a precipitate and the dislocation does not acquire jogs as a result of the shearing process. The stress reaches the critical value just as the dislocation enters the precipitate in both the pure Fe and Fe-10% Cr matrices (see, e.g. Fig. 3 in Ref. [147]). τ_c is plotted in Fig. 32(a) in the form predicted by continuum modelling of impenetrable particles with dislocation self-stress included (eq. (14)). The atomistic and continuum values are in good agreement at large D, for which the dislocation sidearms at the obstacle are pulled into near-screw alignment at τ_c, but not when D is small, i.e. when $\varphi_c \gg 0^\circ$ (compare Fig. 31 and Fig. 21). Fig. 32(a) also contains estimates of τ_c derived from two theoretical treatments for shearable particles using the approximation of constant line tension (equal to $Gb^2/2$). For the chemical strengthening (CS) mechanism, Terentyev et al. used MS to calculate the additional (compared with pure Fe) applied force required for the dislocation to shear a Cr precipitate by ½[1 1 1] on the (1 $\bar{1}$ 0) plane. The other estimate uses the shear modulus difference (SMD) between Fe and Cr, for which a formula from Ref. [149] was used since the Russell–Brown analysis applies to alloys in which the precipitate modulus is less than that of the matrix. Both treatments underestimate τ_c except when D is small. When the two contributions are added, however, the total τ_c they predict is much closer to the simulation data. Fig. 32(b) compares the dependence of τ_c on the harmonic mean of L and D for matrices of pure Fe and the Fe-10%Cr solid solution. τ_c is much higher in the latter case. The difference, labelled $\Delta\tau_{FeCr}$, is almost constant and independent of D. It is approximately 250 MPa and equals the stress required for continued edge dislocation glide in the Fe-10%Cr solution without precipitates. In other words, the two contributions

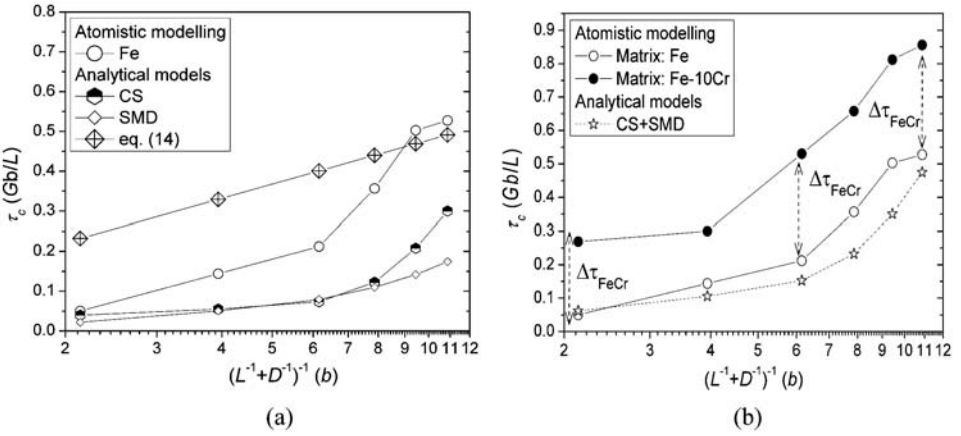

Fig. 32. Plot of τ_c (units Gb/L) versus Cr precipitate diameter at $T = 0$ K. (a) Comparison of values obtained by simulation with theoretical estimates based on either eq. (14) or models of chemical strengthening (CS) and shear modulus difference (SMD). (b) The effect on τ_c of Cr in solution in the Fe matrix. (Reprinted from Ref. [147] with permission from Elsevier Ltd. http://www.sciencedirect.com/science/.)

of solution and precipitate strengthening combine by linear addition in this system. (This is consistent with conclusions on the superposition rule by some workers, but not others. For a recent discussion see Ref. [150].)

In contrast to the shearable obstacles above, precipitates in some materials are not coherent with the surrounding matrix, e.g. in overaged or dispersion-strengthened alloys. In these, a dislocation either stays in its slip plane by bowing between the obstacle and leaving a loop around it ('Orowan' mechanism), or screw segments cross-slip to allow bypass on a different slip plane ('Hirsch' mechanism). (See, e.g. Refs [2,89,151].) The interaction between an edge dislocation and a rigid, impenetrable particle has been simulated by Hatano [152]. The particle was created in a Cu crystal by defining a spherical region in which the atoms were immobile. The MD model used the interatomic potential from Ref. [121] and was strained at a constant rate of $7 \times 10^6\,\mathrm{s}^{-1}$ at $T = 300\,\mathrm{K}$.

With reference to Fig. 3, the outcome was found to depend on whether strain was applied by moving either upper block B alone or A and B by equal but opposite amounts. The Hirsch mechanism was found to operate in the former method. In the sequence shown in Fig. 33: (a) the dislocation bows round the obstacle to form a screw dipole; (b) the screw segments cross-slip onto inclined $(1\,1\,\bar{1})$ planes at τ_c; (c), (d) they annihilate by double cross-slip, allowing the dislocation, now with a double superjog, to bypass the obstacle; (e) a prismatic loop with the same $\boldsymbol{b}$ is left behind; and (f) the dragged superjogs pinch-off as the dislocation glides away, creating a loop of opposite sign to the first on the right of the obstacle. τ_c varies with D and L as predicted by the continuum modelling that led to eq. (14), but is over three times larger in magnitude. Hatano argues that this could arise from either higher stiffness of a dissociated dislocation or a dependence of τ_c on the initial position of the dislocation. It is also possible that the requirement for the dislocation to constrict

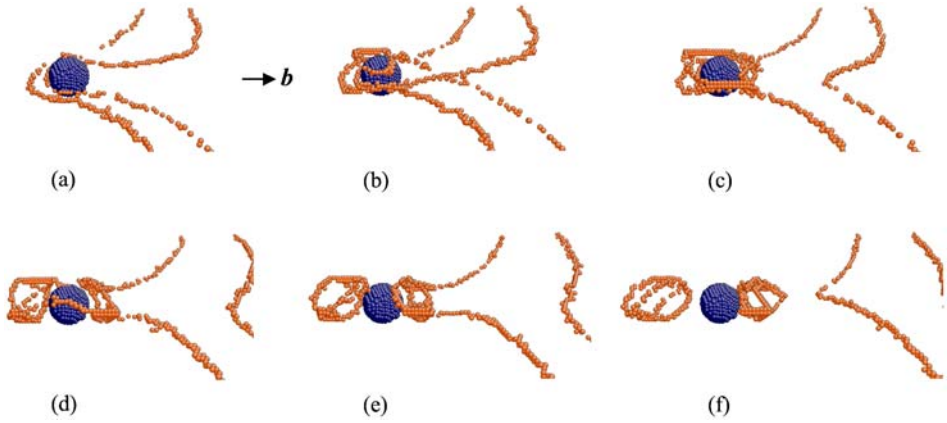

Fig. 33. Visualisations of an edge dislocation bypassing an impenetrable particle of 3 nm diameter in Cu at 300 K. Atoms in the dislocation cores are shown, but those in the stacking faults between the partial dislocations are not visualised. See text for details. (Reprinted with permission from Ref. [152]. © (2006) by the American Physical Society.)

and the absence of a component of applied shear stress on the cross-slip plane results in a high value of τ_c. When the model was loaded by displacing both blocks A and B, only Orowan looping occurred, although τ_c was almost the same. Hatano speculates that the presence of stress asymmetry in the vicinity of the obstacle as the strain pulse travels from the top of the model promotes cross-slip and the Hirsch mechanism. The modelling issues raised by this work require further study.

4.4. Bubbles and loose clusters of vacancies

Despite the potential importance of He bubbles, i.e. He-filled cavities, for the mechanical properties of structural materials in fusion energy applications, there have been few atomic-level studies of dislocation–bubble interaction. This is explained in part by difficulties in developing suitable interatomic potentials for metal–He systems, for those in use have deficiencies in describing He-defect properties. Nevertheless, some MD simulations have been performed [137,153,154]. A small model of Fe containing about 0.5×10^6 atoms was used to study interaction between an edge dislocation and a row of 2 nm cavities containing He. He:vacancy ratios of up to 5 were simulated for T between 10 and 700 K. It was found that τ_c has a non-monotonic dependence on the He:vacancy ratio, dislocation climb increases with this ratio and interstitial defects are formed in the vicinity of the bubble. However, the equilibrium properties of He-filled bubbles were not investigated and interpretation of these results is not straightforward.

Vacancies do not always agglomerate in compact arrangements such as voids or dislocation loops. Positron annihilation experiments on neutron-irradiated Fe indicate that vacancies cluster together in loose arrangements in the core of displacement cascades [154] and this is supported by MD modelling [12,155,156]. Interaction between dislocations and vacancies in diffuse clusters is therefore relevant to the vacancy contribution to matrix hardening in irradiated Fe. The effect on τ_c and dislocation climb of changing the arrangement of 59 vacancies from a void with $D = 1$ nm to a loose cluster has been investigated for the case $L = 41.4$ nm by Osetsky and Bacon [120] using the interatomic potential for Fe from Ref. [70]. Clusters were created in spherical zones centred on the slip plane with vacancy concentration, c_v, equal to 10, 15, 25 or 100%. The vacancies were placed randomly on lattice sites and three different arrangements were simulated for the 15% condition. The crystals were annealed at 600 K for 1 ns before shear strain was applied at a constant rate of either 2 or $5 \times 10^6\,s^{-1}$ at temperatures in the range from 1 to 600 K.

τ_c versus T is plotted for all the c_v values in Fig. 34(a). Although τ_c for a loose cluster is smaller than that for a void with the same number of vacancies, the difference is small for the higher c_v values. For instance, the T-dependence of the plot for $c_v = 25\%$ follows that for the void with only a slight reduction in stress (15–20 MPa). The τ_c values for the three clusters with $c_v = 15\%$ show variability associated with the differences in the vacancy migration during interaction, but the trend in the mean value of τ_c again follows that for the void. The stress values for the 10% cluster are the lowest, although the unexpectedly high value for 450 K again

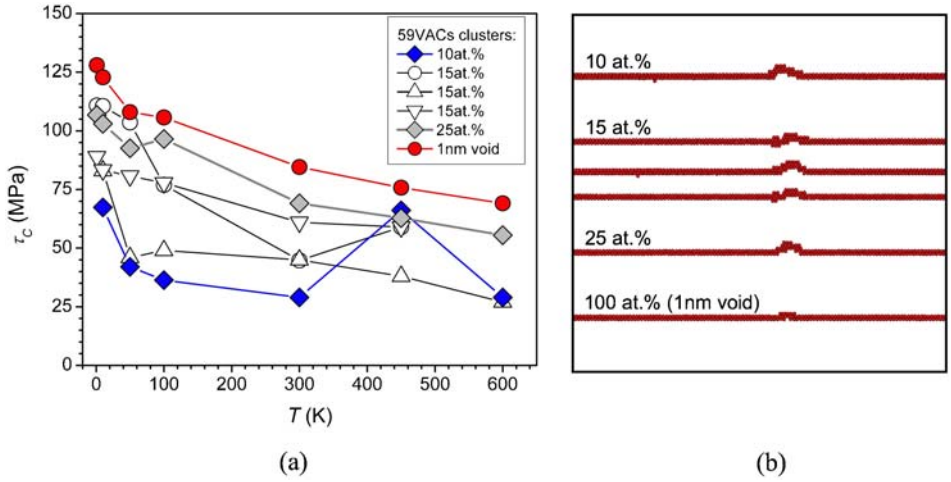

Fig. 34. (a) Plots of τ_c versus T for an edge dislocation breaking away from a row of vacancy clusters in Fe. All clusters contain 59 vacancies at concentrations from 10 to 100%. (b) [1 1 1] projection of the shape of a ½[1 1 1] edge dislocation after breakaway at 300 K from the vacancy zones with c_v values indicated. The extra half-plane is in the upper part of the figure in each case. (From Ref. [120].)

shows the significance of the vacancy rearrangement. We conclude that although loose clusters of vacancies are weaker obstacles than voids, they still offer significant resistance to slip and may make an important contribution to matrix hardening in the temperature range where they are stable. The vacancy absorption by climb of the edge dislocation seen on breakaway from a void (Section 4.3) also occurs for clusters. The visualisations of the core atoms in Fig. 34(b) show the shape of the ½[1 1 1] edge dislocation along the bottom of its extra half-plane after passing through a cluster at 300 K. It is clear from the extent of climb that vacancy absorption is a more efficient process for zones where the vacancies are loosely packed.

4.5. Conclusions

It is clear from the simulation studies of dislocation interaction with obstacles such as voids and precipitates reviewed in this section that a treatment based on linear elasticity can provide a good approximation of processes and strengthening effects that occur in some cases. In these, the elasticity approximation has been shown to be valid, even for obstacles only a nanometre or so in size. A key requirement for validity is that dislocation self-stress must be allowed for in the elasticity approach because interaction of nearby segments of the same dislocation can determine how an obstacle is overcome. Self-stress is incorporated in modern DD codes, see e.g. Ref. [1]. The agreement between continuum and atomistic modelling is obviously best for $T = 0$ K, i.e. when minimum potential energy defines the equilibrium configuration. The results of the two methods are also closer for the BCC structure, in which the dislocation is not dissociated, than in, say, Cu, where it is. This suggests

that the dissociated nature of the dislocation core should be taken into account in DD modelling of many FCC metals.

MS and MD simulations have revealed effects that were not foreseen in earlier continuum treatments. One is climb of an undissociated dislocation by absorption or emission of point defects as it leaves an obstacle. From simulations to date, this seems to be a general phenomenon for voids and clusters of vacancies. Another effect is strengthening due to a dislocation-induced phase transformation of a metastable precipitate. The predictions that have arisen from atomic-level simulation are now found to be consistent with accurate experimental measurements on nanoscale Cu precipitates in Fe. This points to the power of simulations provided the interatomic potentials employed are sufficiently reliable.

5. *Obstacles having dislocation character*

5.1. Dislocation loops and SFTs

Although loops and SFTs can be created as a result of dislocation reactions, this chapter is concerned with those that form in irradiated or quenched metals, i.e. those that nucleate and possibly grow in a supersaturation of point defects. SFTs have a vacancy nature, whereas dislocation loops can form from vacancies or SIAs. The shape, Burgers vector and nature of these extended defects have been widely studied over the past 50 years, particularly by transmission electron microscopy (TEM), and are reasonably well understood (e.g. Refs [2,3]). We denote the Burgers vector of a dislocation loop by $\boldsymbol{b}_{\mathrm{L}}$. Perfect loops have $\boldsymbol{b}_{\mathrm{L}}$ equal to a lattice translation vector, e.g. $\frac{1}{2}\langle 1\,1\,0\rangle$ in the FCC structure and $\frac{1}{2}\langle 1\,1\,1\rangle$ or $\langle 1\,0\,0\rangle$ in the BCC structure. If the metal has a stable stacking fault of low enough energy on the plane in which the loop forms, the loop may enclose a fault and have a partial Burgers vector. Stable faults are not known to exist in the BCC metals where all loops are perfect. In FCC metals with low fault energy on $\{1\,1\,1\}$ planes, faulted ('Frank') loops with $\boldsymbol{b}_{\mathrm{L}} = 1/3\langle 1\,1\,1\rangle$ are common. The relative stability of faulted and perfect loops depends on fault energy and loop size, with the result that Frank loops can unfault to become perfect loops when large enough. This process depends on the loop nature. Vacancy loops contain an intrinsic fault corresponding to a missing plane in the ternary stacking of $\{1\,1\,1\}$ planes. It can be removed by a single Shockley partial sweeping across the loop, e.g. on the $(1\,1\,1)$ plane:

$$\frac{1}{3}[1\ 1\ 1] + \frac{1}{6}[1\ 1\ \bar{2}] \rightarrow \frac{1}{2}[1\ 1\ 0]. \tag{15}$$

Frank loops formed by SIAs contain an extrinsic fault, i.e. an extra plane in the $\{1\,1\,1\}$ stacking sequence, and this is removed when two Shockley partials sweep the planes adjacent to the fault, e.g.

$$\frac{1}{3}[1\ 1\ 1] + \frac{1}{6}[2\ \bar{1}\ \bar{1}] + \frac{1}{6}[\bar{1}\ 2\ \bar{1}] \rightarrow \frac{1}{2}[1\ 1\ 0]. \tag{16}$$

The partials may glide either together as a double core (a 'D-Shockley' partial) or separately. It will be seen in Section 5.3.2 that these unfaulting reactions can be caused by interaction with dislocations. Frank loops with lowest energy have hexagonal shape with side orientations that depend on the material, e.g. ⟨1 1 0⟩ directions in Cu [157] and ⟨1 1 2⟩ directions in austenitic steels and Ni [158,159]. The lowest energy shape of perfect ½⟨1 1 0⟩ loops is a rhombus, with loop sides lying on the glide prism formed by the two sets of {1 1 1} planes that contain $\boldsymbol{b}_L$ [13].

In metals such as Ag, Au and Cu with relatively low stacking fault energy, vacancy Frank loops may not unfault but dissociate into an SFT with its six sides consisting of stair-rod partial dislocations. The vacancy content of the loop is thereby redistributed over the four faulted {1 1 1} faces of the tetrahedron [160,161]. SFTs formed in this way are commonly observed after quenching and ageing [162–164]. Nanometre-scale SFTs can also be created directly in displacement cascades in irradiated FCC metals, see, e.g. experimental observations [165] and MD simulations [166] on Cu. Large SFTs are also formed during fast deformation in Al, a material with a high fault energy [167].

The most commonly observed loops in irradiated BCC metals are interstitial in nature and have $\boldsymbol{b}_L = ½⟨1 1 1⟩$ (e.g. Ref. [19]), which is consistent with the fact that dislocation energy is proportional to b^2 and ½⟨1 1 1⟩ is the shortest lattice vector. These loops are also the most common type created in MD modelling of displacement cascades [12]. MS simulations indicate that the most stable loop shape is a hexagon with sides along ⟨1 1 2⟩ directions. Experiments on neutron-irradiated Fe and ferritic alloys show that interstitial loops with $\boldsymbol{b}_L = ⟨1 0 0⟩$ also form in these materials. Their fraction of the loop population increases with irradiation temperature [21,168,169]. They also form in electron- and ion-irradiated Fe [170,171]: their sides lie in ⟨1 0 0⟩ directions. ⟨1 0 0⟩ loops do not have the shortest $\boldsymbol{b}_L$ and various explanations for their occurrence have been proposed. However, recent calculations based on anisotropic elasticity theory have shown that changes in the elastic constants of Fe as T is increased towards the α–γ transformation reverse the order of stability of ½⟨1 1 1⟩ and ⟨1 0 0⟩ loops, so that the latter are favoured at high T [172]. Thus, in order to account for the whole temperature range of interest, both types of loops are considered here.

Perfect dislocation loops are glissile along their glide prism, in principle. Small loops containing up to ~100 SIAs have the structure and properties of bundles of crowdions with their axis parallel to $\boldsymbol{b}_L$. Consequently they exhibit rapid thermally activated 1D motion. At high enough temperature, $\boldsymbol{b}_L$ can flip from one direction to another by thermal activation, leading to 3D diffusion composed of 1D motion separated by changes of direction [173–175].

The critical stress and atomic processes involved in the interaction of gliding dislocations with loops and SFTs have been simulated using the PAD model (Section 2.3) and the results, including effects of obstacle size, dislocation–obstacle geometry, T and $\dot{\varepsilon}$ are presented in Sections 5.3–5.5. The geometry for loops in BCC metals (Section 5.3) is the same as that in Fig. 16(a) for obstacles in the form of voids and precipitates. The simulation cell used for the FCC metals is shown schematically in Fig. 16(b). In both cases, the 'positive' edge dislocation has its extra

half-plane above the slip plane in the figure and the positive direction of the right-handed screw dislocation is the x direction. The Thompson tetrahedron [2,3] drawn in Fig. 16(b) will be used to label the Burgers vectors and slip and habit planes of the FCC simulations. The perfect dislocation has $\boldsymbol{b} = \mathbf{AC}$ with an initial line orientation that depends on its character. Upon initial relaxation, the dislocation dissociates on plane ABC into partials with Burgers vectors $\mathbf{A\delta}$ and $\mathbf{\delta C}$.

The variety of reactions observed in simulations to date is too large to be described comprehensively in this review. However, it is possible to classify them in a qualitative way according to some common characteristics. Four main types of interaction have been identified, depending on the character of the dislocation and on whether the obstacle is unchanged, modified or absorbed by the dislocation. In addition, some reactions occur which are specific to the type of defect, i.e. SFT or loop. These reaction categories are summarised in Section 5.2 and examples for loops and SFTs are presented in Sections 5.3–5.5.

5.2. Classification of main reactions

5.2.1. Reaction R1: the obstacle is crossed by the dislocation and both are unchanged
In this, the defect is sheared by the dislocation but is fully reconstructed after the dislocation unpins. This reaction has been observed for both screw and edge dislocations with SFTs (see Fig. 51 below) and Frank loops (see Fig. 36 below) in FCC metals. It has also been observed for edge dislocations interacting with large $\frac{1}{2}\langle 1\,1\,1\rangle$ loops that have $\boldsymbol{b}_{\mathrm{L}}$ inclined to the glide plane in BCC metals (see Fig. 44 below). Steps corresponding to $\boldsymbol{b}$ form on the defect surface (1 step on loops, 2 ledges on SFTs) but are mobile and disappear at a border of the defect. The obstacle and the dislocation thus remain unchanged and τ_{c} is low. The requirements are that the dislocation slip plane should be close to an SFT apex or loop edge, T should be low and v_{D}, i.e. $\dot{\varepsilon}$, high.

5.2.2. Reaction R2: the obstacle is crossed and modified and the dislocation is unchanged
This occurs in two instances. First, as a modification of reaction R1 in FCC metals when the steps are stable because of a relatively long distance to either the SFT apex or the loop edge. Multiple reaction with dislocations on the slip plane shears the obstacle into separate parts (see Fig. 52 below for SFTs). Second, some $\langle 1\,0\,0\rangle$ loops in BCC metals are transformed by an edge dislocation into mixed $\langle 1\,0\,0\rangle/\langle 1\,1\,1\rangle$ loops (see Fig. 48 below).

5.2.3. Reaction R3: partial or full absorption of the obstacle by an edge dislocation that acquires a double superjog
This is seen when SFTs with their base above the slip plane of a positive edge dislocation are absorbed as a pair of glissile superjogs on the dislocation (see Fig. 53 below). The superjogs can thus be dragged away by the dislocation. The probability of this process increases with T and SFT size and decreasing distance between the

base and slip plane. The reaction occurs for loops in two situations. First, glissile loops with $\boldsymbol{b}_L$ inclined to the dislocation glide plane are attracted towards the dislocation. $\boldsymbol{b}_L$ of small loops changes on contact with the dislocation and becomes that of the dislocation itself (see Fig. 41 below). Large loops react with the dislocation to form a common segment with different $\boldsymbol{b}$, but this segment glides across the loop to convert $\boldsymbol{b}_L$ to the Burgers vector of the dislocation (see Fig. 42 below). Second, sessile and glissile loops away from the glide plane with $\boldsymbol{b}_L$ parallel to it may also flip under the torque of the dislocation and be absorbed by it. This reaction occurs when the loops are small and close to the slip plane, and is favoured by high T and low v_D. Another variant of R3 arises when the slip plane of an edge dislocation intersects either a Frank loop (Fig. 37) or a BCC $\langle 1\,0\,0 \rangle$ loop (see Fig. 47 below). The dislocation absorbs part of the loop after transforming the $\boldsymbol{b}_L$ of this part into its own.

5.2.4. *Reaction R4: temporary absorption of part or the entire obstacle into a helical turn on a screw dislocation*

This is the most common reaction for a screw dislocation (see Fig. 38 for Frank loops, Fig. 45 for BCC $\frac{1}{2}\langle 1\,1\,1 \rangle$ loops and Fig. 54 for SFTs). The screw dislocation absorbs an SFT or a loop, either partially or completely, to form a helical turn by a succession of cross-slip events, a process promoted by high T and low v_D. A helical turn can only glide in the direction of its $\boldsymbol{b}$ and so cannot be dragged away by the screw dislocation. Moreover, it is a very effective pinning agent because it is not localised but extended along the length of the screw dislocation. The turn has to close up in order for the dislocation to unpin, with the result that a loop with the Burgers vector of the screw dislocation is left behind.

5.2.5. *Other reactions*

Other reactions associated with particular situations.

(i) *Reaction $R1_{SFT}$: the dislocation is unchanged but an SFT is reduced in size and small clusters of vacancies form*. This variant of R1 occurs when the slip plane of the dislocation (screw or edge) coincides with the base of an SFT. A small portion of the SFT is detached, usually as a chain of vacancies, without creating a superjog on an edge dislocation. An example of $R1_{SFT}$ can be seen in Fig. 11 of Ref. [176].

(ii) *Reaction $R3_{drag}$: the obstacle is dragged by the dislocation and both remain unchanged*. This occurs in BCC and FCC metals when a glissile loop has $\boldsymbol{b}_L$ parallel to the slip plane of an edge dislocation but does not intersect it. An SIA loop is pushed by the compressive stress of the dislocation above the slip plane or dragged by the tensile stress below. This results in a loop sweeping effect, first analysed using elasticity theory in Refs [177,178]. MD simulations show that as applied stress increases a terminal velocity is reached at which the force due to the dislocation cannot overcome the loop friction and the loop is left behind. Another example of drag is seen in FCC metals when $\boldsymbol{b}_L$ of a loop that intercepts the glide plane flips to a direction in the glide plane

but not that of $\boldsymbol{b}$ of the dislocation. The loop is then attached to the gliding dislocation by a junction segment (see Fig. 35 below) and is dragged away.

Note that reactions $R3_{drag}$, R3 and R4 are potentially important as mechanisms for clear band formation in irradiated metals because all or part of the defects are carried away by the dislocations. $R3_{drag}$ and R3 have a direct effect since the edge dislocation can either drag/push the point defect cluster or absorb it into a double superjog. R4 can move defects but only by the motion of the helical turn along a screw dislocation line.

5.3. Loops in FCC metals

5.3.1. Perfect interstitial loops

In the first detailed study of edge dislocation–loop interaction using large-scale MD, Rodney and Martin [51,76] used the interatomic potential from Ref. [179] to simulate Ni. Small glissile loops containing from 4 to 37 SIAs with $\boldsymbol{b}_L = \mathbf{BD}$ (Fig. 16(b)) inclined to the dislocation glide plane were considered. A loop in this configuration can glide along its glide cylinder and react with the dislocation by reactions R3 and $R3_{drag}$ above. There exists a critical distance of a few nanometres within which the glissile loop is spontaneously attracted to, and captured by, the dislocation. Capture occurs at one of the Shockley partials of the dislocation after a rotation of $\boldsymbol{b}_L$ to a $\langle 1\,1\,0 \rangle$ direction in the glide plane. An example is shown in Fig. 35, where a 37-SIA loop is attached to the core of the **Aδ** partial after $\boldsymbol{b}_L$ changed from **BD** to **BA**, allowing for an energetically favourable junction reaction:

$$\mathbf{BA} + \mathbf{A\delta} = \mathbf{B\delta}. \tag{17}$$

The reorientation is stochastic and in some cases $\boldsymbol{b}_L$ flips to **AC** and the loop is absorbed as a pair of superjogs. Loops absorbed in this way are not obstacles to the motion of the dislocation but are dragged in the direction of their Burgers vector by the moving dislocation.

Drag of small dislocation loops by gliding edge dislocations has also been observed in MD simulations of Cu [77,180] for situations where the loop does not intersect the dislocation glide plane and has $\boldsymbol{b}_L$ parallel to it (reaction $R3_{drag}$).

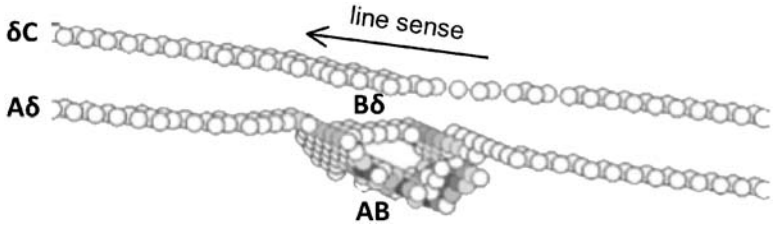

Fig. 35. Visualisation of dislocation core atoms after trapping of a 37-SIA loop at one of the Shockley partials in Ni at 100 K. (From Ref. [51].)

If placed within a few nanometres of the glide plane, such loops are trapped in the elastic field of the passing dislocation and dragged at speeds of up to several $100\,\mathrm{ms}^{-1}$, until at high enough velocity the dislocation breaks free. The friction due to a dragged loop was found to add an extra contribution, B_L, to the dislocation friction coefficient, i.e. the coefficient in eq. (6) becomes $B_{\mathrm{eff}} = B + B_L$. For loop sizes of a few tens of SIAs, B_L is of the order of 100 μPas and so larger than B (in the range 1–100 μPas). It increases with loop size, T and loop density $1/L$. A physical model for B_L was derived in Ref. [77] by noting that $B_L L$ equals the loop mobility, m_L, and that $m_L = (k_B T)/(D_L L)$, where D_L is the loop diffusivity. By using data obtained by MD for D_L of loops undergoing one-dimensional motion under the influence of temperature alone [174], the values of B_L predicted by the model are consistent with those from the simulations of drag by a dislocation.

5.3.2. Interstitial Frank loops

Several interaction configurations have to be considered, depending on the loop Burgers vector ($\boldsymbol{b}_L =$ **αA**, **βB**, **γC** or **δD**), and the dislocation character (edge or screw), Burgers vector direction ($\boldsymbol{b} =$ **AC** or **CA**) and glide direction (the dislocation may approach the loop from one side or the other). Eight sets of non-equivalent interactions were simulated at $T = 600\,\mathrm{K}$ in Ref. [46]. The loops were hexagonal with ⟨1 1 2⟩ sides, in agreement with TEM observations of irradiated austenitic steels. The case of screw dislocations has also been studied at $T = 0\,\mathrm{K}$ and $T = 100\,\mathrm{K}$ for ⟨1 1 2⟩- and ⟨1 1 0⟩-sided loops [45,181]. Potentials for Ni [179,182,183] or Cu [183] were used to provide models with stacking fault energy within the range for austenitic steels. In the simulations in Ref. [46], the loop diameter, D, was 6 nm and $L = 50\,\mathrm{nm}$, so that the defect density, N, corresponded to values observed experimentally, i.e. inter-loop distance in glide plane 50 nm $\sim 1/\sqrt{ND}$ with $D = 6\,\mathrm{nm}$ and $N \sim 5 \times 10^{22}\,\mathrm{m}^{-3}$.

The interaction mechanisms found cover all reactions presented in Section 5.2. Loops are absorbed only after they have been unfaulted, $\boldsymbol{b}_L$ usually being transformed into that of the dislocation. Unfaulting always starts by a cross-slip event on the dislocation and so edge dislocations, which can cross-slip only if bent to become screw, shear Frank loops in most configurations. Screw dislocations, on the other hand, unfault Frank loops in most configurations when cross-slip is promoted by high T (600 K). At low T (100 K), the shape of the Frank loops matters. Loops with ⟨1 1 0⟩ sides are more easily absorbed than those with ⟨1 1 2⟩ sides because in the former case, four of the six sides lie in {1 1 1} planes, allowing the dislocation to cross-slip and recombine with them, while in the latter case, no sides are in {1 1 1} planes. It has also been shown that the presence of a second dislocation in the simulation cell, which mimics an embryonic pile-up, favours cross-slip and unfaulting by increasing the resolved shear stress in cross-slip planes [46]. Three illustrative examples are now presented.

R1/R2: loop shearing. Fig. 36 shows an **AC** edge dislocation gliding in the $+x$ direction on the plane ABC and reacting with a **γC** Frank loop on plane ABD. The dislocation simply cuts through the loop at a low stress of 95 MPa, forming a stable step on the loop, visible in (b). When the edge dislocation re-enters through the

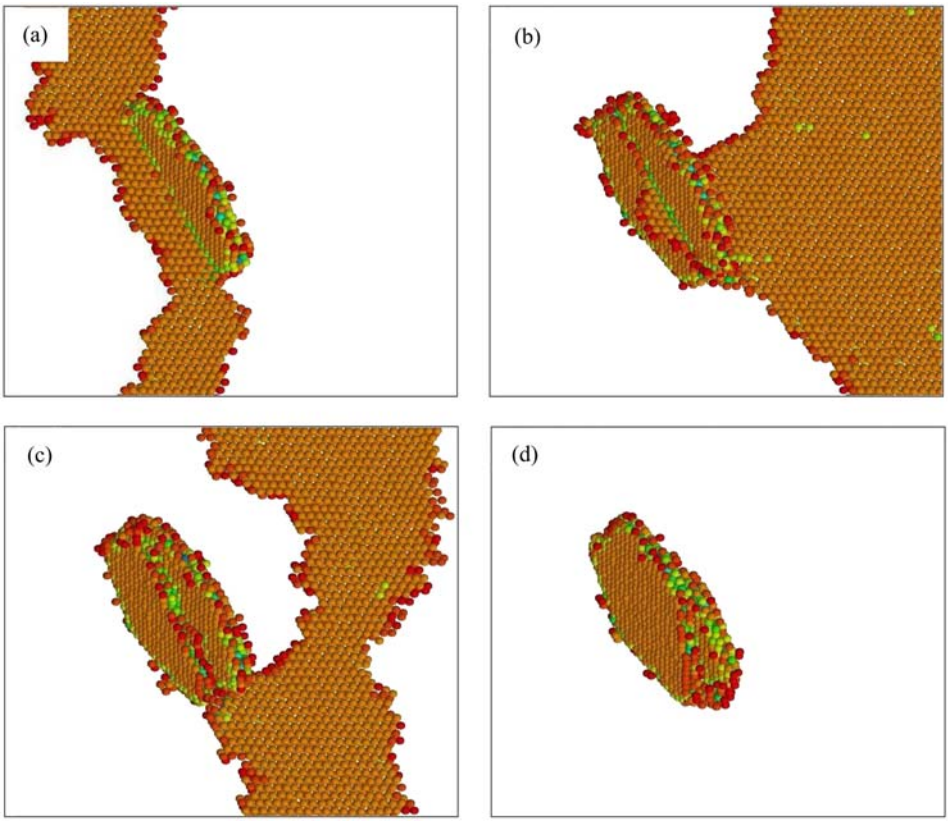

Fig. 36. Interaction of an edge dislocation with a Frank loop in an attractive configuration in Cu at 600 K leading to shear of the loop (reaction R2): snapshots shown at (a) 55 MPa, (b) 95 MPa, (c) 95 MPa and (d) 95 MPa. (From Ref. [46].)

periodic boundaries and shears the defect again, the double step that is formed becomes mobile in the loop surface and annihilates on the loop border, as in (c), thus reforming a faulted loop without damage seen in (d).

R3: loop absorption and drag. The process shown in Fig. 37 has a negative edge dislocation ($\boldsymbol{b} = \mathbf{CA}$) gliding in the $+x$ direction to react with a $\boldsymbol{\gamma}\mathbf{C}$ Frank loop. The loop initially repels the dislocation, but when $\tau = 60$ MPa the dislocation contacts the loop (a), then bends and constricts to acquire a screw segment that cross-slips (b). This segment creates a D-Shockley, i.e. two Shockley partials on adjacent {1 1 1} planes, by the reaction $\boldsymbol{\gamma}\mathbf{C} + \mathbf{CA} = \boldsymbol{\gamma}\mathbf{A}$. The loop starts to unfault as the cross-slipped segment rotates around the upper part of the loop (c). The second dislocation arm acquires screw character and also cross-slips, and when the two cross-slipped segments meet, the upper part of the loop is absorbed by the line (d), which glides away at $\tau = 130$ MPa, leaving the lower, faulted part behind as seen in (e, f).

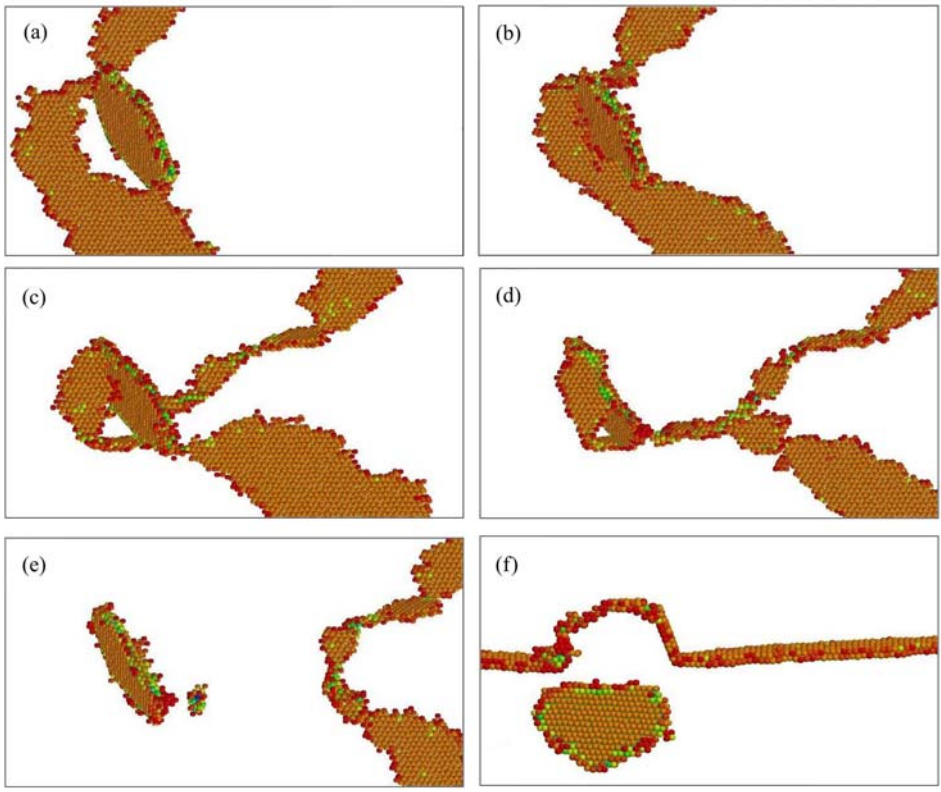

Fig. 37. Interaction of an edge dislocation with a Frank loop in a repulsive configuration in Cu at 600 K leading to the partial loop absorption (reaction R3): snapshots shown at (a) 65 MPa, (b) 105 MPa, (c) 130 MPa, (d) 130 MPa, (e) 130 MPa and (f) 130 MPa with a different viewing angle. (From Ref. [46].)

R4: loop absorption into a helical turn. Fig. 38 shows six stages in the interaction of an **AC** screw dislocation gliding in the $+y$ direction with an $\boldsymbol{\alpha}\mathbf{A}$ Frank loop with $\langle 1\,1\,0 \rangle$ sides as τ is increased from 0 to 400 MPa at $T = 0$ K. The dislocation gliding on plane ABC in (a) constricts at the point where it first contacts the loop and then cross-slips in (b) onto ACD to combine with a loop side to form a D-Shockley partial by the reaction $\mathbf{AC} + \boldsymbol{\alpha}\mathbf{A} = \boldsymbol{\alpha}\mathbf{C}$. This partial dislocation unfaults the loop by sweeping over its surface as the **AC** dislocation cross-slips at the remaining loop sides, see (c–e). This process converts the loop into a helical turn on the screw dislocation (e, f). As mentioned in Section 5.1, the helical turn is an obstacle for glide of the screw dislocation and it offers high resistance because, as seen in (f), it is not localised but expands over the length of the dislocation in order to minimise its line energy.

Fig. 39 shows that with increasing τ the dislocation escapes by the bowing of the segments dissociated in ABC planes, thereby forcing the helical turn to close on itself so that a perfect interstitial loop with $\boldsymbol{b}_{\mathrm{L}} = \mathbf{AC}$ is left behind. Absorption is controlled by cross-slip reactions on the screw dislocation. Thus, at high T (600 K),

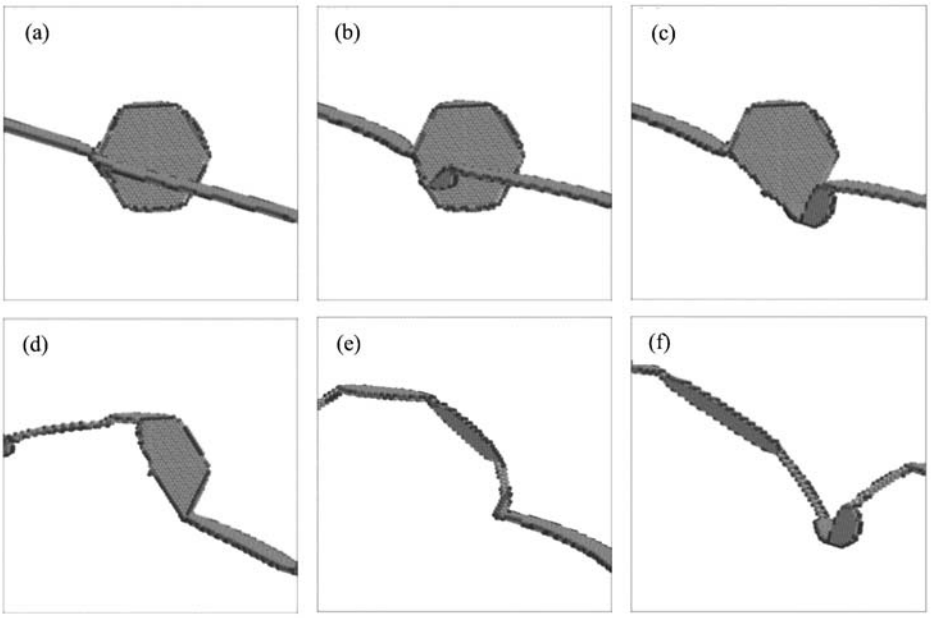

Fig. 38. Interaction of a screw dislocation with a ⟨1 1 0⟩-sided Frank loop in Ni at $T = 0$ K (reaction R4). (From Ref. [181].)

such events have a high probability and occur in all configurations with ⟨1 1 0⟩- and ⟨1 1 2⟩-sided loops except one configuration (**AC** screw dislocation gliding in $-x$ direction and reacting with an **αA** ⟨1 1 2⟩-Frank loop). At 300 K loops with ⟨1 1 0⟩ sides are absorbed but ⟨1 1 2⟩-sided loops are sheared because, as mentioned above, their sides do not belong to {1 1 1} planes.

The critical stress τ_c for a screw dislocation to overcome rows of Frank loops with different values of spacing, L, at 100 K is plotted in Fig. 40. The data are compared with dashed lines showing the stress given by continuum modelling of the Orowan process, i.e. eq. (14) with $A = (1 - \nu)$, $\Delta = 0.615$ and effective size D close to the real size of the loops [45]. The good agreement shows that τ_c is determined by the condition that the screw dislocation has to bow out in order to unpin from these strong obstacles. We note that upon unpinning, the dislocation is re-emitted in a {1 1 1} plane parallel but different from its initial glide plane. This is due to the 3-D structure of the helical turn, which contains no segment in the initial glide plane of the dislocation. The process shown in Fig. 39 clearly depends on the periodic boundary conditions along the dislocation line, but dislocation re-emissions in new glide planes have also been observed with multiple loops that break the periodicity [46] as well as in DD simulations without periodic boundaries [22]. This effect is believed to play a role in the broadening of clear bands in irradiated metals since it allows screw dislocations to change glide plane through a mechanism analogous to double cross-slip [22,46].

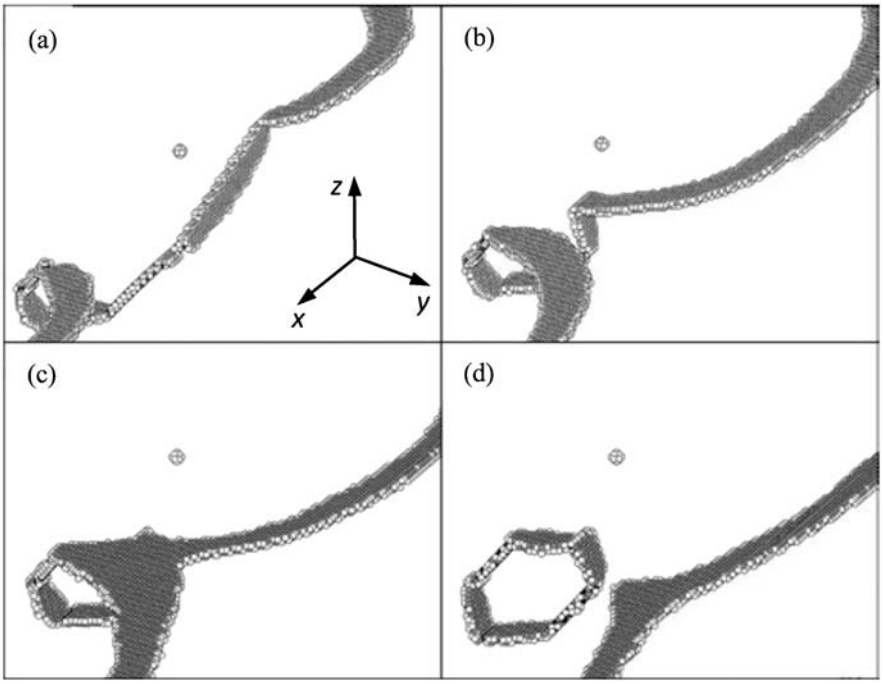

Fig. 39. Unpinning of a screw dislocation from a helical turn (reaction R4) at different times (in ps) in Ni under $\tau = 600$ MPa at $T = 100$ K: (a) 18, (b) 24, (c) 25.2 and (d) 27. (From Ref. [45].)

5.4. Interstitial loops in BCC metals

5.4.1. ½⟨1 1 1⟩ loops

Depending on the orientation of $\boldsymbol{b}_L$, two cases can be distinguished in the interaction of a ½[1 1 1](1 $\bar{1}$ 0) *edge dislocation* with ½⟨1 1 1⟩ loops. First, two of the four $\boldsymbol{b}_L$ orientations, namely ½[1 1 1] and ½[1 1 $\bar{1}$], are parallel to the dislocation glide plane and these loops can be dragged (reaction $R3_{drag}$ in Section 5.2). This situation was considered in Refs [180,184] for hexagonal loops containing either 37 or 61 SIAs, with centres between 3 and 9 nm below the glide plane of the positive edge dislocation. The process is as described in Section 5.3.1.

The second case concerns loops with $\boldsymbol{b}_L = ½[1\ \bar{1}\ 1]$ and ½[$\bar{1}$ 1 1] inclined to the glide plane. (They are equivalent for the ½[1 1 1](1 $\bar{1}$ 0) dislocation.) Hexagonal loops with ⟨1 1 2⟩ sides and centres placed initially below the glide plane have been simulated for a variety of numbers of SIAs: 37 and 331 [184], 99 [185] and 169 [186]. Sensitivity of results to the interatomic potential was examined by using the potential of Ref. [69] in Ref. [184] and that of Ref. [70] in Ref. [186]. As mentioned in Section 5.1, ½⟨1 1 1⟩ loops move easily by one-dimensional glide, and if within a few nanometres of a gliding edge dislocation, slip on their glide prism under

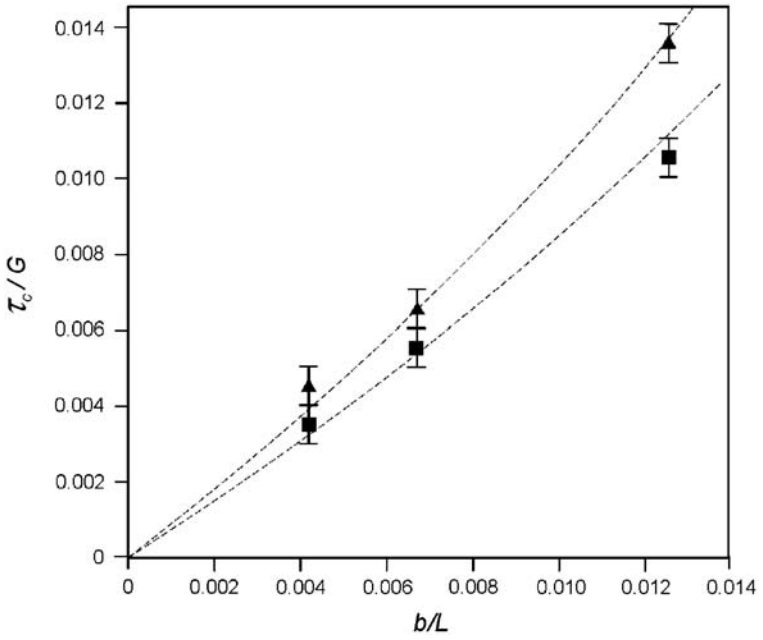

Fig. 40. Variation of τ_c, in units of G (taken to be 74.6 GPa), with b/L for hexagonal Frank loops with either $\langle 1\,1\,0 \rangle$ sides (triangles) or $\langle 1\,1\,2 \rangle$ sides (squares) in Ni at $T = 100$ K. Dashed lines are the Orowan stress predicted from elasticity theory (eq. (14)). (From Ref. [45].)

attractive elastic interaction and react on contact with the dislocation. The outcome depends on both the defect size and, for large loops, the temperature.

Small loops (37 SIAs) undergo an R3 reaction, for $\boldsymbol{b}_L$ rotates spontaneously to that of the dislocation and the loop is thereby absorbed and moved away as a double superjog. τ_c falls from 51 MPa at 0 K to 13 MPa at 450 K for $L = 41$ nm. Two stages in this process at $T = 0$ K are shown in Fig. 41. These interstitial loops are weaker obstacles than voids with a similar number (27 or 59) of vacancies (Figs 18 and 28).

Large loops (≥ 99 SIAs) are unable to change $\boldsymbol{b}_L$ in this way, presumably because the energy barrier is too large. Two interaction mechanisms are observed, depending on T. An example for high T is provided in Fig. 42 for the case of a 331-SIA loop at $T = 300$ K and $\dot{\varepsilon} = 20 \times 10^6\ \mathrm{s}^{-1}$. When the loop contacts the dislocation, a [0 1 0] junction segment forms by the energetically favourable reaction

$$\frac{1}{2}[1\ 1\ 1] - \frac{1}{2}[1\ \bar{1}\ 1] = [0\ 1\ 0], \tag{18}$$

and the remainder of the loop retains its ½[1 $\bar{1}$ 1] Burgers vector, as shown in (b). The [0 1 0] segment is sessile in the (1 $\bar{1}$ 0) slip plane, but glissile in the inclined (1 0 $\bar{1}$) plane. However, it is pinned at its ends by the junctions with the ½[1 1 1] and ½[1 $\bar{1}$ 1] lines, and is too short to bow under the applied stress. As τ increases, the

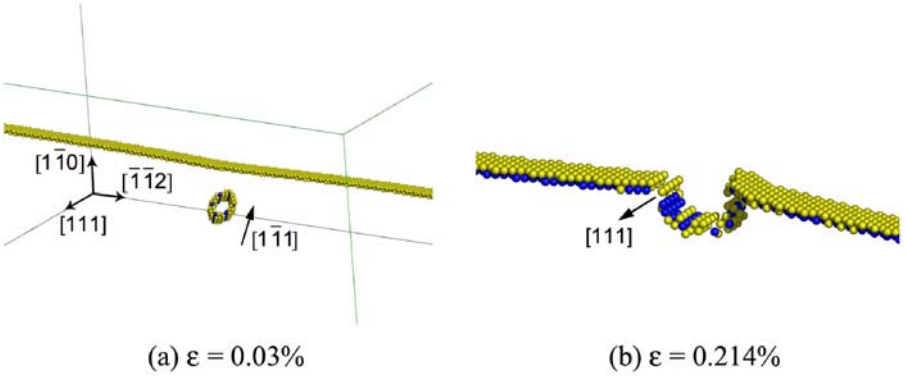

Fig. 41. Visualisations of the spontaneous glide and absorption process of a 37-SIA loop on an edge dislocation in Fe at $T = 0\,\mathrm{K}$ (reaction R3). (Reprinted from Ref. [184] with permission from Taylor & Francis Ltd., http://www.informaworld.com.)

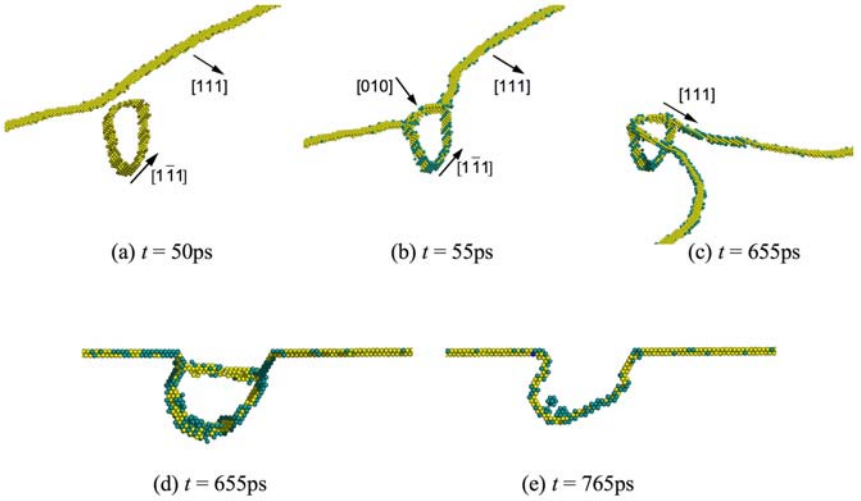

Fig. 42. Visualisation of the spontaneous glide and transformation process of a 331-SIA loop in Fe at $T = 300\,\mathrm{K}$ and $\dot{\varepsilon} = 20 \times 10^6\ \mathrm{s}^{-1}$ (reaction R3). (Reprinted from Ref. [184] with permission from Taylor & Francis Ltd., http://www.informaworld.com.)

½[1 1 1] line segments pinned at the junctions are pulled into the screw orientation in (c) and, assisted by the applied force on the [0 1 0] segment, cross-slip on (1 0 $\bar{1}$) planes, thereby allowing the [0 1 0] segment to move downwards on its (1 0 1) glide plane, as in (d). Slip of this segment transforms the Burgers vector of the remainder of the loop by the reaction

$$\frac{1}{2}[1\ \bar{1}\ 1] + [0\ 1\ 0] = \frac{1}{2}[1\ 1\ 1], \tag{19}$$

and results again in the formation of a pair of superjogs on the gliding dislocation (e). Large ½[1 $\bar{1}$ 1] loops at high enough temperature are thus absorbed and dragged as in reaction R3. τ_c is 220 MPa and the jogged dislocation line continues to glide at $\tau = 12$ MPa. The same reaction and transformation process occurs for other strain rates at 300 and 450 K, and with the sense of the applied strain reversed, i.e. the dislocation approaching the loop from the other side. The dependence of τ_c on T and $\dot{\varepsilon}$ is illustrated by the data plotted in Fig. 43.

In contrast to this, the reaction with large ½[1 $\bar{1}$ 1] loops at low T is of R1 type. The process is illustrated in Fig. 44 for a 331-SIA loop at 100 K, for which $\tau_c = 290$ MPa. A [0 1 0] segment again forms and a screw dipole is pulled out of the dislocation as at high T. However, the mobility of the [0 1 0] segment is strongly reduced at low T and the screw dipole reaches a longer extension and annihilates by cross-slip before the [0 1 0] segment becomes mobile. The ½[1 $\bar{1}$ 1] loop is thus restored and left behind when the dislocation breaks away. The critical dipole length and τ_c increase when T decreases further – e.g. $\tau_c = 530$ MPa at 1 K for a 169-SIA loop – because of the low mobility of the BCC screw dislocation at low T.

Unlike the situation for small loops, τ_c for large loops is higher than for voids containing a similar number of point defects, e.g. when $L = 41.4$ nm, $T = 300$ K and $\dot{\varepsilon} = 5 \times 10^6\ s^{-1}$, $\tau_c = 212$ MPa for the 4.9 nm loop containing 331 SIAs compared with 150 MPa for a 2 nm void containing 339 vacancies (Fig. 28). This is probably due to the fact that the effective obstacle size is larger for the loop. The critical line shape consisting of parallel screw segments at the obstacle is the same in both cases,

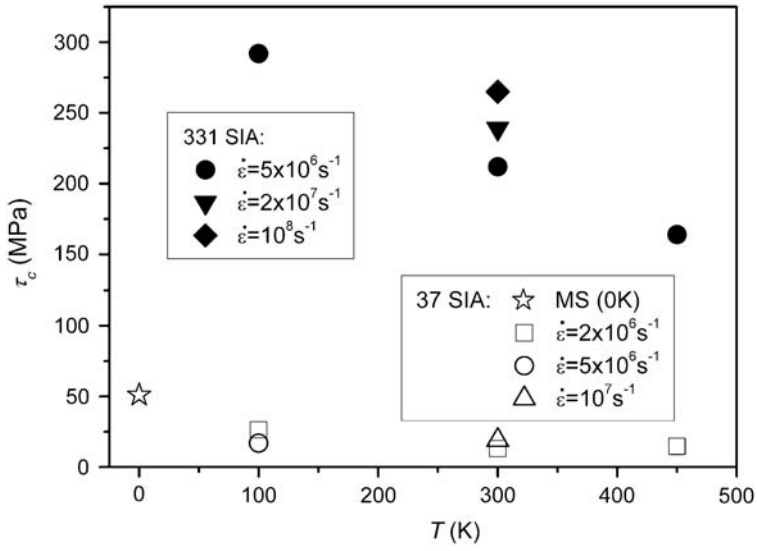

Fig. 43. Temperature dependence of τ_c for 37-SIA and 331-SIA loops in Fe for various values of $\dot{\varepsilon}$ in units of $10^6\ s^{-1}$. The value of τ_c at 0 K for the small loop obtained by MS simulation is also shown. (Reprinted from Ref. [184] with permission from Taylor & Francis Ltd., http://www.informaworld.com.)

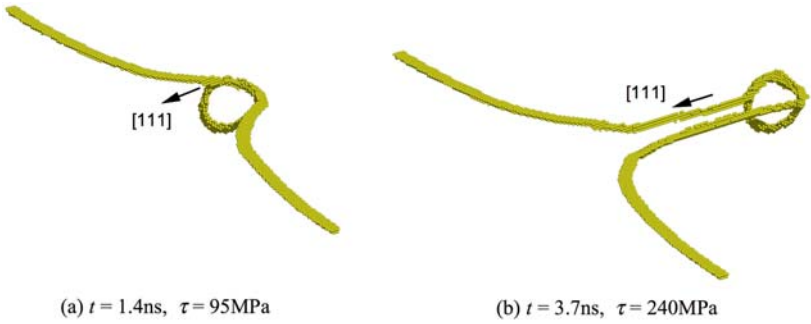

Fig. 44. Visualisations of the interaction process for a 331-SIA loop in Fe at $T = 100$ K and $\dot{\varepsilon} = 5 \times 10^6$ s^{-1} (reaction R1). (Reprinted from Ref. [184] with permission from Taylor & Francis Ltd., http://www.informaworld.com.)

but the dipole spacing is larger for the loop and τ_c scales roughly as the logarithm of the obstacle size for this configuration (eq. (14)).

Less attention has been paid to the interaction of *screw dislocations* with $\frac{1}{2}\langle 1\,1\,1\rangle$ loops in BCC metals. Liu and Biner [187] have simulated the interaction with a $\frac{1}{2}[1\,\bar{1}\,1]$ hexagonal loop containing either 37, 127 or 271 SIAs in Fe at 100 or 300 K using the interatomic potential from Ref. [70]. Free boundaries were imposed in the $[1\,1\,\bar{2}]$ glide direction while a mixture of fixed and rigid boundaries was used in the $[1\,\bar{1}\,0]$ direction to apply strain at a constant rate in the range $0.8–3 \times 10^8$ s^{-1}. As with edge dislocations, the loop is attracted to just above the $(1\,\bar{1}\,0)$ slip plane as the dislocation approaches. Then, depending on the loop size, one of two mechanisms occurs. The $\boldsymbol{b}_L$ of a *small* loop (37 SIAs) changes to $\frac{1}{2}[1\,1\,1]$ and the loop is absorbed on the line to form a helical turn (reaction R4) (see Fig. 3 of Ref. [187]), a similar configuration to that found in MS simulations in Ref. [188]. Loops with 127 or 271 SIAs form a segment with $\boldsymbol{b} = [0\,1\,0]$ by the favourable reaction of eq. (18). The dislocation eventually converts the other sides of the loop to $\boldsymbol{b} = [0\,1\,0]$ before breakaway, as illustrated in Fig. 45 (reaction R2).

5.4.2. $\langle 1\,0\,0\rangle$ loops

The variety of mechanisms and obstacle strengths is wider for these. Some reactions end with complete absorption of the loop by the formation of superjogs (R3), whereas others result in almost no absorption (R2). There is no apparent correlation between τ_c and the amount of absorption. In some cases, the residual loop retains its original $\langle 1\,0\,0\rangle$ Burgers vector while in others it is partially transformed into $\frac{1}{2}\langle 1\,1\,1\rangle$ type.

Terentyev et al. [189] modelled a $\frac{1}{2}[1\,1\,1](1\,\bar{1}\,0)$ *edge dislocation* and a periodic row of interstitial dislocation loops with $L = 41$ nm and $\boldsymbol{b}_L = [1\,0\,0]$, $[0\,1\,0]$ or $[0\,0\,1]$ in Fe at $T = 300$ K under an applied strain rate of 10^7 s^{-1}. The square loops had $\langle 1\,0\,0\rangle$ or $\langle 1\,1\,0\rangle$ sides and contained either 162 or 169 SIAs, respectively. Results were compared for two different interatomic potentials for Fe [69,70]. It was found that τ_c, varies from 30 to 220 MPa, depending on the orientation of $\boldsymbol{b}_L$ and the

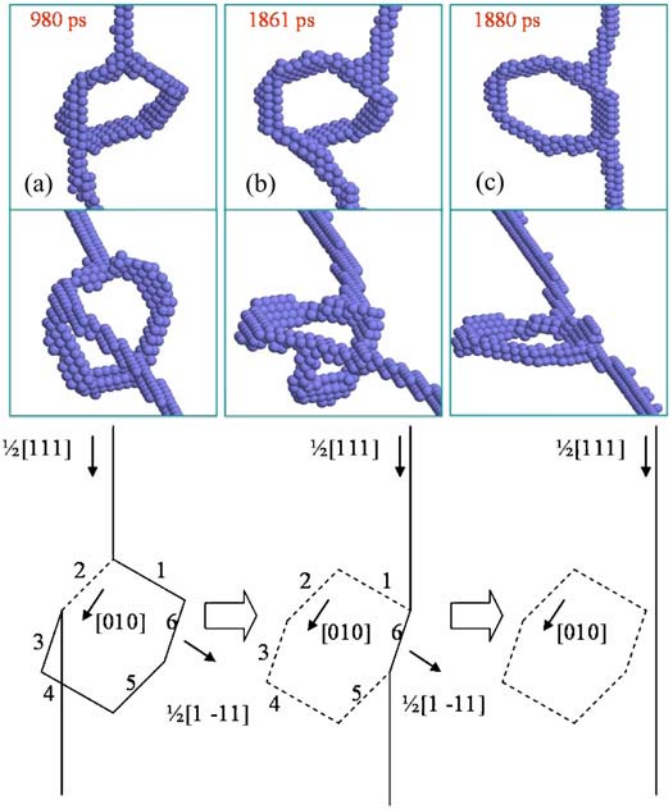

Fig. 45. Snapshots from two perspectives of the interaction of a screw dislocation with a 127-SIA loop in Fe at 100 K at the times indicated (reaction R4). The process is shown schematically in the lower figures. (Reprinted from Ref. [187] with permission from Elsevier Ltd. http://www.sciencedirect.com/science/.)

position of the loop relative to the glide plane. In general, the passage of the dislocation through a row of loops with $\boldsymbol{b}_L = [0\,0\,1]$ parallel to the dislocation glide plane requires the highest stress (100–220 MPa). The two other classes of loop with $\boldsymbol{b}_L = [1\,0\,0]$ and $[0\,1\,0]$ offer less resistance to dislocation motion, τ_c varying from 30 to 190 MPa. Reactions requiring high τ_c for dislocation unpinning are mainly those where either part of the loop transforms to $\boldsymbol{b} = \frac{1}{2}\langle 1\,1\,1\rangle$ and the remaining $\langle 1\,0\,0\rangle$ part is sessile (reaction R2) or the dislocation is strongly attracted to the $\langle 1\,0\,0\rangle$ loop that cannot glide with it. Reactions resulting in low τ_c are those where a $\frac{1}{2}[1\,\bar{1}\,1]$ or $\frac{1}{2}[\bar{1}\,1\,1]$ segment is created and quickly propagates across the loop surface, converting it into $\boldsymbol{b} = \frac{1}{2}[1\,1\,1]$ superjogs on the dislocation line (reaction R3). The following three examples illustrate some effects.

Of the three $\langle 1\,0\,0\rangle$ loop vectors, only $\boldsymbol{b}_L = [0\,0\,1]$ results in a product segment that is glissile in the $(1\,\bar{1}\,0)$ slip plane. This case is illustrated in Fig. 46. The dislocation motion is from right to left and initially results in the formation of a

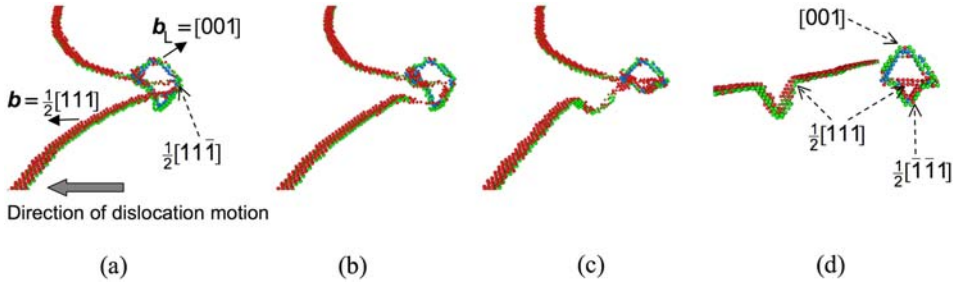

Fig. 46. Visualisation of the interaction between a ½[1 1 1](1 $\bar{1}$ 0) edge dislocation and a [0 0 1] loop in Fe at 300 K (reaction R3): $\tau_c = 175$ MPa. (From Ref. [189].)

short ½[1 1 $\bar{1}$] segment on contact with the first corner of the loop (see (a)) by the reaction

$$\frac{1}{2}[1\ 1\ 1] + [0\ 0\ \bar{1}] = \frac{1}{2}[1\ 1\ \bar{1}]. \tag{20}$$

Under increasing stress, the dislocation arms bow out until one touches the opposite corner, creating another short ½[1 1 $\bar{1}$] segment. At this stage the outer arms of the dislocation are pinned at the opposite corners, which are linked by a ½[1 1 1] segment that bisects the original loop, and as the line bows forward a screw dipole is formed (see (b)). At $\tau_c = 175$ MPa one of the two screw arms cross-slips down and then up on a V-shaped surface of (1 0 $\bar{1}$) and (0 1 $\bar{1}$) planes (see (c)), thereby converting $\boldsymbol{b}_L$ below the slip plane by the reaction

$$[0\ 0\ 1] - \frac{1}{2}[1\ 1\ 1] = \frac{1}{2}[\bar{1}\ \bar{1}\ 1]. \tag{21}$$

The dipole then detaches from the final loop corner (see (d)) and glides away with a set of superjogs containing about 25% of the original interstitials. This leaves two conjoined triangular loops with a common $\boldsymbol{b}_L = ½[1\ 1\ 1]$ segment: the upper part is half of the pre-existing [0 0 1] loop and the lower has $\boldsymbol{b}_L = ½[\bar{1}\ \bar{1}\ 1]$.

Fig. 47 shows three stages in the interaction with a [0 1 0] loop. The line is initially repelled by the loop but under increasing τ makes contact in the middle of the two [0 1 0] sides (see (a)). The upper part of the loop converts spontaneously to $\boldsymbol{b} = ½[1\ \bar{1}\ 1]$ by the reaction

$$\frac{1}{2}[1\ 1\ 1] - [0\ 1\ 0] = \frac{1}{2}[1\ \bar{1}\ 1] \tag{22}$$

and slips on its glide prism to below the dislocation glide plane (see (b)). The configuration formed in this way is the same as that depicted in Fig. 42, in which a ½[1 1 1] dislocation and ½[1 $\bar{1}$ 1] loop interact to form a product segment with $\boldsymbol{b} = [0\ 1\ 0]$. The remainder of the interaction is identical to Fig. 42 and the loop is eventually converted to a ½[1 1 1] superjog.

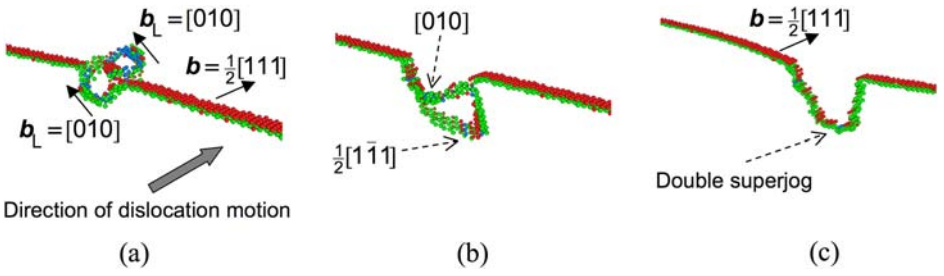

Fig. 47. Visualisation of the interaction between a ½[1 1 1](1 $\bar{1}$ 0) edge dislocation and a [0 1 0] loop in Fe at 300 K (reaction R3): $\tau_c = 125$ MPa. (From Ref. [189].)

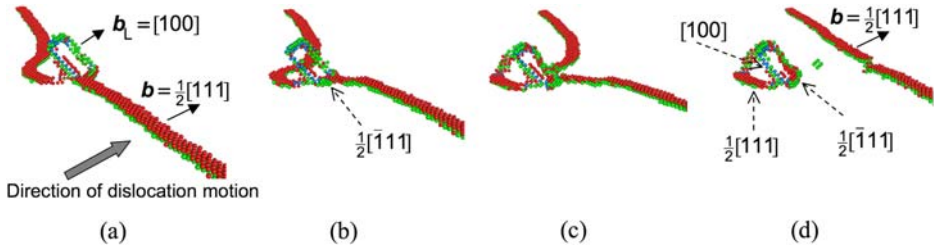

Fig. 48. Visualisation of the interaction between a ½[1 1 1](1 $\bar{1}$ 0) edge dislocation and a [1 0 0] loop in Fe at 300 K (reaction R2): $\tau_c = 110$ MPa. (From Ref. [189].)

The third reaction shown in Fig. 48 involves a [1 0 0] loop positioned initially with its lower [0 0 1] side lying in the dislocation glide plane. The dislocation is initially repelled by the loop, but under increasing τ contacts the lower side first at one corner and then the other (see (a)). The segment of the gliding dislocation between the corners bows backwards due to repulsion (see (b)). As the sidearms of the dislocation bow towards each other under increasing τ (see (c)), the lower half of the loop is converted to $\boldsymbol{b} = \frac{1}{2}[\bar{1}\ 1\ 1]$ by the reaction

$$\frac{1}{2}[1\ 1\ 1] - [1\ 0\ 0] = \frac{1}{2}[\bar{1}\ 1\ 1]. \tag{23}$$

The arms meet and breakaway at $\tau_c = 110$ MPa (see (d)). The final product is a ½[1 1 1] shear loop in the (1 $\bar{1}$ 0) slip plane sharing a (pre-existing) [1 0 0] segment with a ½[$\bar{1}$ 1 1] loop formed by reaction (23).

With regard to the transformation of ⟨0 0 1⟩ loops into mixed ⟨0 0 1⟩/⟨1 1 1⟩ loops, we note that previous computer simulations have shown that such double-loop configurations can form due to interactions between gliding interstitial clusters [190–192]. For example, the reaction product of Fig. 46(d) is also formed by a favourable reaction between two interstitial loops of similar size and Burgers vector [0 0 1] and ½[$\bar{1}$ $\bar{1}$ 1]. MD simulations reveal that this double-loop product is stable and immobile for at least 10 ns at temperature up to 1000 K [192]. The two-loop

complex of Fig. 48(d), which can form by reaction between ½[1 1 1] and ½[$\bar{1}$ 1 1] loops, is unstable, however, for it transforms in the field of another edge dislocation to the original perfect square loop with $\boldsymbol{b}_L = [1\,0\,0]$.

Concerning ½⟨1 1 1⟩ *screw dislocations*, Marian et al. [193] have simulated the interaction with a 113-SIA square loop with $\boldsymbol{b}_L = [1\,0\,0]$ in Fe at 100 K using the interatomic potential from Ref. [69]. Free-surface conditions were imposed along the [1 1 $\bar{2}$] glide direction of the dislocation and in the [1 $\bar{1}$ 0] direction and shear tractions were imposed on the (1 $\bar{1}$ 0) surfaces to apply stress. Under a constant stress $\tau = 750$ MPa, the dislocation moved towards the loop by kink generation and, at the same time, two opposite sides of the loop transformed into two ½⟨1 1 1⟩ segments by the reaction

$$[1\,0\,0] = \frac{1}{2}[1\ 1\ 1] + \frac{1}{2}[1\ \bar{1}\ \bar{1}]. \tag{24}$$

This is not energetically favourable according to Frank's rule for the energy change when parallel dislocations react and is presumably assisted by the stress and/or presence of the screw dislocation. The resulting configuration is shown in Fig. 49(a). As the screw dislocation moves closer, a perfect ½[1 1 1] loop is emitted from the original loop (see (b) and (c)) and is absorbed on the line as a helical turn while the remaining [1 0 0] loop is trapped on the line by a common ½[1 $\bar{1}$ $\bar{1}$]

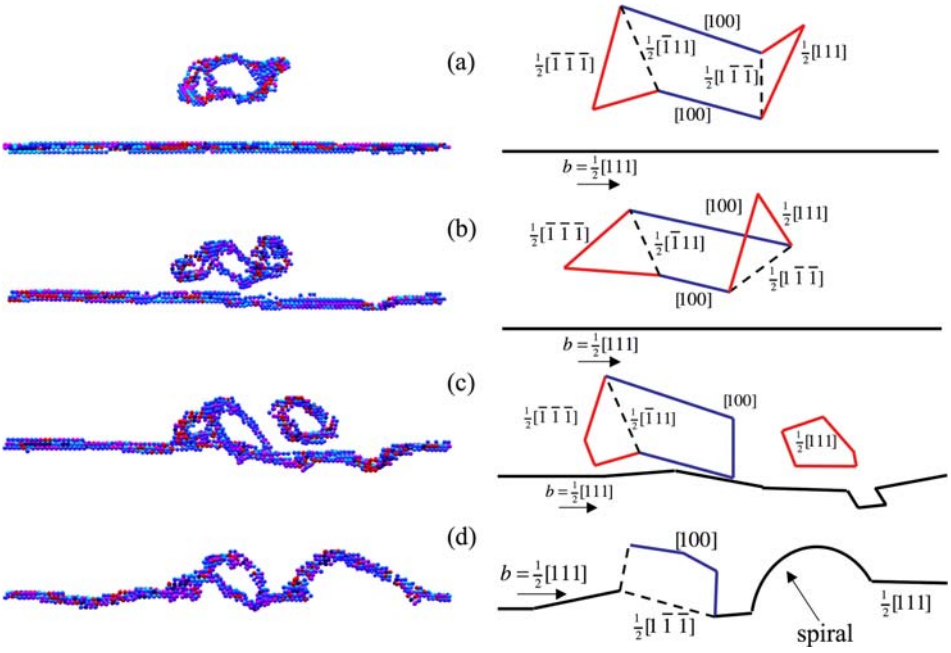

Fig. 49. Stages in the interaction between a 113-SIA [1 0 0] loop and a ½[1 1 1] screw dislocation in Fe at 100 K under $\tau = 750$ MPa (reaction R4). (Reprinted from Ref. [193] with permission from Elsevier Ltd. http://www.sciencedirect.com/science/.)

segment (see (d)). By increasing τ in 50 MPa increments, it was found that the dislocation broke through the obstacle at $\tau = 1$ GPa, an increase of 250 MPa over the stress for glide of the screw alone. It remains to be seen what the effects of loop size, side and $\boldsymbol{b}_L$ orientation, and interatomic potential are on the interaction between screw dislocations and $\langle 1\,0\,0 \rangle$ loops.

5.4.3. Comparison of obstacle strength for voids and loops in iron

On the basis of the simulations reviewed in this section, Terentyev et al. [189], have compared τ_c obtained under the same simulation conditions ($L = 41$ nm, $T = 300$ K, $\dot{\varepsilon} = 10^7\ s^{-1}$) for interaction of a $\frac{1}{2}[1\,1\,1](1\,\bar{1}\,0)$ edge dislocation with a row of obstacles consisting of either spherical voids or $\frac{1}{2}\langle 1\,1\,1 \rangle$ or $\langle 1\,0\,0 \rangle$ interstitial dislocation loops in Fe modelled with the interatomic potential in Ref. [70]. Each obstacle contained approximately the same number of point defects, namely 169 for voids and $\frac{1}{2}\langle 1\,1\,1 \rangle$ loops, and 162 or 169 for $\langle 1\,0\,0 \rangle$ loops. The values of τ_c are plotted in Fig. 50, which also contains values for $\frac{1}{2}\langle 1\,1\,1 \rangle$ loops and voids of smaller and larger size. The Burgers vectors of the loops considered are shown along the abscissa of the figure and the labels C1, etc. were used in Ref. [189] to denote the position of the $\langle 1\,0\,0 \rangle$ loops with respect to the dislocation glide plane and the orientation of their sides. Of the four orientations of loops with $\boldsymbol{b}_L = \frac{1}{2}\langle 1\,1\,1 \rangle$, those plotted for $\boldsymbol{b}_L$ inclined to the dislocation slip plane, i.e. $\frac{1}{2}[\bar{1}\,1\,1]$

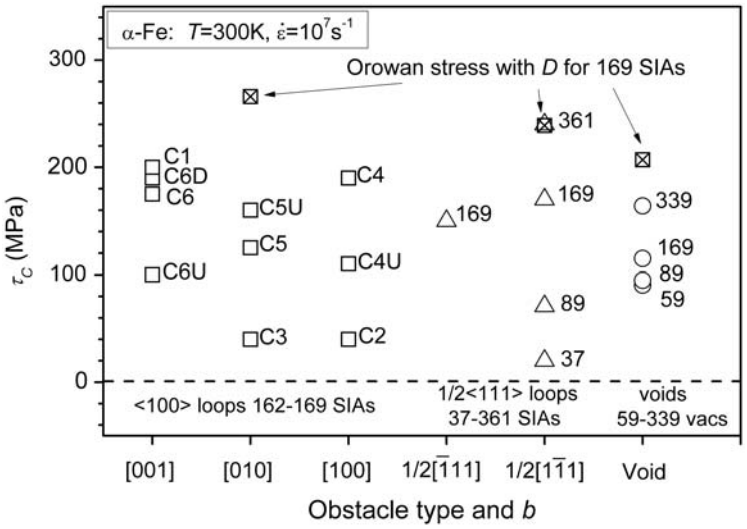

Fig. 50. Comparison of τ_c for $\langle 1\,0\,0 \rangle$ and $\frac{1}{2}\langle 1\,1\,1 \rangle$ interstitial loops and voids in Fe modelled with the potential in Ref. [70] for the conditions $L = 41$ nm, $T = 300$ K, $\dot{\varepsilon} = 10^7\ s^{-1}$. The labels for the $\langle 1\,0\,0 \rangle$ loop configurations are those defined in Ref. [189]: filled symbols for loops with $\langle 1\,0\,0 \rangle$ sides (162 SIAs), open symbols for $\langle 1\,1\,0 \rangle$ sides (169 SIAs). The number of SIAs in the $\frac{1}{2}\langle 1\,1\,1 \rangle$ loops (37–361) and vacancies in the voids (59–339) are indicated against the data points. The values given by eq. (14) are labelled 'Orowan stress'. (After Ref. [189].)

or ½[1 $\bar{1}$ 1], are relatively strong obstacles. The void of 169 vacancies is a weaker obstacle than either the ½⟨1 1 1⟩ loops or some of the ⟨1 0 0⟩ loops containing the same number of SIAs.

It should be borne in mind that loops and voids containing 169 point defects are not fully representative of the size spectrum of point defect clusters in irradiated metals, and it is clear from the additional τ_c values for larger and smaller clusters plotted in Fig. 50 that the size-dependence of τ_c is different for loops and voids. The data for ½[1 $\bar{1}$ 1] loops demonstrate a 10-fold increase in τ_c as the number of interstitials increases from 37 to 331. This is because smaller loops are readily absorbed as a pair of superjogs by spontaneous transformation of $\boldsymbol{b}_L$ to ½[1 1 1]. Larger loops react with the dislocation so that one side forms a common segment with $\boldsymbol{b} = [0\,1\,0]$, which is sessile in the (1 $\bar{1}$ 0) plane and presents a strong obstacle. The obstacle strength of voids, in contrast, has a much weaker variation with number of vacancies because the mechanism of edge dislocation cutting and unpinning is not strongly dependent on diameter. As D increases, the dislocation branches pinned at the void surface approach more closely to the screw orientation, and τ_c increases (see Section 4.2.1). As a result, voids are weaker obstacles than many loops when large, but stronger when small. Furthermore, the strength of voids has weaker T-dependence than that of ½⟨1 1 1⟩ loops [118,186]. All the τ_c data obtained by MD simulation with $T = 300\,\mathrm{K}$ fall below the values predicted by eq. (14). The continuum approximation used for that equation mimics a crystal at $T = 0\,\mathrm{K}$, i.e. no kinetic effects are considered. It was seen in Section 4.2.1 that τ_c obtained by atomic-level simulation of void strengthening approaches the critical value given by eq. (14) as T tends to 0 K if D is $\geq 2\,\mathrm{nm}$. Although the ⟨1 0 0⟩ loops that provide the strongest resistance, such as those labelled C1, C4, C6D and C6 in Fig. 50, cause the dislocation sidearms to bow to the screw orientation as applied stress increases, dislocation breakaway occurs before a stable screw dipole is drawn out. Thus, temperature (and possibly applied strain rate) affects the dislocation release mechanism and the measured obstacle strength falls below the theoretical limit represented by eq. (14).

5.5. Stacking fault tetrahedra

5.5.1. Particular reactions

Interactions involving SFTs have been simulated extensively for both edge and screw dislocations and a wide range of interactions was observed [49,118,176,194–199]. We present here examples of the main reaction types following the categories described in Section 5.2. First, however, it is necessary to identify SFT-specific parameters that arise from the geometry of the interaction. The Thompson tetrahedron shown in Fig. 16(b) shows an SFT configuration. An SFT has two orientations (*Face* and *Edge*) relative to the approaching dislocation and two orientations of its apex (*Up* and *Down*) relative to the dislocation slip plane. Due to the symmetry, all other arrangements, including the dislocation line sense, are equivalent to these. Therefore, the configuration shown in Fig. 16(b) can be

described as *ED*/*Edge*/*Up* (edge dislocation approaching an edge of the SFT with apex up) or *SD*/*Edge*/*Up* in the case of a screw dislocation. Two other important parameters are the SFT height, H, and the distance, h, between the SFT base and dislocation slip plane: these are expressed in units of the spacing ($a_0/\sqrt{3}$) between {1 1 1} planes (see Ref. [176] for explanation). In this notation the total number of vacancies, N_v, in a regular SFT is $H(H+1)/2$. For example, if an edge dislocation intersects an SFT of 36 vacancies ($H = 8$) through its geometrical centre ($h = 4$) this is denoted as *ED*/*Edge*/*Up*/*4*/*8*. Other important parameters such as T and $\dot{\varepsilon}$ or $\dot{\tau}$ are also indicated in the notation below.

R1: shear followed by complete restoration. In this, the SFT is sheared and ledges are formed on two faces. Fig. 51 shows the reaction (*SD*/*Face*/*11*/*16*, 100 K, 2.5 MPa ps^{-1}) for Cu. As emphasised in Section 5.3, conditions for this are that the dislocation intersects the SFT close to its apex, i.e. $h/H > 0.5$, and low T and high v_D. This reaction has a low τ_c.

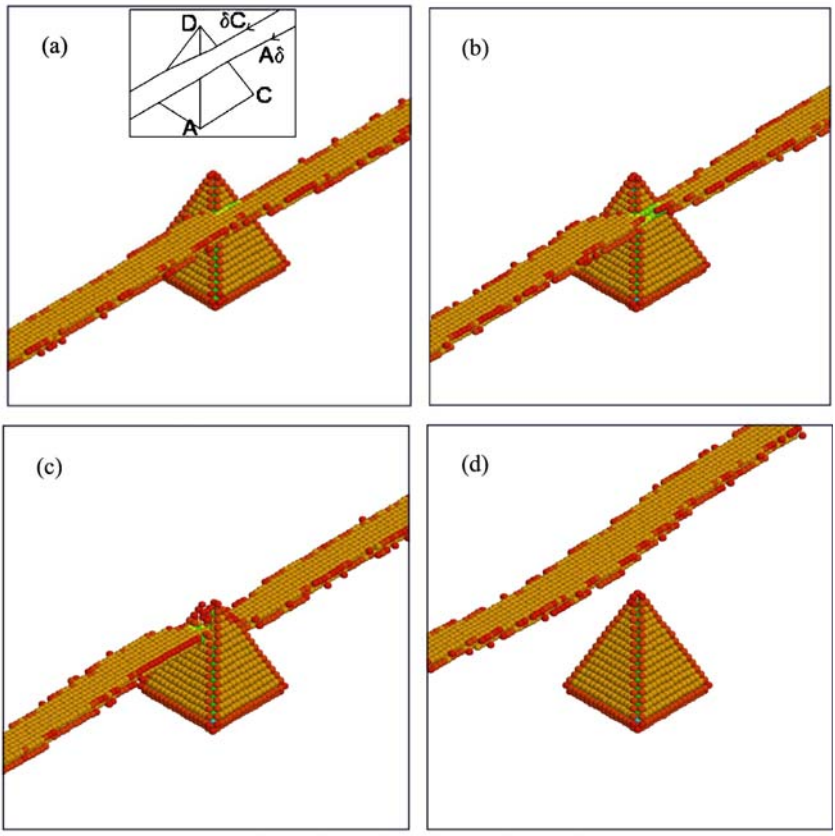

Fig. 51. Shear of a SFT by a screw dislocation, followed by full restoration (reaction R1). (Reprinted from Ref. [176] with permission from Taylor & Francis Ltd., http://www.informaworld.com.)

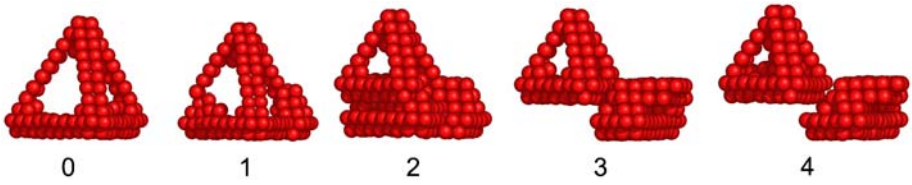

Fig. 52. Shear of an SFT by an edge dislocation, followed by creation of stable ledges (reaction R2). Numbers indicate the number of dislocation passes through the simulation cell. (From Ref. [195].)

R2: shear with permanent damage. Here, the SFT is sheared by the gliding dislocation and two stable ledges are formed on its faces, sometimes accompanied by removal of one or more vacancies from an apex to an edge. This and other examples can be found in Ref. [176]. When an SFT with stable ledges is sheared by multiple dislocations, two situations arise: either the damage accumulates and the SFT is progressively sheared, or the ledges become unstable and the SFT is restored to its initial configuration. The former process is illustrated in Fig. 52 for the case (*ED*/*Up*/*6*/*12*, 300 K, $2 \times 10^7\,s^{-1}$) in Cu when the dislocation passes through the simulation cell four times and separates apex and base parts. (Atoms in the stacking faults are omitted for clarity.)

R3: partial absorption into edge dislocation. This is observed only for *ED*/*Down* and is favoured by high T, small h/H and large H, though the minimum H at which it occurs depends on the interatomic potential [176]. The reaction is illustrated in Fig. 53 by (*ED*/*Down*/*6*/*12,* 450 K, $2 \times 10^7\,s^{-1}$) in Cu, where the insets show the Burgers vectors involved. The **δA** Shockley partial of the edge dislocation comes into contact with the face of the SFT in (a), soon followed in (b) by the **Cδ** partial. The **δA** partial slips through the SFT, while the **Cδ** partial reacts with the **αβ** stair-rod partial edge of the SFT in (c). Finally, the dislocation detaches from the SFT with the formation of a pair of superjogs that are clearly visible in (d). The jogs inherit the initial shape of the SFT, with the consequence that one lies in a {1 1 1} plane and is glissile, while the other is in a {1 0 0} plane and is a constricted segment of a Lomer dislocation having a low mobility. Further motion of the dislocation creates small vacancy clusters visible in (d). The corresponding interstitials are absorbed in the sessile jog to enable it to change shape and plane and become glissile.

R4: temporary absorption of part of the SFT as a helix on a screw dislocation. This is seen only for the *SD*/*Face* arrangement. This configuration was first considered by Kimura and Maddin [200], who proposed a mechanism based on cross-slip of the screw dislocation on an SFT face that could lead to complete absorption of the SFT by formation of a helical turn. Simulation has now confirmed this mechanism in general although complete absorption has not been seen in MD simulations. It is illustrated in Fig. 54 by the case (*SD*/*Face*/*7*/*16*, 100 K, 2.5 MPa ps^{-1}) for Cu. When the leading partial comes into contact with the SFT face in (a), the dislocation spontaneously constricts. It then cross-slips and dissociates in the SFT face into partials **βC** and **βA**. The latter sweeps over the part of the SFT face below the glide plane and removes the stacking fault in this region, whereas the **βC** partial remains

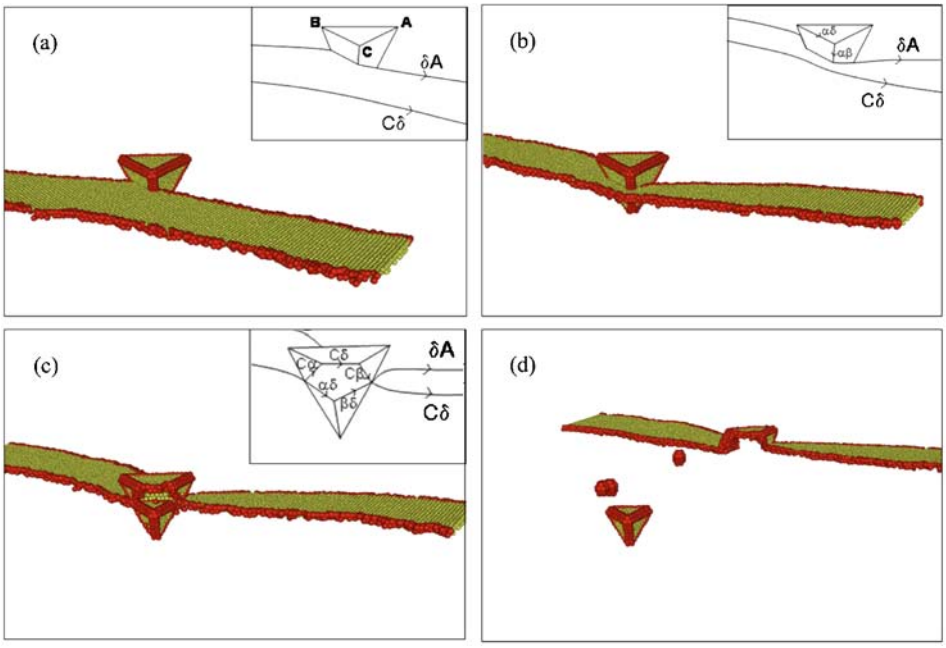

Fig. 53. Partial absorption of an SFT into an edge dislocation (reaction R3). (Reprinted from Ref. [176] with permission from Taylor & Francis Ltd., http://www.informaworld.com.)

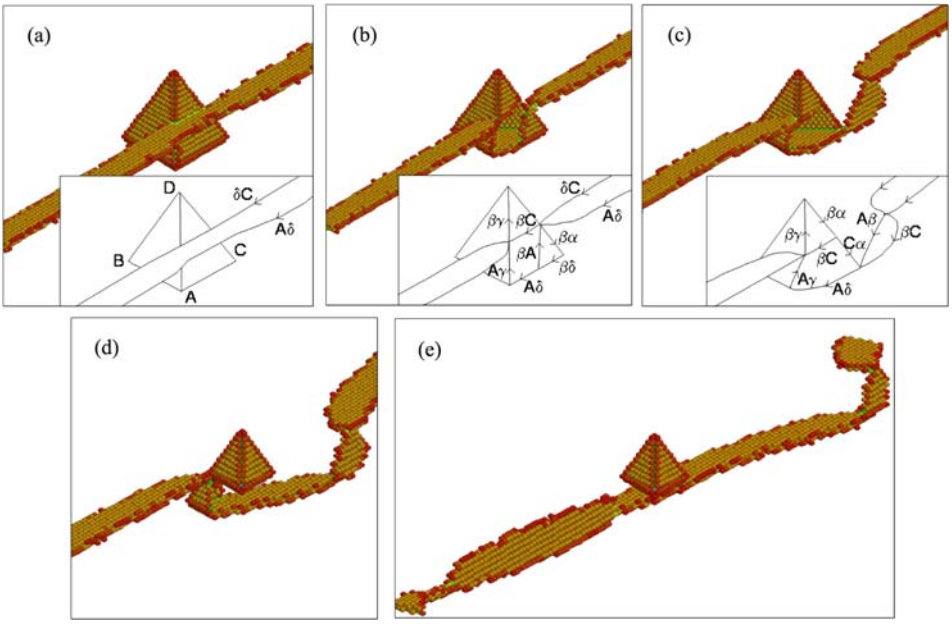

Fig. 54. Partial absorption of an SFT into a screw dislocation (reaction R4). (Reprinted from Ref. [176] with permission from Taylor & Francis Ltd., http://www.informaworld.com.)

immobile (see (b)). The **βA** partial then combines with the **βα** stair-rod on the right-hand side of the SFT and forms an **Aα** Frank partial. This high-energy partial is unstable and dissociates into dislocations with Burgers vectors **AC** and **Cα**. The **AC** segment is a cross-slipped segment of the initial screw that moves away from the SFT on the right-hand side, as shown in (c) and (d). On the other side of the SFT, the screw dislocation cuts the SFT, forming a new stacking fault on the cut plane and thereby recreating a smaller tetrahedron. Thus, the screw absorbs part of the SFT in a helical turn dissociated in several {1 1 1} planes, as seen in (e).

This mechanism has two differences from the one proposed in Ref. [200]. First, the authors supposed that both the **βC** and **βA** cross-slipped partials would sweep the whole face of the SFT and fully remove the fault, while in simulation only one partial is mobile and unfaults only the base part of the SFT. Second, it was also assumed that the **Aα** Frank partial would remain constricted, whereas it decomposes and forms a cross-slipped segment for the screw dislocation that leaves the SFT and forms the helical turn.

As noted earlier, a helical turn is an obstacle for a gliding screw dislocation and unpinning requires the dislocation to bow out and force the turn to close onto itself. When the dislocation unpins, the vacancies that formed the turn are left as a vacancy cluster, separated from the remaining SFT along the **AC** direction by a distance that depends on the helix size and dislocation velocity. Examples are provided in Fig. 4 of Ref. [176].

5.5.2. *Other cases*

The wide range of interaction mechanisms and their dependence on T and SFT orientation and size complicates prediction of strengthening due to these obstacles. First, τ_c depends strongly on the interaction geometry. An example is provided by an edge dislocation cutting a 4.2 nm SFT at different levels, h. The interaction mechanism varies between R4, R2 and R1, and results in a large variation in τ_c, as seen in Fig. 55(a). Second, the picture is complicated by the effect of T. For some geometries, the reaction mechanism does not change and τ_c decreases with increasing T. This is shown in Fig. 55(b) for a 4.2 nm SFT in configuration *ED*/*Up* with $h/H = 0.5$. When the SFT orientation is inverted to apex-down, the reaction type is R1 at 0 and 100 K, R2 at 300 K and R3 at 450 K, resulting in the variation of τ_c with T shown in the figure.

Regardless of the complexity, dislocation–SFT interactions provide a situation where atomic-scale modelling can be related directly to experiment. Dislocation–SFT interactions have been investigated by *in situ* straining in a TEM, e.g. Refs [199, 202–206]. The reactions observed can be separated loosely into three types. The first occurs when a dislocation passes through an SFT without visible change of either defect, i.e. reaction R1. In the second, a dislocation cross-slips and the base portion of the SFT disappears, leaving a smaller defect. The third type is seen when a dislocation undergoes extensive cross-slip in the vicinity of the SFT, ultimately creating a superjog which persists until the experiment is terminated. The second and third types are similar to reaction R4, with the difference that in simulation the base part of the SFT is released back as a vacancy cluster in the vicinity of the

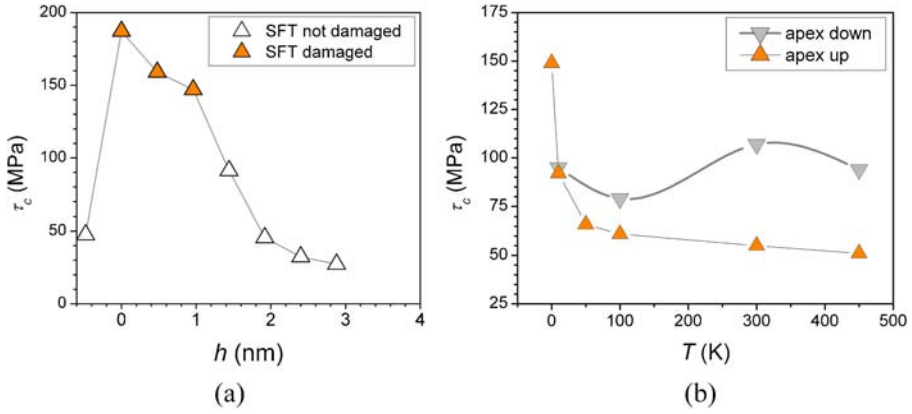

Fig. 55. Variation of τ_c for an edge dislocation crossing a 4.2 nm SFT ($\dot{\varepsilon} = 5 \times 10^7\ s^{-1}$) as a function of (a) distance between the edge dislocation glide plane and the SFT base [195] and (b) temperature [201]. In (a) the SFT apex is oriented up and in (b) cases of apex up and down are both shown.

original SFT. The reason for this difference is that a computational model with periodic boundary conditions along the dislocation line imposes conservation of the total number of vacancies. Thus, in order to reproduce experimental thin-foil conditions, Osetsky et al. [198] modelled a screw dislocation, 50–80 nm long, with free surfaces perpendicular to the line (x-faces in Fig. 16(b)). They found that a fast mass transport effect to a surface occurs due to superjog glide, leading to the elimination of a large number of vacancies and the disappearance of the base part of the SFT.

Fig. 56 shows a time sequence of this process for an SFT containing 820 vacancies, $H = 8.3$ nm, $h = 6.1$ nm and $\dot{\varepsilon} = 10^7\ s^{-1}$, $T = 300$ K and $L = 50$ nm. Figs 56(a) and (b) show how the screw dislocation initially cross-slips in the SFT face and removes the part of the stacking fault between its glide plane and the SFT base. The right-hand segment then cross-slips back and is restored to its original glide plane (see (c)). The left-hand segment with mixed character in (c) achieves pure screw orientation in (d) on the plane coincident with the SFT upper face by annihilation of its edge component at the left-hand surface. This process represents vacancy transport to that surface of the simulation cell. The dislocation now contains a glissile edge superjog of height h. The left screw segment continues to bend under the applied stress, forcing the superjog to glide towards the right-hand surface, as in (e), where it disappears, as shown in (f). The screw dislocation is now restored, but on a plane h above its original slip plane, and glides away. In agreement with the experiments, most of the vacancies of the SFT (765 out of 820) are transferred to the surfaces, with the creation of surface steps, and a much smaller SFT (of 55 vacancies) remains at the tip of the original one. This mass transport occurred over a time of only 0.7 ns. The critical stress was 100 MPa, smaller than the value 170 MPa for an R1 reaction with the same dislocation length. The mechanism in Fig. 56 has variations depending on the position of the SFT relative to free surfaces, L, H and h, T and $\dot{\varepsilon}$ [198].

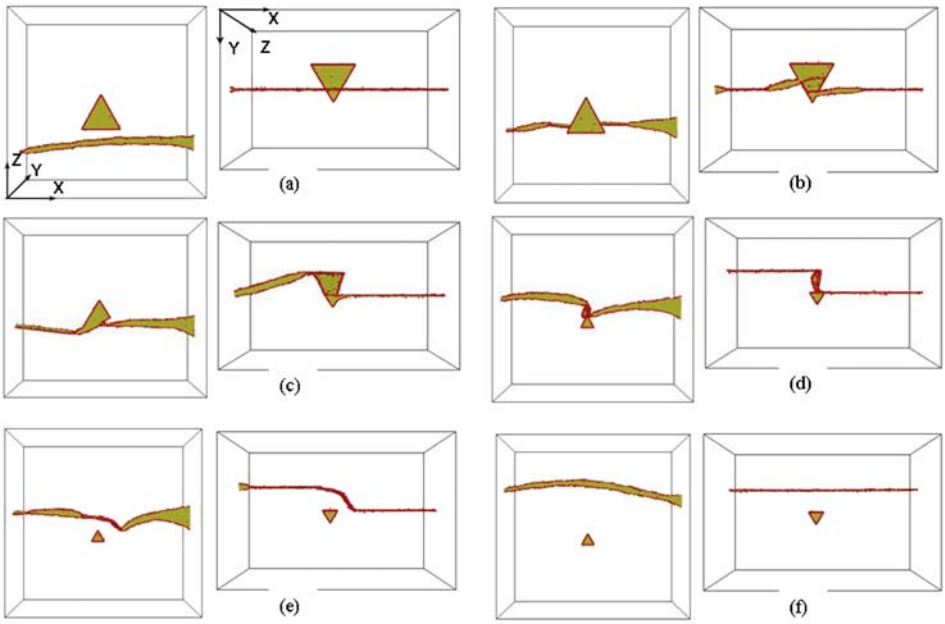

Fig. 56. Sequence of configurations during interaction of a screw dislocation with a 10.2 nm SFT ($L_x = 50$ nm, $T = 300$ K and $\dot{\varepsilon} = 10^7$ s^{-1}). The left-hand image in each pair is a plan view of the (1 1 1) slip plane; the right-hand image is a [1 $\bar{1}$ 0] view with the slip plane edge-on. The free x-surfaces are the left and right faces. (Reprinted from Ref. [198] with permission from Taylor & Francis Ltd., http://www.informaworld.com.)

5.6. Conclusions

The MD simulations described above have assisted in understanding reactions where obstacles have dislocation character. The possibility for screw segments to cross-slip is a key feature of some mechanisms. It allows for loop and SFT unfaulting and is systematically involved in the creation of helices on dislocation lines that can absorb, either partially or completely, obstacles and/or modify their structure (e.g. Burgers vector change). Such reactions are therefore sensitive to both T and stacking fault energy, γ, in that the probability of cross-slip decreases with decreasing T and γ. Strain- and stress-rates are also important since lower rates allow the dislocation to remain for a longer time in contact with the defect, which increases the probability of cross-slip. MD simulations have also shown that temperature and deformation rate can change the interaction mechanism itself, an effect previously unforeseen.

The mobility of helices along a dislocation is a significant mechanism for fragmenting obstacles and transferring point defects over relatively long distances. These effects have not been considered to date in DD continuum modelling. The same comment can also be applied to climb of edge dislocations by superjog formation,

which has been shown here to be able to remove a significant fraction of dislocation obstacles. Climb is more effective for loops and SFTs than for voids and precipitates (Section 4), for which only a few defects are absorbed by a single dislocation.

The ability of atomic-scale simulation to reveal new mechanisms and provide interpretation of experimental observations has been demonstrated in Section 5.5.2 by the example of *in situ* TEM deformation. It is now clear that some reaction mechanisms that occur in thin films are specific to the conditions and cannot be applied for bulk materials.

Finally, the dislocation obstacles considered here offer good examples where atomic-scale modelling can interact productively with DD modelling by providing details of mechanisms and quantification of their parameters. The integration of atomic and continuum treatments is a requirement for the development of a true multiscale materials modelling approach to the effects of microstructure on mechanical properties. This has been done recently for Frank loops [22] but simulations involving all the details of the interaction mechanisms remain computationally expensive and more investigations are required on these issues.

6. Concluding remarks

Significant progress in applying atomic-scale simulation to problems of practical importance has been made over the past decade because of three factors. First, on the hardware side the dramatic increase of computing power per unit of investment has allowed simulation of much larger models and also provided researchers with facility to easily visualise the collective behaviour of hundreds or even thousands of atoms. Second, computer codes have been improved by the development of boundary conditions suitable for dislocations of different type and techniques for simulating external loading, and this has led to more realistic modelling. Third, many new interatomic potentials have been produced with the use of *ab initio* data, and this development has increased confidence in the results of simulation.

As a result of these changes, MD and MS simulations can now be performed for obstacle microstructures with realistic length scale, defect size and dislocation density. We have shown that the parameters of current computer models are well suited to replication of microstructure created by radiation damage, which is characterised by a high density of nanometre-sized defects. Furthermore, atomic-scale simulations are now compatible with the scales of *in situ* deformation in a TEM, and so provide comparison between modelling and experiment, despite the short timescale in the former and resolution limit in the latter.

The research reviewed here provides a broad view of individual dislocation interaction with obstacles. Atomic-scale mechanisms such as absorption of defects by edge dislocations that acquire superjogs, the formation of helical turns on screw dislocations with subsequent long-range mass transfer along dislocation lines, and cross-slip of screw dislocations (or screw parts on bowed edge dislocations) are key features of most interaction processes. The results obtained to date are sufficiently extensive for us to have attempted a qualitative categorisation based on similarities

between the effects of different obstacles. These are most apparent for obstacles with dislocation character, i.e. perfect dislocation loops in FCC and BCC metals, and faulted Frank loops and SFTs in FCC metals. (Although we have not discussed them, effects such as loop absorption and transformation have also been found in the few simulations that have been reported for the HCP structure [55,56].) The similarities across crystal structures and defect types are consistent with changes observed in all metals due to radiation damage, for phenomena such as hardening, embrittlement and clear band formation are common. It is particularly encouraging that the well-established concepts of dislocation theory, based on linear elasticity, offer a valid interpretation of many of the effects observed for nanoscale obstacles, particularly with regard to the use of Frank's rule for reaction between parallel dislocations and the influence of dislocation self-stress. This provides direct validation of continuum DD simulations that use algorithms based on these concepts. The same conclusion has been made as a result of simulation of junction formation between pairs of interacting dislocations [207–209].

There are still significant problems, however, that limit successful application of atomic-scale techniques.

- *Interatomic potentials*. The realism of large-scale atomic simulations is dependent on the validity of interatomic potentials, which have to be short-ranged for computational efficiency and reproduce interactions between atoms in configurations far from perfect. Validity remains limited for many metals. Potentials for relatively simple metals are perhaps reliable, but those for transition metals, where electronic effects in bonding and magnetism are strong, are more problematic. Confidence in the simulated core structure of dislocations in some FCC metals is high, but the core of screw dislocations in BCC transition metals is hard to reproduce and the situation for HCP metals, in which the energy and stability of stacking faults on the basal and prism planes determines dislocation behaviour, is no better. The development of potentials for alloys, where it is important to replicate local chemistry and thermodynamic properties, is also at an early stage. Thus, it is wise to remember that most current potentials provide models that have some of the properties of the real metals in question, such as crystal structure, elastic constants, point defect energies, etc., but not all. By carrying out simulations with different potentials for the same metal, potential-specific peculiarities may be identified.
- *Timescale*. This is possibly the most serious limitation of investigations based on MD. Even with large supercomputers, the timescale accessible to MD simulation remains several orders of magnitude lower than that experienced in experiments, and this restricts the ability to study thermally activated processes. We have demonstrated that MD simulations reproduce thermal effects, such as a decrease of obstacle strength as T increases and an increase in the occurrence of cross-slip reactions when T increases and/or dislocation velocity decreases, i.e. when the strain rate decreases. Nevertheless, thermally activated dislocation processes that can be observed in MD simulations have activation enthalpies smaller than 0.1 eV and most of the energy to overcome an obstacle is provided by the applied stress.

- *Length scale*. Despite clear successes in using atomic-scale models to study interactions between individual dislocations and small obstacles under a variety of loading conditions, the creation of computational approaches capable of predicting mechanical behaviour due to microstructure changes resulting from thermal or irradiation treatments is still a severe challenge. It demands not only atomic-level data based on longer times, but also knowledge of effects that operate over longer length scales. Examples include statistical effects of obstacle populations; cooperative dislocation effects such as pile-ups; mechanisms that affect the operation and blocking of dislocation sources; the influence of intergrain and interphase boundaries on dislocation motion; and the role of these boundaries in acting as sources and sinks for dislocations and other defects.

We conclude that while application of massively parallelised, scalable models in the near future may increase times and lengths, and reduce strain rates, by a few orders of magnitude, atomic-level simulation of millisecond and millimetre scales will not be achievable. Developments such as more efficient algorithms for accelerated dynamics and saddle-point search methods to give access to thermally activated processes compatible with experiment will help, but not solve, the problem. To exploit the power of atomic simulation, it will still be necessary to link it to continuum-based DD modelling by using MD simulation to generate the local rules that describe dislocation–obstacle interaction. This provides the route to study the effects mentioned in the previous paragraph. Although the variety of mechanisms already revealed by MD is large, we have seen that it should be possible to categorise them in such a way that they can be imported into DD codes.

Acknowledgements

Much of the work described in this chapter was carried out with support of grants from a variety of sources, including grants GR/N23189/01, GR/R68870/01 and GR/S81162/01 from the UK Engineering and Physical Sciences Research Council; grant F160-CT-2003-508840 ('PERFECT') under programme EURATOM FP-6 of the European Commission; and the Division of Materials Sciences and Engineering and the Office of Fusion Energy Sciences, U.S. Department of Energy, under contract with UT-Battelle, LLC. The authors thank Prof. Y. Bréchet, and Drs. G. Martin, Y. Mastukawa, R.E. Stoller and S.J. Zinkle for many fruitful discussions on theoretical modelling and experimental results, and Drs. T. Nogaret and D. Terentyev for their contributions to dislocation-loop simulations.

References

[1] V.V. Bulatov, W. Cai, Computer Simulations of Dislocations, Oxford University Press, Oxford, 2006.
[2] D. Hull, D.J. Bacon, Introduction to Dislocations, Butterworth-Heinemann, Oxford, 2001.
[3] J.P. Hirth, J. Lothe, Theory of Dislocations, Krieger Publishing Company, 1982.

[4] F.R.N. Nabarro, Theory of Crystal Dislocations, Oxford University Press, Oxford, 1967.
[5] V. Vitek, V. Paidar, in: J.P. Hirth (Ed.), Dislocations in Solids, vol. 14, Elsevier, Amsterdam, 2008, p. 439.
[6] W. Cai, V.V. Bulatov, J. Chang, J. Li, S. Yip, in: F.R.N. Nabarro, J.P. Hirth (Eds.), Dislocations in Solids, vol. 12, Elsevier, Amsterdam, 2004, p. 1.
[7] H. Swygenhoven, P.M. Derlet, in: J.P. Hirth (Ed.), Dislocations in Solids, vol. 14, Elsevier, Amsterdam, 2008, p. 1.
[8] M. Finnis, Interatomic Forces in Condensed Matter, Oxford University Press, Oxford, 2003.
[9] M.S. Daw, M.I. Baskes, Phys. Rev. B 29 (1984) 6443.
[10] M.P. Allen, D.J. Tildesley, Computer Simulation of Liquids, Oxford University Press, Oxford, 1987.
[11] G.S. Was, Fundamentals of Radiation Materials Science, Springer, Berlin, 2007.
[12] D.J. Bacon, Y.N. Osetsky, R. Stoller, R.E. Voskoboinikov, J. Nucl. Mater. 323 (2003) 152.
[13] Y.N. Osetsky, D.J. Bacon, A. Serra, B.N. Singh, S.I. Golubov, J. Nucl. Mater. 276 (2000) 65.
[14] Y.N. Osetsky, A. Serra, B.N. Singh, S.I. Golubov, Philos. Mag. A 80 (2000) 2131.
[15] N. De Diego, Y.N. Osetsky, D.J. Bacon, J. Nucl. Mater. 374 (2008) 87.
[16] J.V. Sharp, Philos. Mag. 16 (1967) 77.
[17] F. Onimus, I. Monnet, J.L. Bechade, C. Prioul, P. Pilvin, J. Nucl. Mater. 328 (2004) 165.
[18] M. Victoria, N. Baluc, C. Bailat, Y. Dai, M.I. Luppo, R. Schaublin, B.N. Singh, J. Nucl. Mater. 276 (2000) 114.
[19] B.N. Singh, A. Horsewell, P. Toft, J. Nucl. Mater. 272 (1999) 97.
[20] B.N. Singh, A. Horsewell, P. Toft, D.J. Edwards, J. Nucl. Mater. 224 (1995) 131.
[21] S.J. Zinkle, B.N. Singh, J. Nucl. Mater. 351 (2006) 269.
[22] T. Nogaret, D. Rodney, M. Fivel, C. Robertson, J. Nucl. Mater. 380 (2008) 22.
[23] H.B. Huntington, J.E. Dickey, R. Thomson, Phys. Rev. 100 (1955) 1117.
[24] R.M. Cotterill, M. Doyama, Phys. Rev. 145 (1966) 465.
[25] R. Chang, L.J. Graham, Phys. Status Solidi 18 (1966) 99.
[26] V. Vitek, R.C. Perrin, D.K. Bowen, Philos. Mag. 21 (1970) 1049.
[27] J. Schiffgens, K.E. Garrison, J. Appl. Phys. 43 (1972) 3240.
[28] R.C. Perrin, A. Englert, R. Bullough, in: P.C. Gehlen, J.R. Beeler, R.I. Jaffee (Eds.), Interatomic Potentials and Simulation of Lattice Defects, Plenum Press, New York, 1972, p. 509.
[29] V. Vitek, Cryst. Latt. Defects 5 (1974) 1.
[30] M.S. Duesbery, V. Vitek, D.K. Bowen, Proc. R. Soc. Lond. A 332 (1973) 85.
[31] S. Rao, C. Hernandez, J.P. Simmons, T.A. Parthasarathy, C. Woodward, Philos. Mag. A 77 (1998) 231.
[32] V.B. Shenoy, R. Phillips, Philos. Mag. A 76 (1997) 367.
[33] J.E. Sinclair, P.C. Gehlen, R.G. Hoagland, J.P. Hirth, J. Appl. Phys. 49 (1978) 3890.
[34] R. Thomson, S.J. Zhou, A.E. Carlsson, V.K. Tewary, Phys. Rev. 46 (1992) 10613.
[35] S.I. Golubov, X. Liu, H. Huang, C.H. Woo, Comput. Phys. Commun. 137 (2001) 312.
[36] D.G. Pettifor, M. Aoki, Philos. Trans. R. Soc. Lond. A 334 (1991) 439.
[37] J.A. Moriarty, V. Vitek, V.V. Bulatov, S. Yip, J. Comput. Aided Mater. Des. 9 (2002) 99.
[38] C. Woodward, S.I. Rao, Phys. Rev. Lett. 88 (2002) 216402.
[39] M.S. Daw, S.M. Foiles, M.I. Baskes, Mater. Sci. Rep. 9 (1993) 251.
[40] R.C. Pond, J.P. Hirth, Solid State Phys. 47 (1994) 287.
[41] A. Serra, D.J. Bacon, Y.N. Osetsky, Philos. Mag. Lett. 87 (2007) 451.
[42] Y.N. Osetsky, D.J. Bacon, Modell. Simul. Mater. Sci. Eng. 11 (2003) 427.
[43] C. Domain, G. Monnet, Phys. Rev. Lett. 95 (2005) 215506.
[44] J. Chaussidon, M. Fivel, D. Rodney, Acta Mater. 54 (2006) 3407.
[45] D. Rodney, Acta Mater. 52 (2004) 607.
[46] T. Nogaret, C. Robertson, D. Rodney, Philos. Mag. 87 (2007) 945.
[47] H.J. Lee, J.H. Shim, B.D. Wirth, J. Mater. Res. 22 (2007) 2758.
[48] L. Saintoyant, H.J. Lee, B.D. Wirth, J. Nucl. Mater. 361 (2007) 206.
[49] B.D. Wirth, V.V. Bulatov, T.D. De La Rubia, J. Eng. Mater. Technol. 124 (2002) 329.

[50] J. Marian, W. Cai, V.V. Bulatov, Nat. Mater. 3 (2004) 158.
[51] D. Rodney, G. Martin, Phys. Rev. B 61 (2000) 8714.
[52] E. Bitzek, P. Gumbsch, Mater. Sci. Eng. A 400–401 (2005) 40.
[53] D. Rodney, Phys. Rev. B 76 (2007) 144108.
[54] Y.N. Osetsky, S.I. Golubov (unpublished).
[55] R.E. Voskoboinikov, Y.N. Osetsky, D.J. Bacon, Mater. Sci. Eng. A 400 (2005) 49.
[56] R.E. Voskoboynikov, Y.N. Osetsky, D.J. Bacon, Mater. Sci. Eng. A 400 (2005) 54.
[57] D. Terentyev, P. Grammatikopoulos, D.J. Bacon, Y.N. Osetsky, Acta Mater. 56 (2008) 5034.
[58] J.D. Honeycutt, H.C. Andersen, J. Phys. Chem. 91 (1987) 4950.
[59] J.C. Gil Montoro, J.L.F. Abascal, J. Phys. Chem. 97 (1993) 4211.
[60] P. Guyot, J.E. Dorn, Can. J. Phys. 45 (1967) 983.
[61] V. Vitek, Prog. Mater Sci. 36 (1992) 1.
[62] C. Domain, J. Nucl. Mater. 351 (2006) 1.
[63] S.L. Frederiksen, K.W. Jacobsen, Philos. Mag. 83 (2003) 365.
[64] P.B. Hirsch, Proceedings of the 5th International Conference on Crystallography, Cambridge University Press, Cambridge, 1960, p. 139.
[65] L. Kubin, Rev. Deform. Behav. Mater. 244 (1977) 1.
[66] H. Alexander, in: F.R.N. Nabarro (Ed.), Dislocations in Solids, vol. 7, Elsevier, Amsterdam, 1986, p. 113.
[67] D. Terentyev, D.J. Bacon, Y.N. Osetsky, J. Phys. Condens. Matter 20 (2008) 445007.
[68] H. Khater, Ph.D. thesis, University of Liverpool, 2008.
[69] G.J. Ackland, D.J. Bacon, A.F. Calder, T. Harry, Philos. Mag. A 75 (1997) 713.
[70] G.J. Ackland, M.I. Mendelev, D.J. Srolovitz, S. Han, A.V. Barashev, J. Phys. Condens. Matter. 16 (2004) S2629.
[71] G.J. Ackland, S.J. Wooding, D.J. Bacon, Philos. Mag. A 71 (1995) 553.
[72] M.I. Mendelev, G.J. Ackland, Philos. Mag. Lett. 87 (2007) 349.
[73] S. Takeuchi, Philos. Mag. A 39 (1979) 661.
[74] J.L. Bassani, K. Ito, V. Vitek, Mater. Sci. Eng. A 319 (2001) 97.
[75] V.I. Alshits, V.L. Indenbom, in: F.R.N. Nabarro, J.P. Hirth (Eds.), Dislocations in Solids, vol. 7, Elsevier, Amsterdam, 1986, p. 43.
[76] D. Rodney, G. Martin, Phys. Rev. Lett. 82 (1999) 3272.
[77] Z. Rong, Y.N. Osetsky, D.J. Bacon, Philo. Mag. 85 (2005) 1473.
[78] D.L. Olmsted, L.G. Hector, W.A. Curtin, R.J. Clifton, Modell. Simul. Mater. Sci. Eng. 13 (2005) 371.
[79] A. Seeger, Philos. Mag. 1 (1956) 651.
[80] J. Friedel, Dislocations, Pergamon Press, New York, 1964.
[81] G. Henkelman, H. Jonsson, J. Chem. Phys. 111 (1999) 7010.
[82] D. Brunner, J. Diehl, Phys. Status Solidi A 124 (1991) 455.
[83] M. Tang, L.P. Kubin, G.R. Canova, Acta Mater. 46 (1998) 3221.
[84] Y. Aono, K. Kitajima, E. Kuramoto, Scripta Metall. 15 (1981) 275.
[85] Z.S. Basinski, M.S. Duesbery, G.S. Murty, Acta Metall. 29 (1981) 801.
[86] M. Wen, A.H.W. Ngan, Acta Mater. 48 (2000) 4255.
[87] R. Groger, V. Vitek, Philos. Mag. Lett. 87 (2007) 113.
[88] A.S. Argon, Strengthening Mechanisms in Crystal Plasticity, Oxford University Press, Oxford, 2008.
[89] J.W. Martin, Micromechanisms in Particle-Hardened Alloys, Cambridge University Press, Cambridge, 1980.
[90] A.J.E. Foreman, M.J. Makin, Philos. Mag. 14 (1966) 911.
[91] U.F. Kocks, Can. J. Phys. 45 (1967) 737.
[92] K. Hanson, J.W. Morris, J. Appl. Phys. 46 (1975) 983.
[93] R. Labusch, J. Appl. Phys. 48 (1977) 4550.
[94] M. Zaiser, Philos. Mag. A 82 (2002) 2869.
[95] M. Hiratani, V.V. Bulatov, Philos. Mag. Lett. 84 (2004) 461.

[96] P. Haasen, in: F.R.N. Nabarro, J.P. Hirth (Eds.), Dislocations in Solids, vol. 4, Elsevier, Amsterdam, 1979, p. 155.
[97] D.R. Trinkle, C. Woodward, Science 310 (2005) 1665.
[98] E. Rodary, D. Rodney, L. Proville, Y. Brechet, G. Martin, Phys. Rev. B 70 (2004) 054111.
[99] K. Tapasa, D.J. Bacon, Y.N. Osetsky, Modell. Simul. Mater. Sci. Eng. 14 (2006) 1153.
[100] L. Proville, D. Rodney, Y. Brechet, G. Martin, Philos. Mag. 86 (2006) 3893.
[101] S. Patinet, L. Proville, Phys. Rev. B 78 (2008) 104109.
[102] R.W. Cahn, Nature 410 (2001) 643.
[103] D.L. Olmsted, L.G. Hector, W.A. Curtin, J. Mech. Phys. Sol. 54 (2006) 1763.
[104] T.H. Wille, W. Gieseke, C.H. Schwink, Acta Metall. 25 (1987) 2679.
[105] A.H. Cottrell, B.A. Bilby, Phys. Soc. Lond. A 62 (1949) 49.
[106] K. Tapasa, A.V. Barashev, D.J. Bacon, Y.N. Osetsky, Acta Mater. 55 (2007) 1.
[107] R.A. Johnson, G.J. Dienes, A.C. Damask, Acta Metall. 12 (1964) 1215.
[108] J.P. Hirth, M. Cohen, Scripta Metall. 3 (1969) 107.
[109] J.P. Hirth, M. Cohen, Scripta Metall. 3 (1969) 311.
[110] G. Schoeck, Scripta Metall. 3 (1969) 239.
[111] D.J. Bacon, Scripta Metall. 3 (1969) 735.
[112] C.S. Becquart, J.M. Raulot, G. Bencteux, C. Domain, M. Perez, S. Garruchet, H. Nguyen, Comput. Mater. Sci. 40 (2007) 119.
[113] R.E. Reed-Hill, R. Abbaschian, Physical Metallurgy Principles, PWS Publishing Company, Boston, MA, 1991.
[114] U.F. Kocks, A.S. Argon, M.F. Ashby, Thermodynamics and Kinetics of Slip, Prog. Mater. Sci. 19 (1975) (Pergamon, Oxford).
[115] R.O. Scattergood, D.J. Bacon, Acta Metall. 30 (1982) 1665.
[116] Y.N. Osetsky, D.J. Bacon, V. Mohles, Philos. Mag. 83 (2003) 3623.
[117] Y.N. Osetsky, D.J. Bacon, J. Nucl. Mater. 323 (2003) 268.
[118] D.J. Bacon, Y.N. Osetsky, JOM 59 (2007) 42.
[119] D.J. Bacon, Y.N. Osetsky, J. Math. Mech. Sol. 14 (2009) 270.
[120] Y.N. Osetsky, D.J. Bacon (unpublished).
[121] G.J. Ackland, G.I. Tichy, V. Vitek, M.W. Finnis, Philos. Mag. A 56 (1987) 735.
[122] D.J. Bacon, Y.N. Osetsky, Mater. Sci. Eng. A 400 (2005) 353.
[123] R. Monzen, M.L. Jenkins, A.P. Sutton, Philos. Mag. A 80 (2000) 711.
[124] J.T. Buswell, C.A. English, M.G. Hetherington, W.J. Phythian, G.D.W. Smith, G.M. Worral, Effects of Radiation on Materials: 14th International Symposium ASTM STP 1046, vol. II, ASTM, Philadelphia, PA, 1990, p. 127.
[125] R.G. Carter, N. Soneda, K. Dohi, J.M. Hyde, C.A. English, W.L. Server, J. Nucl. Mater. 298 (2001) 211.
[126] R. Chaouadi, R. Gerard, J. Nucl. Mater. 345 (2005) 65.
[127] D.J. Bacon, Y.N. Osetsky, J. Nucl. Mater. 329–333 (2004) 1233.
[128] Y.N. Osetsky, D.J. Bacon, in: H. Kitagawa, Y. Shibutani (Eds.), IUTAM Symposium on Mesoscopic Dynamics of Fracture Process and Materials Strength, Kluwer Academic Publishers, Dordrecht, 2004, p. 193.
[129] Y.N. Osetsky, D.J. Bacon, Mater. Sci. Eng. A 400 (2005) 374.
[130] T. Harry, D.J. Bacon, Acta Mater. 50 (2002) 195.
[131] T. Harry, D.J. Bacon, Acta Mater. 50 (2002) 209.
[132] K.C. Russell, L.M. Brown, Acta Metall. 20 (1972) 969.
[133] D.J. Bacon, U.F. Kocks, R.O. Scattergood, Philos. Mag. 28 (1973) 1241.
[134] R.O. Scattergood, D.J. Bacon, Philos. Mag. 31 (1975) 179.
[135] D.J. Bacon, in: B.A. Bilby, K.J. Miller, J.R. Willis (Eds.), Fundamentals of Deformation and Fracture, Cambridge University Press, Cambridge, 1985, p. 401.
[136] G. Monnet, Acta Mater. 55 (2007) 5081.
[137] R. Schaublin, N. Baluc, Nucl. Fusion 47 (2007) 1690.
[138] S.M. Hafez Haghighat, R. Schaublin, J. Comput. Aided Mater. Des. 14 (2007) 191.

[139] S.L. Dudarev, P.M. Derlet, J. Phys. Condens. Matter 17 (2005) 7097.
[140] T. Hatano, H. Matsui, Phys. Rev. 72 (2005) 094105.
[141] T. Hatano, T. Kaneko, Y. Abe, H. Matsui, Phys. Rev. 77 (2008) 064108.
[142] J.H. Shim, Y.W. Cho, S.C. Kwon, W.W. Kim, B.D. Wirth, Appl. Phys. Lett. 90 (2007) 021906.
[143] S. Lozano-Perez, M.L. Jenkins, J.M. Titchmarsh, Philos. Mag. Lett. 86 (2006) 367.
[144] K. Suganuma, H. Kayano, J. Nucl. Mater. 118 (1983) 234.
[145] M.H. Mathon, Y. De Carlan, G. Geoffroy, X. Averty, A. Alamo, C.H. De Novion, J. Nucl. Mater. 312 (2003) 236.
[146] A. Alamo, V. Lambard, X. Averty, M.H. Mathon, J. Nucl. Mater. 329–333 (2004) 333.
[147] D.A. Terentyev, G. Bonny, L. Malerba, Acta Mater. 56 (2008) 3229.
[148] P. Olsson, J. Wallenius, C. Domain, K. Nordlund, L. Malerba, Phys. Rev. B 72 (2005) 214119.
[149] P.M. Kelly, Int. Metall. Rev. 18 (1973).
[150] U. Lagerpusch, V. Mohles, E. Nembach, Mater. Sci. Eng. A 319–321 (2001) 176.
[151] P.B. Hirsch, F.J. Humphreys, in: A.S. Argon (Ed.), Physics of Strength and Plasticity, MIT Press, Boston, MA, 1969, p. 189.
[152] T. Hatano, Phys. Rev. 74 (2006) 020102(R).
[153] R. Schaublin, Y.L. Chiu, J. Nucl. Mater. 362 (2007) 152.
[154] M. Eldrup, B.N. Singh, J. Nucl. Mater. 323 (2003) 346.
[155] A.F. Calder, D.J. Bacon, J. Nucl. Mater. 207 (1993) 25.
[156] A.F. Calder, D.J. Bacon, A.V. Barashev, Y.N. Osetsky, Philos. Mag. Lett. 88 (2008) 43.
[157] M. Kiritani, H. Takata, J. Nucl. Mater. 69–70 (1978) 277.
[158] M. Suzuki, A. Sato, T. Mori, J. Nagakawa, N. Yamamoto, H. Shiraishi, Philos. Mag. A 65 (1992) 1309.
[159] L. Boulanger, F. Soisson, Y. Serruys, J. Nucl. Mater. 233–237 (1996) 1004.
[160] Y.N. Osetsky, A. Serra, M. Victoria, S.I. Golubov, V. Priego, Philos. Mag. A 79 (1999) 2259.
[161] Y.N. Osetsky, A. Serra, M. Victoria, S.I. Golubov, V. Priego, Philos. Mag. A 79 (1999) 2285.
[162] J. Silcox, P.B. Hirsch, Philos. Mag. 4 (1959) 72.
[163] M. Kiritani, J. Nucl. Mater. 216 (1994) 220.
[164] S. Kojima, Y. Satoh, H. Taok, I. Ishida, T. Yoshiie, M. Kiritani, Philos. Mag. A 59 (1999) 519.
[165] B.N. Singh, D.J. Edwards, P. Toft, J. Nucl. Mater. 299 (2001) 205.
[166] R.E. Voskoboinikov, Y.N. Osetsky, D.J. Bacon, J. Nucl. Mater. 377 (2008) 385.
[167] M. Kiritani, Y. Satoy, Y. Kizuka, K. Arakawa, Y. Ogasawara, S. Arai, Y. Shimomura, Philos. Mag. Lett. 79 (1999) 797.
[168] I.M. Robertson, M.L. Jenkins, C.A. English, J. Nucl. Mater. 108 (1982) 209.
[169] L.L. Horton, J. Bentley, K. Farrell, J. Nucl. Mater. 108 (1982) 222.
[170] B.C. Masters, Philos. Mag. 11 (1965) 881.
[171] E.A. Little, B.L. Eyre, J. Micros. 97 (1973) 107.
[172] S.L. Dudarev, R. Bullough, P.M. Derlet, Phys. Rev. Lett. 100 (2008) 135503.
[173] N.V. Doan, D. Rodney, G. Martin, Diffusions in Materials: DIMAT 2000, Pts. 1 & 2, 194–199, 2001, p. 43.
[174] Y.N. Osetsky, D.J. Bacon, A. Serra, B.N. Singh, S.I. Golubov, Philos. Mag. 83 (2003) 61.
[175] K. Arakawa, K. Ono, M. Isshiki, K. Mimura, M. Uchikoshi, H. Mori, Science 318 (2007) 956.
[176] Y.N. Osetsky, D. Rodney, D.J. Bacon, Philos. Mag. 86 (2006) 2295.
[177] M.J. Makin, Philos. Mag. 10 (1964) 695.
[178] L.P. Kubin, J. Kratochvil, Philos. Mag. A 80 (2000) 201.
[179] J.E. Angelo, N.R. Moody, M.I. Baskes, Modell. Simul. Mater. Sci. Eng. 3 (1995) 289.
[180] Y.N. Osetsky, D.J. Bacon, Z. Rong, B.N. Singh, Philos. Mag. Lett. 84 (2004) 745.
[181] D. Rodney, Nucl. Instrum. Methods Phys. Res. Sect. B 228 (2005) 100.
[182] Y. Mishin, D. Farkas, M.J. Mehl, D.A. Papaconstantopoulos, Phys. Rev. 59 (1999) 3393.
[183] Y. Mishin, M.J. Mehl, D.A. Papaconstantopoulos, A.F. Voter, J.D. Kress, Phys. Rev. 63 (2001) 224106.
[184] D.J. Bacon, Y.N. Osetsky, Z. Rong, Philos. Mag. 86 (2006) 3921.
[185] A. Nomoto, N. Soneda, A. Takahashi, S. Ishino, Mater. Trans. JIM 46 (2005) 463.

[186] D. Terentyev, L. Malerba, D.J. Bacon, Y.N. Osetsky, J. Phys. Condens. Matter 19 (2007) 456211.
[187] X.Y. Liu, S.B. Biner, Scripta Mater. 59 (2008) 51.
[188] S. Jumel, J.C. Van Duysen, J. Ruste, C. Domain, J. Nucl. Mater. 346 (2005) 79.
[189] D. Terentyev, D.J. Bacon, Y.N. Osetsky, Acta Mater. 56 (2008) 5034.
[190] J. Marian, B.D. Wirth, J.M. Perlado, Phys. Rev. Lett. 88 (2002) 255507.
[191] Y.N. Osetsky, A. Serra, V. Priego, J. Nucl. Mater. 276 (2000) 202.
[192] D. Terentyev, L. Malerba, P. Klaver, P. Olsson, J. Nucl. Mater. 382 (2008) 126.
[193] J. Marian, B.D. Wirth, R. Schaublin, G.R. Odette, J.M. Perlado, J. Nucl. Mater. 323 (2003) 181.
[194] Y.N. Osetsky, D.J. Bacon, B.N. Singh, B. Wirth, J. Nucl. Mater. 307 (2002) 852.
[195] Y.N. Osetsky, R.E. Stoller, Y. Matsukawa, J. Nucl. Mater. 329–333 (2004) 1228.
[196] Y.N. Osetsky, R.E. Stoller, D. Rodney, D.J. Bacon, Mater. Sci. Eng. A 400 (2005) 370.
[197] P. Szelestey, M. Patriarca, K. Kaski, Modell. Simul. Mater. Sci. Eng. 13 (2005) 541.
[198] Y.N. Osetsky, Y. Matsukawa, R.E. Stoller, S.J. Zinkle, Philos. Mag. Lett. 86 (2006) 511.
[199] J.S. Robach, I.M. Robertson, H.J. Lee, B.D. Wirth, Acta Mater. 54 (2006) 1679.
[200] H. Kimura, R. Maddin, in: R.M.J. Cotterill, M. Dotama, J.J. Jackson, M. Meshii (Eds.), Lattice Defects in Quenched Metals, Academic Press, New York, 1965, p. 319.
[201] Y.N. Osetsky (unpublished).
[202] J.S. Robach, I.M. Robertson, B.D. Wirth, A. Arsenlis, Philos. Mag. 83 (2003) 955.
[203] Y. Matsukawa, S.J. Zinkle, J. Nucl. Mater. 329–333 (2004) 919.
[204] Y. Matsukawa, Y.N. Osetsky, R.E. Stoller, S.J. Zinkle, Mater. Sci. Eng. A 400–401 (2005) 366.
[205] Y. Matsukawa, Y.N. Osetsky, R.E. Stoller, S.J. Zinkle, J. Nucl. Mater. 351 (2006) 285.
[206] Y. Matsukawa, Y.N. Osetsky, R.E. Stoller, S.J. Zinkle, Philos. Mag. 88 (2008) 581.
[207] V. Bulatov, F.F. Abraham, L. Kubin, B. Devincre, S. Yip, Nature 391 (1998) 669.
[208] R. Madec, B. Devincre, L. Kubin, T. Hoc, D. Rodney, Science 301 (2003) 1879.
[209] V.V. Bulatov, L.L. Hsiung, M. Tang, A. Arsenlis, M.C. Bartelt, W. Cai, J.N. Florando, M. Hiratani, M. Rhee, G. Hommes, T.G. Pierce, T.D. De La Rubia, Nature 440 (2006) 1174.